

COHERENT OPTICAL MANIPULATION OF ELECTRON SPINS IN  
SEMICONDUCTOR NANOSTRUCTURES

by

SHANNON O'LEARY

A DISSERTATION

Presented to the Department of Physics  
and the Graduate School of the University of Oregon  
in partial fulfillment of the requirements  
for the degree of  
Doctor of Philosophy

September 2008

“Coherent Optical Manipulation of Electron Spins in Semiconductor Nanostructures,” a dissertation prepared by Shannon O’Leary in partial fulfillment of the requirements for the Doctor of Philosophy degree in the Department of Physics. This dissertation has been approved and accepted by:

---

Dr. Miriam Deutsch, Chair of the Examining Committee

---

Date

Committee in Charge:      Dr. Miriam Deutsch, Chair  
   Dr. Hailin Wang, Adviser  
   Dr. David Cohen  
   Dr. Paul Csonka  
   Dr. Jeffrey Cina

Accepted by:

---

Dean of the Graduate School

An Abstract of the Dissertation of

Shannon O'Leary                      for the degree of                      Doctor of Philosophy  
in the Department of Physics                      to be taken                      September 2008

Title: COHERENT OPTICAL MANIPULATION OF ELECTRON SPINS  
IN SEMICONDUCTOR NANOSTRUCTURES

Approved: \_\_\_\_\_  
Dr. Hailin Wang, Adviser

Electron spin coherence can arise through a coherent superposition of two spin states in the conduction band of a semiconductor and can persist over remarkably long time and length scales. The robust nature of electron spin coherence makes it an excellent model system for exploring coherent quantum phenomena in semiconductors. This dissertation presents both spectral- and time-domain nonlinear optical studies of electron spin coherence through  $\Lambda$ -type three-level systems in two- and zero-dimensional semiconductor systems.

The spectral domain study focuses on the experimental realization of electromagnetically induced transparency (EIT), a phenomenon that exploits destructive interference induced by the spin coherence. Coherent Zeeman Resonance (CZR), a precursor to EIT, is demonstrated in two 2D systems, a GaAs mixed-type quantum well (MTQW) and a modulation doped CdTe quantum well (QW). For these studies,  $\Lambda$ -type three-level systems are formed via dipole coupling of a trion to two electron spin states. The CZR response can be described qualitatively by

effective density matrix equations. In addition, effects of manybody Coulomb interactions on CZR are investigated by varying the electron density in the MTQW via optical carrier injection.

Time-domain studies based on transient differential transmission (DT) are carried out to explore the excitation, manipulation, and detection of electron spin coherence and to better understand how manybody interactions affect coherent nonlinear optical processes in semiconductors. While electron spin coherence can be formed and detected via resonant excitation of excitons or trions, a surprising observation is that injecting excitons into the 2D electron gas in a modulation doped CdTe QW can significantly alter the oscillatory nonlinear response of the electron spin coherence, while the response remains qualitatively unchanged when trions are injected. These behaviors are attributed to an interplay between manybody effects and carrier heating generated by trion formation from excitons.

Finally, donor-bound electrons in GaAs are used as a model of localized electron spins. Spin decoherence of order 10 ns, limited by nuclear hyperfine interactions, is observed. Electron spin rotation induced by a nearly resonant laser pulse is also observed, opening the door for further work on mitigating electron spin decoherence time through optical spin echoes.

## CURRICULUM VITAE

NAME OF AUTHOR: Shannon T. O'Leary

PLACE OF BIRTH: Spokane, Washington

DATE OF BIRTH: August 12, 1977

## GRADUATE AND UNDERGRADUATE SCHOOLS ATTENDED:

University of Oregon

University of Puget Sound

## DEGREES AWARDED:

Doctor of Philosophy in Physics, 2008, University of Oregon

Master of Science in Physics, 2004, University of Oregon

Bachelor of Science in Physics and Mathematics, 1998, University of Puget  
Sound

## PROFESSIONAL EXPERIENCE:

Graduate Teaching Fellow, Department of Physics, University of Oregon,  
Eugene, 2002-2008

National Science Foundation GK-12 Program, University of Oregon,  
Eugene, 2003-2007

## GRANTS, AWARDS AND HONORS:

OSA/MRS Congressional Fellowship Finalist, 2008

Arthur H. Guenther Congressional Fellowship Finalist, 2008

Selected Participant and Travel Grant Recipient for the American Physical  
Society Workshop on Energy Research, APS March Meeting 2008

National Science Foundation GK-12 Fellow 2003-2007

Fundamental Optical Processes in Semiconductors, Student Travel Grant,  
2007

University of Oregon Women in Graduate Sciences Travel Scholarship, 2007

American Physical Society, Division of Laser Science Student Travel  
Grant, 2006

Graduated with Honors in Physics, University of Puget Sound, 1998

Coolidge Otis Chapman Honors Scholar, University of Puget Sound, 1998

Raymond S. and Olive Seward Memorial Scholarship, University of Puget  
Sound, 1997

Phi Beta Kappa, inducted in 1997

Sigma Pi Sigma, inducted in 1997

#### PUBLICATIONS:

**S. O’Leary** and H. Wang, “Manipulating Nonlinear Optical Response from Electron Spins in a 2-D Electron Gas via Exciton Injection,” in *Conference on Lasers and Electro-Optics/Quantum Electronics and Laser Science Conference and Photonic Applications Systems Technologies* (Optical Society of America, 2008) p. QFJ2.

**S. O’Leary** and H. Wang, “Manipulating nonlinear optical responses from spin-polarized electrons in a 2D electron gas via exciton injection,” *Phys. Rev. B* **77**, 165309 (2008).

**S. O’Leary** Y. Shen, and H. Wang, “Optical Control of Electron Spin Precession in Semiconductor Quantum Wells,” in *Conference on Lasers and Electro-Optics/Quantum Electronics and Laser Science Conference and Photonic Applications Systems Technologies* (Optical Society of America, 2007) p. QFB2.

**S. O’Leary**, H. Wang, and J. P. Prineas, “Coherent Zeeman resonance from electron spin coherence in a mixed-type quantum well,” *Opt. Lett.* **32**, 6 (2007).

**S. O’Leary**, H. Wang, and J. Prineas, “A Lambda-Type System for Electron Spins in a Mixed-Type GaAs/AlAs Quantum Well,” in *Conference on Lasers and Electro-Optics/Quantum Electronics and Laser Science Conference and Photonic Applications Systems Technologies* (Optical Society of America, 2006) p. QThB6.

M. L. Quillin, D. M. Anstrom, X. Shu, **S. O’Leary**, K. Kallio, D. M. Chudakov, and S. J. Remington, “Kindling Fluorescent Protein from *Anemonia sulcata*: Dark-State Structure at 1.38 Å Resolution,” *Biochemistry* **44** 5774 (2005).

## ACKNOWLEDGMENTS

I begin by thanking my adviser, Hailin Wang, for the generosity of his time and resources over the past four years. His enthusiasm for physics and unassailable optimism in the face of difficult experiments will continue to motivate me.

I give thanks to Alan Thorndike, who encouraged me to pursue physics and is my role model of an inspiring teacher.

I acknowledge the people who grew and provided the semiconductor nanostructures studied in this dissertation, including John Prineas and Ronald Cox.

I highly appreciate and admire the expertise Kris Johnson employed repairing a particularly stubborn leak in our superconducting magnet cryostat, which was used in the studies of the donor-bound electrons in Chapter V.

I thank all my colleagues in the Wang Lab who have shared not only their knowledge of physics and techniques in the lab, but also many laughs; I especially thank my officemates Young-Shin and Yan. I thank Carey for his patience discussing rotating spins with me and for sharing the calculation in Chapter V. Also, thanks to Mats for providing the PL spectrum in Chapter V. I also appreciate Tim, Nima, Yumin, Susanta, and Sasha for being my labmates and friends throughout the years.

The Physics and OCO Administration provided me with much support, both technical and personal, over the years, especially Bonnie, Patty S., Jani, Brandy, Jeff, and Janine.

I thank my homework team, without whom my first two years of graduate school would not have been as enjoyable or successful: Kristin—the rule-enforcer, Laura—the rule-interpreter, and Billy—the rule-breaker.

Other invaluable friends who made my time in Eugene memorable, and who understood the value and challenges of pursuing a Ph.D. are Keisuke, Libby, Ann, Chuck, H., Brian, Paul, Iva, Ruth, Regina, and Christine.

I thank my parents, Mike and Louise, for their unending love and encouragement.

And lastly I thank Adam, who has been my constant source of support throughout graduate school, and the person whose opinion I value the most.

## TABLE OF CONTENTS

Chapter	Page
I	INTRODUCTION . . . . . 1
1.1	Electromagnetically Induced Transparency . . . . . 1
1.2	Electron Spin Coherence . . . . . 3
1.3	Electron Spin Manipulation . . . . . 6
1.4	Manybody Interactions . . . . . 7
1.5	Overview of the Dissertation . . . . . 8
II	BACKGROUND THEORY OF SEMICONDUCTOR OPTICS . . . . . 11
2.1	Semiconductor Properties . . . . . 12
2.2	Bound Quasiparticles . . . . . 16
2.3	Confinement in Quantum Wells . . . . . 20
2.4	Effects of an Externally Applied Magnetic Field . . . . . 24
2.5	Chapter Summary . . . . . 28
III	COHERENT ZEEMAN RESONANCE FROM ELECTRON SPINS . . . . . 29
3.1	The GaAs Mixed-Type Quantum Well (MTQW) . . . . . 32
3.2	Trion Characterization in a GaAs MTQW . . . . . 34
3.3	Continuous Wave Pump-Probe Experimental Setup . . . . . 36
3.4	Continuous Wave Results for a GaAs MTQW . . . . . 38
3.5	The Modulation-Doped CdTe Quantum Well . . . . . 47
3.6	Continuous Wave Results for Modulation-Doped CdTe QW . . . . . 49
3.7	Chapter Summary . . . . . 49
IV	TRANSIENT INITIALIZATION, DETECTION AND MANIPULATION OF ELECTRON SPINS . . . . . 52
4.1	Time-Domain Differential Transmission Experimental Setup . . . . . 54
4.2	Spin Initialization and Detection . . . . . 57
4.3	Three-Pulse DT Studies . . . . . 61

Chapter	Page
4.4 Chapter Summary . . . . .	73
V TRANSIENT ROTATIONS OF LOCALIZED ELECTRON SPINS . . .	74
5.1 Introduction . . . . .	74
5.2 Motivation for Donor-Bound Electrons . . . . .	75
5.3 Characterization of Donor-Bound Electron System . . . . .	77
5.4 Transient DT of Donor-Bound Electrons . . . . .	80
5.5 Chapter Summary . . . . .	89
VI CONCLUSIONS, FUTURE WORK, AND OUTLOOK . . . . .	90
6.1 Dissertation Summary . . . . .	90
6.2 Future Work and Outlook . . . . .	93
APPENDIX: DENSITY MATRIX CALCULATION FOR THE SPECTRAL DOMAIN . . . . .	96
A DENSITY MATRIX CALCULATION FOR THE SPECTRAL DOMAIN	96
1.1 Introduction to the Density Matrix Approach . . . . .	96
1.2 The Density Matrix Equations of Motion . . . . .	98
1.3 The Order by Order Calculation . . . . .	100
1.4 The Nonlinear Signal . . . . .	108
BIBLIOGRAPHY . . . . .	111

## LIST OF FIGURES

Figure	Page
1.1 General Effects of EIT on the Optical Response of a Material . . . . .	3
1.2 Generic V-type and $\Lambda$ -type Three-Level Systems . . . . .	4
2.1 Generic Direct Gap Semiconductor Diagram . . . . .	13
2.2 Band Structure of a Direct Gap Semiconducture near $\mathbf{k} = 0$ . . . . .	15
2.3 Single Particle and Quasiparticle Energy Diagrams for Excitons . . . . .	20
2.4 Physical Structure of a Typical QW with Energy Diagram . . . . .	21
2.5 QW Energy Level Diagrams with and without Magnetic Field . . . . .	25
2.6 Equivalent Pictures of Spin Coherence and Spin Polarization . . . . .	26
2.7 Spin Precession due to External Magnetic Field . . . . .	27
3.1 Physical Structure of the GaAs MTQW . . . . .	32
3.2 Schematic of the GaAs MTQW Band Structure . . . . .	33
3.3 GaAs MTQW PL with Red and Green Pumping . . . . .	35
3.4 GaAs MTQW PL Temperature Dependence . . . . .	36
3.5 Spectral Domain Pump-Probe Experimental Setup . . . . .	37
3.6 CZR from Electron Spin Coherence in a GaAs MTQW . . . . .	39
3.7 Polarization Dependence of CZR in a GaAs MTQW . . . . .	40
3.8 Calculated Nonlinear Optical Response for a GaAs MTQW . . . . .	43
3.9 Injection Effect on CZR and Absorption in GaAs MTQW . . . . .	45
3.10 Comparison of Injection Experiment and Calculated Responses . . . . .	46
3.11 Physical Structure and Absorption of a Modulation-Doped CdTe QW . . . . .	48
3.12 CZR for a Modulation-Doped CdTe QW . . . . .	50
4.1 Experimental Setup for Transient Differential Transmission . . . . .	55
4.2 Two Equivalent Three-Level Energy Diagrams . . . . .	56
4.3 Cartoon of Spin-Polarization Initialization using Trion Excitation . . . . .	57
4.4 Doped CdTe Two-Pulse Measurement: Resonant Trion Excitation . . . . .	58
4.5 Band-filling Cartoon for the Exciton and Trion . . . . .	59
4.6 Doped CdTe Two-Pulse Measurement: Resonant Exciton Excitation . . . . .	61
4.7 Spectral Dependence of QB Amplitude . . . . .	62
4.8 Direct vs. Indirect QBs . . . . .	63

Figure	Page
4.9 3-Pulse DT: Degenerate on Trion and Exciton . . . . .	66
4.10 3-Pulse DT: Degenerate Wavelengths Summary . . . . .	67
4.11 3-Pulse DT: TXX Configuration . . . . .	68
4.12 3-Pulse DT: Configurations TTX and TXT . . . . .	69
4.13 Control Intensity Dependency of $ \alpha $ and $ \beta $ . . . . .	70
5.1 Photoluminescence Emission Spectrum of Bulk GaAs . . . . .	78
5.2 Absorption Spectrum of Bulk GaAs . . . . .	79
5.3 Absorption Spectra: Free Standing vs. Sapphire-Affixed Bulk GaAs . . . .	80
5.4 The $D^o - D^oX$ $\Lambda$ -type System . . . . .	82
5.5 Long-lived QBs from Donor-Bound Electrons . . . . .	83
5.6 Nonlinear Signal Detected over a Range of Wavelengths . . . . .	84
5.7 Pump Intensity Dependency of QB Amplitudes . . . . .	85
5.8 Fitted QB Amplitude and Phase vs $\sqrt{I_{pump}}$ . . . . .	86
5.9 Theoretical Pump Area Dependency of QB Amplitudes . . . . .	88
1.1 $\Lambda$ -Type Energy Level Scheme . . . . .	97
1.2 Term Contributions to the DT signal . . . . .	110

## LIST OF TABLES

Table	Page
2.1 Parameter Values for GaAs and CdTe . . . . .	18
4.1 Two-Color, Three-Pulse Experimental Configurations . . . . .	65

## CHAPTER I

### INTRODUCTION

This dissertation contributes to the field of experimental semiconductor optics. Using both continuous wave single-mode lasers and ultrafast pulsed lasers, coherences between electron spin states are initialized by dipole-coupling to a third state. The nonlinear optical responses from these coherences provide important information on coherent optical processes as well as manybody interactions inherent in semiconductors.

#### 1.1 Electromagnetically Induced Transparency

This research is instigated by a desire to understand and harness coherence and correlation effects in semiconductors in order to manipulate their optical properties and develop novel devices based on coherent effects. Advances in our knowledge can improve existing technologies or provide alternative semiconductor device applications. New devices based on semiconductors would have the advantage of being integrable into pre-existing solid-state technology.

Semiconductor optics experiments often begin with reproducing phenomena induced and observed in atomic and molecular systems. Familiar coherent effects

from atomic physics have been observed in semiconductor materials, including Rabi oscillations [1], quantum beats [2], and adiabatic population transfer [3].

An example of such a coherent effect which has been studied extensively for atomic systems, but is just starting to gain traction in the semiconductor optics community is electromagnetically induced transparency (EIT) [4]. EIT is a quantum coherent effect that causes an otherwise opaque material to become transparent, see Fig. 1.1. This dramatic light-matter interaction is the result of destructive interference between quantum transitions within the material [5]. EIT and similar coherent phenomena pave the way for a host of interesting and potentially useful quantum coherent effects. Recent studies include demonstrating the reduction in the group velocity of light to a few meters per second [6], and stopping and storing pulses of light in a material [7], with the ability to read them out later [8]. These breakthroughs point to the possibility of using EIT as a mechanism for quantum memory [9].

In order to use EIT for an application such as quantum memory, the feasibility of practical implementation motivates the choice of semiconductors over atomic systems. The two main challenges of realizing EIT in semiconductors are that coherences are typically short-lived in semiconductors ( $\sim$ ps or fs) and manybody interactions can conspire to destroy the coherent signal. However, noteworthy progress in the Wang lab has been made inducing EIT in the transient-domain in semiconductor quantum wells [10, 11]. Recently EIT in the transient domain has been shown in self-assembled InGaAs/GaAs quantum dots [12].

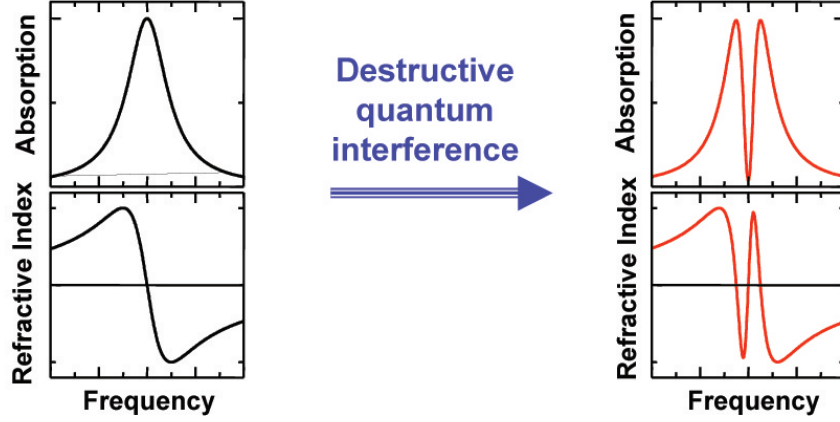


Figure 1.1: *General Effects of EIT on the Optical Response of a Material.* The curves on the left indicate typical absorption and dispersion curves of a material. EIT leads to nonlinear enhancement of the susceptibility of the material, demonstrated by altered absorption and dispersion curves shown on the right. The induced transparency is seen as a dip in the absorption. Correspondingly, the slope of the dispersion curve becomes steep and passes through zero.

## 1.2 Electron Spin Coherence

Coherences are established by optically exciting a coherent superposition of two states, with a well-defined phase relationship between relevant probability amplitudes. Referring to the three-level systems depicted in Fig. 1.2, an interaction of the system with a coupling light field creates a superposition of the three states written as follows:

$$|\Psi_{system}\rangle = C_a e^{i\phi_a} |a\rangle + C_b e^{i\phi_b} |b\rangle + C_c e^{i\phi_c} |c\rangle,$$

where  $C_a e^{i\phi_a}$ ,  $C_b e^{i\phi_b}$ , and  $C_c e^{i\phi_c}$  are the probability amplitudes of states  $|a\rangle$ ,  $|b\rangle$ , and  $|c\rangle$  respectively. The dipole coupling establishes this superposition, creating fixed relationships between the phases of the probabilities amplitudes. For example, the coherence between states  $|a\rangle$  and  $|b\rangle$  can be described by  $C_a^* C_b e^{i(\phi_b - \phi_a)}$ . This coherence, which is nonradiative because a direct transition between these two

states is dipole-forbidden, exists as long as the phase relationship  $\phi_a - \phi_b = \text{constant}$  is preserved. Each defined phase relationship in the system describes a quantum coherence, and is limited by its preservation time, referred to as the decoherence time. These times are reduced when the quantum system interacts with the environment, such as scattering events between carriers or with lattice vibrations. In semiconductor nanostructures at low temperatures, the main dephasing mechanism for electron spin coherence involves interactions with the surrounding nuclear spin bath hosted by the crystal lattice [13, 14].

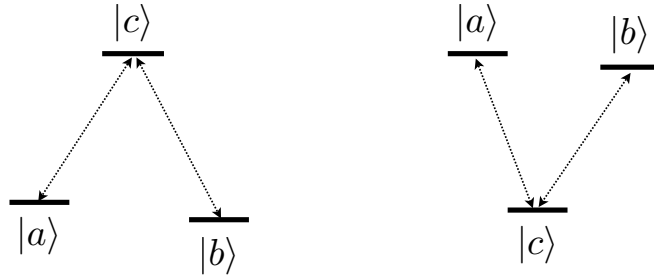


Figure 1.2: *Generic V-type and  $\Lambda$ -type Three-Level Systems.* *Left:* A generic  $\Lambda$ -type three-level system. *Right:* A generic V-type three-level system. In both cases, the arrows indicate dipole-allowed transitions. A nonradiative coherence exists between states  $|a\rangle$  and  $|b\rangle$ .

### 1.2.1 Decoherence Mechanisms of Electron Spin Coherence

Most coherences in semiconductors are fragile. Hole-spin and exciton-spin coherences, for example, dephase on the order of picoseconds [15]. Electron spin coherence is exceptionally long-lived in comparison, remaining intact on the order of the electron-hole recombination time, which is  $\sim$ ns. Electron spin coherence has been reported to persist up to 100 ns in n-doped systems [16]. The robustness of the electron spin coherence results from the fact that the electron spin, in contrast to the hole spin, is largely decoupled from the orbital degrees of freedom. Spin-orbit

coupling of charge carriers leads to mixing of the spin states, and any perturbation of the orbital would lead to a phase variation of the spin state [17]. However, the electron spins in our systems are relatively immune to this source of decoherence because spin-orbit coupling is weak for conduction band electrons in most zinc-blende semiconductors [18]; the zinc-blende semiconductors GaAs and CdTe being the subjects of interest in this thesis. Nevertheless, coupling to the nuclear spins of the crystal lattice through hyperfine interactions puts a limit on the electron spin decoherence time, at about 10 ns [19]. The nuclear spins create an effective magnetic field, and allow flip-flop processes that dephase the spin coherence. A clever method to defray these dephasing effects from nuclear spins has recently been experimentally shown. The nuclear spin states are brought to a specific and stable quantum state by mode-locking with the laser repetition rate [20]. In this way, the spin coherence can actually be stored in the nuclear spin bath and be recovered up to 0.3 s later [21].

### *1.2.2 $\Lambda$ -type Three-Level Systems for Electron Spin Coherence*

Because electron spin coherence is a robust, nonradiative quantum coherence, it provides an excellent platform for pursuing the manipulation of quantum coherences in semiconductors and for developing coherent quantum devices [22, 23]. The majority of electron spin coherence studies have focused on the transient response, using processes such as time-resolved photoluminescence, time-resolved Faraday rotation [15], and transient differential transmission [24, 25]. Earlier spectral domain studies exploit a V-type three-level system, for which the electron spin states serve as the upper states and the spin decoherence time is limited by the radiative lifetime of the relevant optical transition [26]. A  $\Lambda$ -type three-level system,

in which ground-state electron spin states are dipole-coupled to a common upper state, however, provides a more promising scheme for coherent applications such as EIT, quantum repeaters [5], and controlled generation of single photons [27, 28].

The attractiveness of the  $\Lambda$ -type three-level system lies in the fact that the electron spins are energetic ground states. The electron spin decoherence time is therefore not limited by the radiative lifetimes of excited electron spin states, and long decoherence times are essential for any practical application. Further, only negligible absorption is necessary to induce the coherence in a  $\Lambda$ -type three-level system, and so processes such as EIT are not hindered by strong pump absorption. To induce electron spin coherence in the V-type system, a photoexcited electron-hole pair must be produced by absorbing a photon. This absorption limits the efficacy of EIT.

A  $\Lambda$ -type three-level system for electron spins was recently realized in semiconductors using donor-bound excitons in bulk GaAs [29]. This work showed coherent population trapping utilizing electron spin coherence. As an alternative to semiconductor material, but still in the solid-state,  $\Lambda$ -type three-level systems using nitrogen-vacancy centers in diamond are also being pursued [30]. This dissertation presents experimental work investigating coherence from electron spins using  $\Lambda$ -type three-level systems in three semiconductor nanostructures.

### 1.3 Electron Spin Manipulation

Once electron spin coherence in a  $\Lambda$ -type three-level system has been induced and detected, the next step is to influence the nonlinear signal, and ultimately control the spins themselves through ultrafast coherent optical manipulation. In attempting to manipulate the spins, the manybody effects inherent in

semiconductors often manifest themselves as obstacles to attaining the desired coherent effect. Extensive experimental studies have been carried out with nonlinear optical techniques such as transient differential transmission (DT) and time-resolved Faraday or Kerr rotation [24, 25]. These studies have emphasized spin dynamics, including the generation, rotation, and decay of spin coherences [31–33]. In addition, electron spin rotation has also been used to manipulate the nonlinear optical response from electron spin coherence [34].

Recent work in a single quantum dot claims an important step forward in electron spin manipulation. An a.c Stark shift was used to create an effective magnetic field along the light propagation direction. This effect was used to manipulate a single electron spin in a time interval as short as 30 ps, which is almost three orders of magnitude faster than any previous single spin manipulation achieved in previous work [35].

#### 1.4 Manybody Interactions

Semiconductors also provide an ideal environment for studying the influence of manybody interactions and Coulomb correlations, which is a difficult unsolved problem in condensed-matter physics. It is well-known that the optical responses of dilute atomic gases are well-described by independent transitions between atomic levels, and that the nonlinear responses can be understood by the Pauli exclusion principle, or “state-filling,” of a collection of independent non-interacting two-level systems [36]. However, semiconductors typically containing  $10^{22} - 10^{23}$  particles/cm<sup>3</sup> [37], are by no means a dilute collection of independent particles. These particles interact through Coulombic forces and bind together to form quasiparticles such as excitons and trions. Optical excitation of these quasiparticles

dominates the linear properties of semiconductors at the bandgap. Further, interactions between these quasiparticles profoundly influence the nonlinear optical response of semiconductors [38].

Coulombic forces not accounted for in the theoretical treatment of the formation of quasiparticles lead to interactions between the quasiparticles, inducing nonlinearities and destroying phase coherences [37]. These interactions involve many degrees of freedom [39].

Advancement in growth technology supports the production of high-quality samples, and our understanding of the band structures and basic optical responses of semiconductors are well-established by both theory and experiment [40]. Semiconductors can be fabricated with atomic precision, and therefore confinement effects, which enhance correlations and optical nonlinearities, can be customized to facilitate controlled studies of manybody interactions. Analyzing these interactions provides insight into the Coulomb correlations and the quantum nature of condensed-matter systems, and is hence of fundamental interest.

## 1.5 Overview of the Dissertation

The thesis focuses on electron spin coherence from three different semiconductor nanostructures. Each nanostructure was chosen not only because it can enable a  $\Lambda$ -type three-level system for electron spin states, but also because each has a special feature we can exploit in our experimental studies. The next chapter provides background details on semiconductor optics, including a description of collective excitations including free excitons, bound excitons, and trions, which are needed in each of our three nanostructures to provide the upper level in the  $\Lambda$ -type system.

We begin our experimental study of electron spin coherence in the spectral domain (Chapter III), performing EIT-like differential transmission (DT) experiments on a GaAs mixed-type quantum well (MTQW). This nanostructure has the unique feature that the density of electrons in the quantum well conduction band can be optically controlled. We use this feature to study trion formation as well as to monitor the impact of manybody interactions on our nonlinear resonance from electron spin coherence. We observe that while the electron spin coherence induced via trions remains robust with increasing electron density, the nonlinear signal is suppressed because of the fragility of the relevant dipole coherences [41].

Encouraged by the resilient quality of electron spin coherence enabled through trions revealed by the MTQW studies, we initiate electron spin coherence studies in a modulation-doped CdTe quantum well sample, known for its well-resolved, strong trion absorption resonance. High quality nonlinear resonance peaks due to electron spin coherence via trions observed in the spectral domain DT (Chapter III), motivates further studies of the sample in the time domain (Chapter IV). The transient experiments seek to investigate the spin coherence initialization process with two-pulse measurements, as well as study manybody effects introduced by a third pulse. We learn that the spin coherence is initialized in the two-dimensional electron gas (2DEG) of the CdTe QW through trion formation, which can be brought about either by resonant trion excitation or resonant exciton excitation. Despite the fact that the electron spin coherence can be indiscriminately initialized either by trion or exciton pumping, the three-pulse DT studies reveals an interesting disparity. The nonlinear signal, detected at the exciton resonance can be qualitatively altered by injecting excitons at the appropriate time. However, injecting trions into the system does not have any appreciable effect [42].

While fascinating, these manybody effects foil attempts at ultrafast manipulation of the electron spin coherence. In order to study electron spin coherence in a system that does not experience manybody effects to the same degree, we consider electrons bound to neutral donors in bulk GaAs (Chapter V). The donor-bound electrons are localized, and hence their motion is quantized in all three directions. In the limit of a dilute donor concentration interactions between donors are negligible. After characterizing donor-bound excitons with photoluminescence and absorption studies, we show spin coherence from the donor-bound electron coupled to the donor-bound exciton state to be long-lived,  $\sim 10$  ns. This coherence time is limited by interactions with the surrounding nuclear spins of the GaAs crystal lattice. We also show pump intensity dependency studies of the nonlinear signal from the donor-bound electron spin coherence which suggest partial spin rotation induced by the pump, opening the door for future work on mitigating the electron spin decoherence time through optical spin echoes, discussed further in Chapter VI.

## CHAPTER II

### BACKGROUND THEORY OF SEMICONDUCTOR OPTICS

This dissertation presents experimental nonlinear optical studies in three semiconductor nanostructures, each chosen because of its ability to support a  $\Lambda$ -type three-level system for inducing electron spin coherence. These nanostructures include a GaAs/AlAs mixed-type quantum well, a modulation-doped CdTe quantum well, and a high-purity bulk GaAs sample. This chapter provides a basic review of semiconductor optics, with a focus on using resonant optical excitations to induce electron spin coherence. First an introduction to the semiconductor materials of interest is given, with a presentation of their bulk characteristics and electronic band structures. Bound quasiparticles including free excitons, bound excitons, and trions are discussed. We show how the semiconductor energy level structure can be engineered using quantum confinement. When semiconductors are grown in a low-dimensional structure such as a quantum well, quasiparticles become more tightly bound. Finally, we describe the standard experimental technique of applying an in-plane magnetic field to enable electron spin coherence. A brief presentation of magnetic field effects is given, including modification of the selection rules, electron Zeeman splitting, and electron spin precession.

## 2.1 Semiconductor Properties

Both GaAs and CdTe have a zinc-blende crystal structure, which is based on a face-centered-cubic (f.c.c.) lattice. In both GaAs and CdTe, each constituent atom has four valence electrons, given that eight electrons are covalently shared in each molecule comprising the crystal. The valence electrons of a four-valent atom come from s- and p- orbitals, and the nature of these orbitals plays into the character of the semiconductor band structures, especially at the band edge, where the electron wave vector is null or  $\mathbf{k} = 0$ .

The electronic states, or band structure, of a crystalline solid such as GaAs or CdTe can be calculated according to the band theory of solids, which can be found in standard texts [40]. The idea is that atoms become so tightly packed when bonded together as a crystal that their outer orbitals overlap. This overlap causes the discrete energy levels of individual atoms to merge, forming bands of energy. The electrons occupy these bands up to the Fermi energy. When the structure has an even number of electrons per atom, as is the case for our structures of interest, the highest occupied band is completely full of electrons and is called the valence band (VB). The lowest unoccupied band is called the conduction band (CB), and the Fermi energy is located somewhere between the VB and CB. Excitation of an electron, and hence absorption of a photon, requires a minimal amount of energy corresponding to the energy difference between the VB and CB, which is referred to as the band gap,  $E_g$ . When a photon is absorbed by the semiconductor, an electron from the VB is promoted to the CB, leaving behind a hole in the VB. Interband photon absorption is equivalent to this electron-hole pair production, see Fig. 2.1.

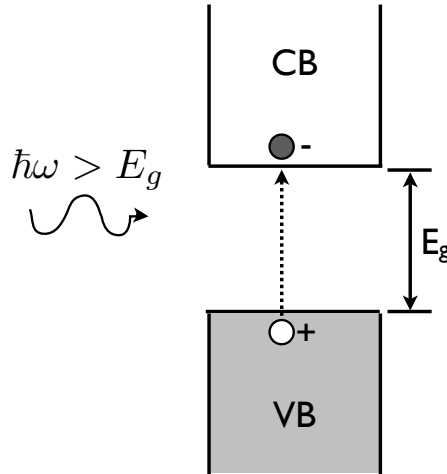


Figure 2.1: *Generic Direct Gap Semiconductor Diagram.* The conduction band (CB) and valence band (VB) are separated by  $E_g$ , the band gap. In direct gap semiconductors, photons with energies greater than  $E_g$  can promote electrons from the VB into the CB, leaving a hole behind in the VB.

Both GaAs and CdTe are direct gap semiconductors, making them favorably suited for optical studies. An appropriately polarized photon with energy greater than the band gap energy,  $\hbar\omega \gg E_g$ , can be absorbed. This is in contrast to indirect gap semiconductors which require a phonon to assist the transition process in order to conserve momentum. Because our structures of interest are direct gap semiconductors, we restrict our attention on the band structure near  $\mathbf{k} = 0$ , which is known as the  $\Gamma$ -point of the Brillouin zone.

The motion of free electrons and holes is determined by the E-k dispersion of the crystal. For free electrons, the dispersion is given by the parabolic relationship:

$$E = \frac{p^2}{2m_o} = \frac{\hbar^2 k^2}{2m_o}, \quad (2.1)$$

where  $m_o$  is the electron's rest mass and  $p$  is the electron's momentum, given by  $p = \hbar k$ . The E-k relationship in Eqn. 2.1 must be modified for electrons in a crystal,

since the electrons are not actually free. The modification, arising from the perturbation of the crystal lattice potential, is quantified by an effective mass,  $m^*$ , defined by the curvature of the parabolic dispersion curve as follows:

$$m^* = \hbar^2 \left( \frac{d^2 E}{dk^2} \right)^{-1} \quad (2.2)$$

For GaAs and CdTe near  $\mathbf{k} = 0$ , the VB is p-like and therefore has three bands, each band being 2-fold degenerate considering the electron spin states. Recall that total angular momentum,  $J$ , is defined as  $J = L + S$ , where  $L$  is the orbital angular momentum and  $S$  is the electron spin. The p-like nature of the VB restricts our interest to the  $\ell = 1$  subspace, where six states are characterized by their total angular momentum eigenstates  $|J, J_z\rangle = |3/2, \pm 3/2\rangle, |3/2, \pm 1/2\rangle$ , and  $|1/2, \pm 1/2\rangle$ . Please see Fig. 2.2 for a band structure diagram near  $\mathbf{k} = 0$ . Two hole bands  $|3/2, \pm 3/2\rangle, |3/2, \pm 1/2\rangle$  are degenerate at  $\mathbf{k} = 0$ , but have distinct curvatures. These are known as the heavy (HH) and light hole (LH) bands, with the HH band having the smaller curvature, and hence the greater effective mass by Eqn. 2.2. Spin-orbit coupling leads to a large energy suppression of the  $|3/2, \pm 1/2\rangle$  band such that this third valence band has a lower energy than the HH and LH bands, denoted  $\Delta$ , and is known as the split-off (SO) hole band. Likewise, the CB is s-like and thereby has  $\ell = 0$ , and one 2-fold degenerate band with electrons having total angular momentum  $J = 1/2$ .

All four of these bands have parabolic dispersion curves near  $\mathbf{k} = 0$ . Positive curvature of a CB indicates an electron band, and negative curvature of a VB indicates a hole band. An electron in the CB behaves like a negatively-charged free particle of mass  $m_e^*$ , whereas a hole in the VB behaves like a positively-charged free particle of mass  $m_h^*$ . The dispersion for the four bands near  $\mathbf{k} = 0$  are written as

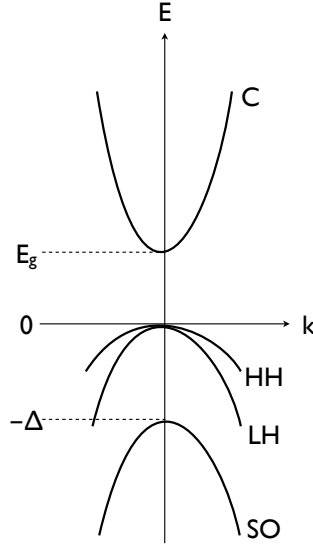


Figure 2.2: *Band Structure of a Direct Gap Semiconductor near  $\mathbf{k} = 0$ .* At  $\mathbf{k}=0$ ,  $E = 0$  is the top of the VB where the heavy hole (HH) and light hole (LH) bands are degenerate.  $E = E_g$  corresponds to the bottom of the CB, which hosts electrons. The split-off (SO) hole band is shown shifted down by  $E = -\Delta$ .

follows:

$$E_C(k) = E_g + \frac{\hbar^2 k^2}{2m_e^*} \quad (2.3)$$

$$E_{HH}(k) = -\frac{\hbar^2 k^2}{2m_{HH}^*} \quad (2.4)$$

$$E_{LH}(k) = -\frac{\hbar^2 k^2}{2m_{LH}^*} \quad (2.5)$$

$$E_{SO}(k) = -\Delta - \frac{\hbar^2 k^2}{2m_{SO}^*} \quad (2.6)$$

Furthermore, the p-like nature of the VBs and s-like nature of the CB makes transitions from all three bands to the CB dipole-allowed by electric dipole selection rules. However, the SO hole band is rarely involved in direct-band studies because its energy is so low.

## 2.2 Bound Quasiparticles

The above treatment has neglected Coulomb interactions between charged particles, as well as all other manybody interactions. But in reality, the optical response of semiconductors are usually dominated by the particle correlations resulting from these interactions. The primary optical response of semiconductors is the photo-creation of electron-hole pairs. Coulomb attraction can cause this pair to form a bound state, called an exciton, as is discussed below.

### 2.2.1 *Free Excitons*

In semiconductors, electron-hole pairs are created at the same point in space, by photon absorption. The electron and hole, having opposite charge, can bind together via Coulomb attraction and form an exciton, which is a stable, neutral quasiparticle. The electron and hole orbit each other much like positronium, and the bound state can be modeled using effective mass theory. In semiconductors, the radius of orbit of the exciton is usually much larger than the unit cell of the crystalline solid. These excitons are referred to as free excitons, otherwise known as Wannier-Mott excitons. If the exciton is not associated with any particular lattice site, it is free to move. Wannier excitons contrast with Frenkel excitons, which are tightly-bound, having small radii comparable to the Bohr radius. Frenkel excitons are found in insulator and molecular crystals.

The binding of a Wannier exciton is well described by the Bohr model, because the electron-hole separation is large enough one can approximate the structure of the atoms in between the electron and hole with a uniform dielectric material. The free electron is modeled as a hydrogenic system using a high dielectric constant for the crystalline medium,  $\epsilon_r$ , as well as the reduced electron-hole mass

mass,  $\mu$ , given by:

$$\frac{1}{\mu} = \frac{1}{m_e^*} + \frac{1}{m_h^*} \quad (2.7)$$

Standard results for the hydrogen atom can be applied, and the exciton bound states are quantized by the principle quantum number  $n$ . The exciton energy level in terms of the Rydberg constant of the hydrogen atom,  $R_H = 13.6\text{eV}$ , as a function of  $n$  is given by:

$$E_X^{3D}(n) = -\frac{\mu}{m_o} \frac{1}{\epsilon_r} \frac{R_H}{n^2} = \frac{R_X}{n^2} \quad (2.8)$$

where  $R_X = (\mu/m_o\epsilon_r^2)R_H$  is defined as the exciton Rydberg constant. Following through with the hydrogenic analogy, the radius of the electron-hole orbit is given by:

$$r_X(n) = \frac{m_o}{\mu} \epsilon_r n^2 a_H = n^2 a_X \quad (2.9)$$

where  $a_H = 0.053$  nm is the Bohr radius and  $a_X = (m_o\epsilon_r/\mu)a_H$  is defined as the exciton Bohr radius.

As listed in Table 2.1, GaAs and CdTe have comparable band gaps and lattice constants. Small effective masses and the high effective dielectric constants of the crystals result in exciton Bohr radii that are two orders of magnitude larger than the Bohr radius. Likewise, the exciton binding energies are three and two orders of magnitude smaller than the Rydberg energies. To illustrate the size of these excitons, we do a simple estimation of the number of unit cells contained in each  $n = 1$  exciton. The volume of a sphere,  $V_X = 4/3\pi a_X^3$ , approximates the exciton volume, and a cube gives the volume of each unit cell,  $V_{cell} = a^3$ . We find that approximately  $5 \times 10^4$  unit cells are contained within a GaAs exciton, and  $5 \times 10^3$  unit cells are in a CdTe exciton. With increasing excitation, the exciton wavefunctions will increasingly overlap with one another leading to exciton-exciton

correlations and bound-states. These exciton-exciton interactions have a significant impact on the optical response of the semiconductor [43].

Table 2.1: *Parameter Values for GaAs and CdTe.*

	GaAs	CdTe	Ref.
Band Gap, $E_g$ (eV)	1.6	1.5	[44]
Lattice constant, $a$ (nm)	0.57	0.65	[44]
Exciton Bohr radius, $a_X$ (nm)	13	6.7	[44]
Exciton Rydberg Energy, $E_X$ (meV)	4.2	12	[44]
Dielectric constant, $\epsilon_r/\epsilon_o$	12.8	9.4	[45]
Electron effective mass, $m_e/m_o$	0.066	0.1	[46]
Heavy hole effective mass, $m_{hh}/m_o$	0.47	0.4	[46]
Number of unit cells/exciton	$5.2 \times 10^4$	$4.6 \times 10^3$	estimation

A hole can be created in either the LH or HH band to bind with an electron in the CB and form of an exciton referred to as either a LH-exciton or a HH-exciton. The energy of each exciton is equal to the energy required to promote the electron to the CB,  $E_g$ , minus the electron-hole binding energy,  $E_X$ :

$$E_n = E_g - \frac{R_X}{n^2} \quad (2.10)$$

In the direct gap semiconductors, a photon of energy  $E_n$  can form an exciton. The formation of the bound state is energetically favorable, so the likelihood of exciton formation is high. The optical absorption spectrum of a typical semiconductor has peaks at energies beneath the band gap corresponding to LH and HH excitons of  $n = 1$ ,  $n = 2$ , etc.

### 2.2.2 Impurity-Bound Excitons

When the semiconductor material is highly pure, containing only a relatively small number of neutral impurities, excitons can be attracted to these impurities through van der Waals interactions. If the impurity can contribute an electron to the semiconductor CB, it is called a donor. Whereas if the impurity can contribute a hole to the VB (by capturing an electron), it is called an acceptor. Attraction to a neutral impurity lowers the exciton energy, and thereby makes the impurities efficient traps for the excitons.

Theoretical treatment of bound-excitons follows similar logic as that outlined above for free exciton. Instead of using an analogy to the hydrogen atom, we use results from the hydrogen molecule  $H_2$ . In the case of donors, the four-body complex called a neutral donor-bound exciton ( $D^0X$ ), is composed of two electrons in spin-singlet states, a hole, and a positive ion. The  $D^0X$  was first predicted by Lampert in 1958 [47] and was first experimentally verified in silicon by Haynes in 1960 [48].

While the  $D^0X$  can still be considered a Wannier exciton because its radius greatly exceeds the size of a unit cell, it is not a free exciton. The complex is localized to the impurity site. Because the impurities are sparsely scattered through the crystal, and the excitons are tethered to them, bound excitons are less likely to suffer from interactions, and the inhomogeneous absorption linewidth can be quite small. For example, in high purity n-type GaAs, the absorption linewidth for the  $D^0X$  transition can be as small as  $10 \mu\text{eV}$ .

Before moving on to discuss the confinement effects of lowering the dimensionality of the semiconductor, we stress here that although an atomic binding analogy matches well with the binding conditions of excitons, the nature of optical

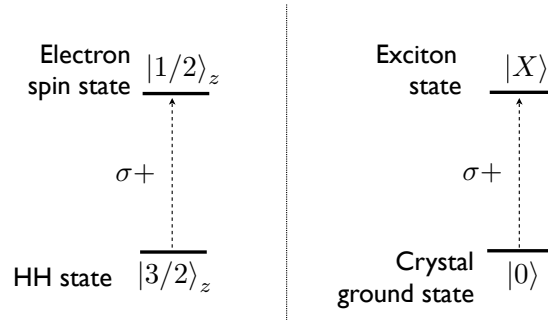


Figure 2.3: *Single Particle and Quasiparticle Energy Diagrams for Excitons.* Photo-creation of an exciton *Left:* in the single particle picture, and *Right:* in the quasiparticle picture.

excitations in each system is fundamentally different. In the case of an atom, absorption of a photon causes an electron to transition to a higher energy orbital. But in the resonant excitation of excitons in semiconductors, an excitation causes the system to go from its ground state to the exciton state,  $|0\rangle \rightarrow |X\rangle$ .

### 2.3 Confinement in Quantum Wells

Semiconductor materials are grown in structures that confine the electrons and holes to exist in two-, one- or zero-dimensions. An example of each kind of structure is a quantum well (QW), quantum wire, and quantum dot, respectively. This section will focus on the confinement effects of quantum wells.

Grown by molecular beam epitaxy (MBE) or chemical vapor deposition, a single QW is formed when a thin semiconductor of thickness  $d$ , called the well layer, is sandwiched in between two high bandgap semiconductors of thickness  $b$ , called barrier layers (see Fig. 2.4.) If the well layer is thin enough and the bandgap energies have a large ratio, the electrons in the well layer experience confinement within the plane of the QW. Quantum confinement becomes important when the confinement energy,  $E_c$ , is larger than the thermal kinetic energy. That is, when

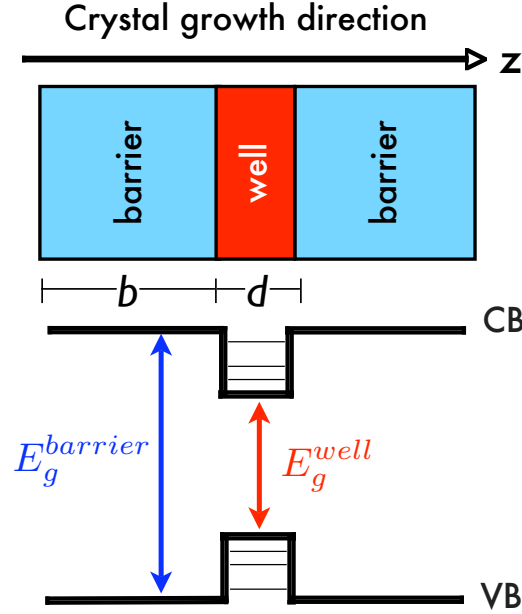


Figure 2.4: *Physical Structure of a Typical QW with Energy Diagram.* A physical schematic of a quantum well is shown above, with corresponding spatial variation in the conduction band (CB) and valence band (VB) below. A single quantum well, is formed when a thin semiconductor of thickness  $d$ , is sandwiched by two higher bandgap semiconductor layers of thickness  $b$ . The electrons and holes are effectively trapped within the well layer because the band gap relationship,  $E_g^{barrier} > E_g^{well}$ .

$E_c > \frac{1}{2}k_B T$ . The confinement energy is defined using the Heisenberg Uncertainty relationship,  $\Delta p_x \sim \hbar/\Delta x$ :

$$E_c = \frac{\Delta p_z^2}{2m} = \frac{\hbar^2}{2m(\Delta z)^2} \quad (2.11)$$

From Eqn. 2.11, we obtain a condition on the well thickness,  $b$ , for obtaining confinement within the well:

$$d \sim \sqrt{\frac{\hbar^2}{mk_B T}} \quad (2.12)$$

Both GaAs and CdTe have effective electron masses of  $m_e \sim 0.1m_o$ . We require  $d \sim 5$  nm for quantum size effects to be important at room temperature. Our

experiments are all performed at cryogenic temperatures, where this constraint can be relaxed to  $d \sim 25$  nm at  $T = 10$  K.

We can understand the major characteristics of quantum confinement by treating the wells as infinite potential barriers, and apply the results of the classic quantum mechanical problem of “particle in a box.” By solving Schrödinger’s equation and applying boundary conditions, the energy levels of the electrons and holes in the QW are given by the standard result:

$$E_n = \frac{\hbar^2}{2m^*} \left( \frac{n\pi}{d} \right)^2 = n^2 \Delta E \quad (2.13)$$

Eqn. 2.13 describes a ladder of energy levels increasing by  $n^2$  in units of  $\Delta E$ , the so-called confinement energy. The confinement energy increases the unconfined ground state by  $\Delta E$ . The energy of the levels is inversely proportional to the effective mass,  $m^*$ , and therefore the HH band and LH band do not have the same quantization energy. The degeneracy of the HH and LH bands in the bulk case is lifted and the HH, with its larger effective mass, becomes the lowest energy level in the VB. Eqn. 2.13 also shows that the energy of the levels is inversely proportional to the square of the well thickness,  $d^2$ . This fact allows for band engineering, and will become important when we discuss the mixed-type QW structure in the next chapter.

The main confinement effect on the formation of excitons is that the electron and hole are forced spatially closer to each other. The exciton bound state energies are:

$$E_n^{2D} = -\frac{R_X}{(n - 1/2)^2} \quad (2.14)$$

Comparing Eqns. 2.14 and 2.8, we can see that the binding energy of a

two-dimensional exciton is four times the binding energy of a three-dimensional exciton.

In reality, the barriers are of finite height, therefore the electrons and holes can tunnel out of the well with a probability depending on the bandgap ratio between barrier and well. There are also a finite number of energy levels contained within the well, not implied by Eqn. 2.13.

### 2.3.1 Trions

In confined semiconductor nanostructures such as QWs, the presence of a low density electron gas in the CB can lead to the formation of three-body complexes consisting of a hole and two electrons of opposite spin [49]. Analogous to a hydrogen ion,  $H^-$ , this complex can be thought of as a charged exciton, and is often referred to as a trion. The formation of trions was predicted in 1958 by Lampert [47], but its small binding energy prevents experimental observation in the bulk. Not until high quality quantum wells were developed, in which confinement enhances the binding energy by an order of magnitude compared to in the bulk, did physical evidence for the trion exist, observed in 1993 by K. Kheng et al. [50]. The binding of the exciton to the excess electron lowers the total energy of the exciton, and therefore trions resonances appear energetically below exciton resonances. We will observe this in Fig. 3.3.

Kheng et al. used the most straightforward method of obtaining the low electron density necessary for trion formation. They used a modulation-doped quantum well. This doping method implants n-type dopants, or donors, into the quantum well barrier. In this way, the dopants are spatially separated from the actual quantum well, so that scattering between photo-excited carriers and the

dopants is minimized. But the dopant electrons remain available for trion formation. The low density electron gas can also be obtained using a novel nanostructure called a mixed-type quantum well, which will be discussed in more detail in Chapter III.

## 2.4 Effects of an Externally Applied Magnetic Field

### 2.4.1 *Modification of the Optical Selection Rules*

To realize electron spin coherence in these semiconductor nanostructures, two electron spins states must have dipole-allowed transitions to a common state. In the work presented in this thesis, the two electron spin states belong to the low density electron gas in the CB, provided by n-doping (either through modulation doping, residual doping, or optically-injected doping). These electron spin states are in the ground state, because no corresponding holes in the VB cause the electrons to recombine and drop back to the VB.

The common state to which both electron spin states can couple is the energy level of a trion. However, in order to realize this  $\Lambda$ -type system for electron spins, we must use a standard semiconductor optics technique; an external magnetic field is used to alter the selection rules of the system [51]. With no magnetic field, the two electron spin states of an electron are written in the  $z$ -basis and have dipole-allowed transitions to trion states, using right-hand or left-hand circularly polarized light, written  $\sigma+$  and  $\sigma-$  in Fig. 2.5. However, in this configuration, the two electron spin states cannot couple to a common trion energy level. We therefore must apply an external magnetic field in the plane of the QW, perpendicular to the QW growth direction. This so-called Voigt configuration causes the electron spins to align with the magnetic field. Simultaneously, at relatively weak magnetic field strengths, spin-orbit coupling in the valence band along with quantum confinement

of the well geometry keeps the holes from aligning with the magnetic field, and  $J_z$  of the holes remains an approximately good quantum number [52]. As a result of magnetic field, the original  $z$ -basis electron spin states are mixed, and we express them in the  $x$ -basis. Optical dipole-coupling between the two electron spin states to a common trion state is enabled, and two  $\Lambda$ -type three-level systems are formed. We can choose to address only one of the  $\Lambda$ -type three-level systems by using appropriately polarized light.

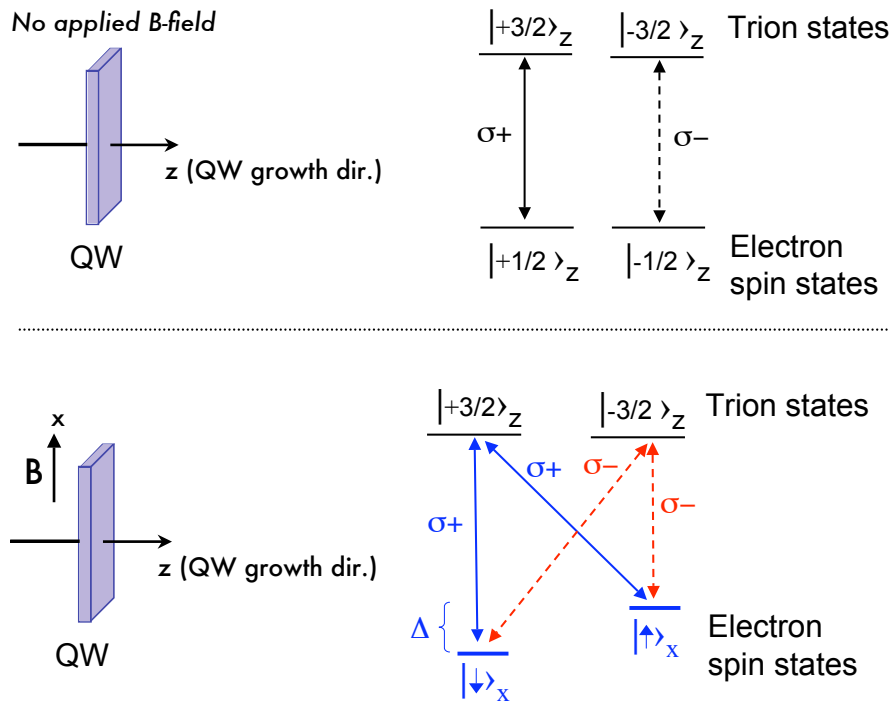


Figure 2.5: *QW Energy Level Diagrams with and without Magnetic Field.* *Top:* Cartoon of the MTQW without an externally applied magnetic field and the corresponding energy level structure of the electron spin states and trion spin states. Trions are labeled by the  $J_z$  of the constituent hole. *Bottom:* The diagram shows the effects of an in-plane magnetic field on the energy level structure. Two  $\Lambda$ -type three-level systems are formed by spin-up and spin-down electron states coupled to a common trion state.

In the semiconductor materials discussed in this thesis, the electron spin states experience Zeeman splitting given by:

$$\Delta E_Z = g_e \mu_B B \quad (2.15)$$

where  $g_e$  is the electron g-factor,  $\mu_B = \frac{e\hbar}{2m_0}$  is the Bohr magneton, and  $B$  is the externally applied magnetic field. The g-factor is a sample-dependent property, as it is sensitive of the degree of confinement [53]. We also note that the splitting scales linearly with the applied magnetic field.

#### 2.4.2 Electron Spin Precession

Electron spin coherences induced between to the two  $x$ -basis spin states in the  $\Lambda$ -type system discussed above can equivalently be thought of as a spin polarization,  $\mathbf{S}$ , in the  $z$ -direction as shown in the Fig. 2.6:

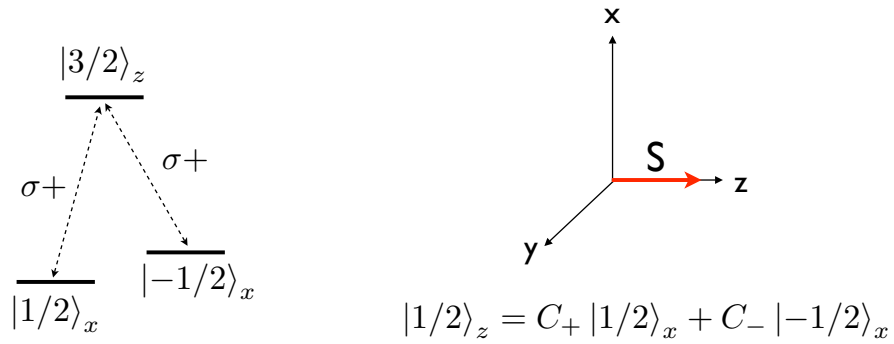


Figure 2.6: *Equivalent Pictures of Spin Coherence and Spin Polarization.* Electron spin coherence and electron spin polarization are equivalent pictures for the superposition of two electron spin states. The spin polarization concept is useful in understanding the transient response of spin coherence in the presence of an external magnetic field.

By an analogy to classical Larmor precession, we know that spin in an external magnetic field will experience a torque-like force given by the cross product of the magnetic moment and the magnetic field:

$$\frac{dS}{dt} = M \times B \quad (2.16)$$

where  $M$  is the magnetic moment, defined as  $M = -g_e\mu_B S$ . By taking the projection of  $M$  along the  $z$ -direction, we find the magnetic moment oscillates according to  $M_z = \cos(\omega_B t)$ . The frequency,  $\omega_B$ , is known as the Larmor frequency:

$$\omega_B = g_e\mu_B B \quad (2.17)$$

We can see that  $\omega_B$  is equivalent to the Zeeman splitting energy given in Eqn. 2.15. In the presence of a magnetic field, the polarization precesses, as depicted in Fig. 2.7. We observe this precession in the time-domain as quantum beats, to be discussed in Chapter IV.

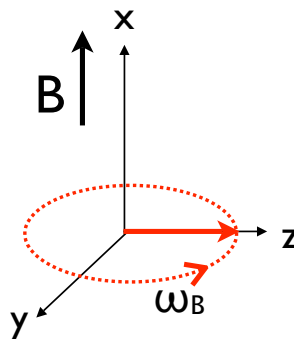


Figure 2.7: *Spin Precession due to External Magnetic Field.* In the presence of an external magnetic field, the electron spin polarization,  $S$ , precesses according to Larmor frequency  $\omega_B$ .

## 2.5 Chapter Summary

This chapter presents a brief introduction to the band-edge energy levels of semiconductors using the effective mass theory approach. Because GaAs and CdTe are both direct gap semiconductors, we have restricted our interest to bands close to  $\mathbf{k} = 0$ . These bands have a parabolic shape whose curvature defines an effective mass. The upper VB is characterized by two hole bands with distinct effective masses—the HH and LH bands. Exploiting analogies to hydrogenic atoms, we model strong Coulombic correlations between electrons and holes as bound quasiparticles with discrete energy levels. The discussions include free excitons, donor-bound excitons, and trions.

Confinement within a quantum well increases the exciton binding energy by a factor of four. By introducing a preferred direction according to the quantum well growth direction, the high symmetry of the bulk crystal is broken, and the degeneracy of the HH and LH bands is lifted. The quasiparticles dominate the linear optical response of semiconductors, and the relatively small binding energies of the quasiparticles correspond to large radii compared to the lattice constant of the semiconductor crystal. Therefore, the quasiparticles are big and loosely-bound, and the interactions between them has been shown to strongly influence the nonlinear optical signal.

These bound states provide the third level necessary for inducing electron spin coherence. In order to enable this coherence in the lab, an in-plane magnetic field must be applied to modify the inherent selection rules. The magnetic field also serves to Zeeman split the electron energy levels. Simultaneously, the electron spin coherence corresponds to an induced spin polarization projected on the  $z$ -axis of the Bloch sphere, and the magnetic field causes this spin polarization to precess.

## CHAPTER III

COHERENT ZEEMAN RESONANCE  
FROM ELECTRON SPIN COHERENCE

As introduced in Chapter I, Electromagnetically Induced Transparency (EIT) is a quantum coherent effect that causes an otherwise opaque material to become transparent. This dramatic light-matter interaction is the result of destructive interference between quantum transitions within the material. If two states, like the spin states of an electron, are dipole-forbidden to couple to each other, and are individually coupled to a third level, quantum interference of the probability amplitudes of the two allowed transition pathways can be established [5]. In EIT, two electromagnetic fields are used to couple two states to a common level. One of the fields is much weaker than the other and is typically called the probe. This three-level system can be V-type,  $\Lambda$ -type, or a cascade scheme.

The theory of EIT was first published by Olga Kocharovskaya and Yakov Khanin at the Institute of Applied Physics in Nizhni, Russia in 1988 [54] and independently by Steven Harris at Stanford in 1989 [55]. The first experimental demonstration of EIT quickly followed, performed in strontium vapor by the Harris group in 1991 [56]. The same year the Harris group also saw EIT in lead vapor [57]. Most EIT studies since then have been carried out in atomic or atomic-like systems, with a few noted exceptions [10, 11].

There are two main obstacles to realizing EIT in semiconductors. First, manybody Coulomb interactions between excitons strongly effect coherent nonlinear optical processes in excitonic systems. Second, quantum coherences in semiconductors are short-lived and fragile, with the exception of electron spin coherence. Despite these difficulties, the theory behind EIT can be applied to extended optical excitations such as excitons and trions in semiconductors. Further, real-world device applications based on EIT or EIT-related phenomena will be more feasible if supported in a solid-state material as opposed to, for example, a laser-cooled trap of atomic vapor.

This chapter presents experimental demonstrations of a quantum interference effect which is a precursor to EIT—Coherent Zeeman Resonance (CZR), or coherent Raman resonance between two Zeeman sublevels. CZR in DT responses arising from electron spin coherence can be considered a precursor to EIT because the resonance is created by an induced increase in the differential transmission, which correspondingly is an induced decrease in the absorption. Complete disappearance of the absorption would be equivalent to EIT. We present CZR results from two 2D semiconductor nanostructures, a mixed type GaAs/AlAs quantum well (MTQW) as well as a modulation-doped CdTe quantum well (QW). These semiconductor nanostructures were chosen because they both enable  $\Lambda$ -type systems, in which the two spin states of an excess electron in the conduction band are dipole-coupled with optical fields to a common trion state.

A unique feature of the MTQW is that tunable control of the excess electron density can be achieved via an optical carrier injection process described below. This optical tunability of the electron density makes the MTQW a model system for studying trion formation and especially for investigating the effects of manybody

interactions on the manifestation of electron spin coherence in nonlinear optical responses.

Our MTQW studies give us valuable initial insight into trions and how they can be utilized to enable electron spin coherence. While carrier injection leads to increased density of trions, the increased electron density in the conduction band causes manybody interactions such as electron-exciton scattering which broaden the relevant dipole coherences in the system. This fragility of the dipole coherences revealed by the carrier injection causes a suppression of the CZR signal.

Armed with the experimental knowledge gained from the MTQW studies, we sought a semiconductor nanostructure that allowed for similar robust trion formation, but did not carry with it the same manybody issues. Modulation-doped II-VI semiconductor materials are known to feature sharp optical transitions [58]. And a modulation-doped CdTe QW has the historical distinction of enabling the first experimental verification of the existence of trions, observed in 1993 by K. Kheng et al. [50]. Thus motivated, we were granted the opportunity to extend the spectral domain studies to the identical modulation-doped CdTe QW used by K. Kheng et al.

This chapter is organized as follows: After a brief discussion of the MTQW, its band structure and optical injection process, photoluminescent studies revealing trion formation in the MTWQ are shown. The spectral-domain experimental setup for the CZR study is given, and we present the nonlinear results for the MTQW, including an experimental realization of CZR, a spectral study of the CZR, injection studies, and an example of the polarization dependency of CZR. We then introduce the modulation-doped CdTe QW sample with an absorption spectrum. Finally, encouraging CZR results for a modulation-doped CdTe QW are given, and a chapter summary follows.

### 3.1 The GaAs Mixed-Type Quantum Well (MTQW)

The MTQW structure used in our studies was grown by John Prineas, from the University of Iowa, and consists of four periods of narrow (2.3 nm) and wide (16.0 nm) GaAs QWs separated by 11.2 nm AlAs barriers (see Fig. 3.1), with the GaAs substrate removed by chemical etching for transmission. The well growth direction is geometrically-defined by the structure and is labeled as  $z$ . The wide well (WW) is a typical QW as described in Section 2.3, in that electrons and holes both are confined within the same two-dimensional layer, the WW. Typical QWs such as our GaAs WW is referred to as a type-I QW. The narrow well (NW), on the other hand, is a type-II QW, or a spatially indirect bandgap semiconductor in which

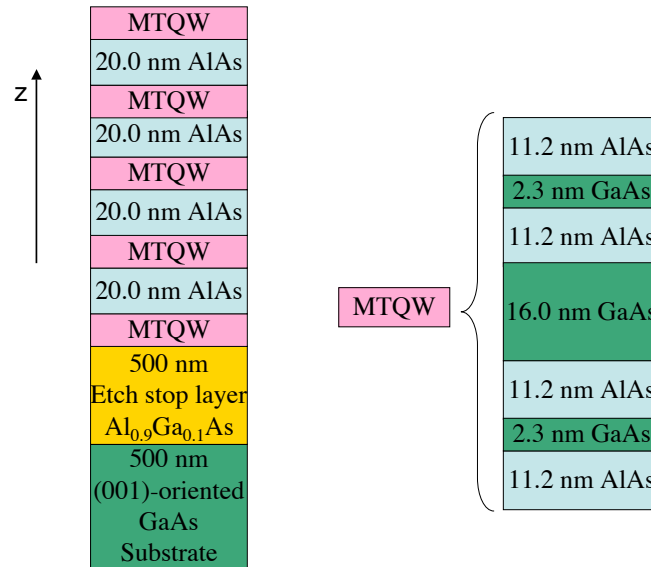


Figure 3.1: *Physical Structure of the GaAs MTQW. Right:* The GaAs MTQW structure consists of two narrow (2.3 nm) GaAs QWs and one wide (16.0 nm) GaAs QW separated by 11.2 nm AlAs barriers. *Left:* The full sample nanostructure consists of four periods of the MTQW separated by AlAs barriers of 20.0 nm thickness. The GaAs substrate is removed by chemical etching to enable transmission experiments. The AlGaAs stop etch layer prevents overetching.

electrons and holes are confined in a different layers. This spatial separation is due to the fact that the bottom of the NW conduction band is energetically higher than the conduction band minimum in the AlAs barrier. The band minimum in the AlAs layer happens to occur at the X point of the Brillouin zone, and is hence referred to as the X-valley. The presence of both type-I and type-II QWs is responsible for “mixed-type” part of the moniker MTQW.

As discussed in Chapter II, the QW thickness determines the electron and hole confinement, and therefore governs the band gap,  $E_g$ , according to Eqn. 2.13. The well thicknesses are chosen to enable a staircase of energy levels in the conduction band (see Fig 3.2). Electrons photoexcited above the band gap in the NW thermalize and transfer via the X-valley in the AlAs barrier to the conduction band of the wide well (WW). Meanwhile, the NW holes remain trapped in the NW valence band, preventing recombination with the electrons. Optical excitation of electron-hole pairs in the NW can thus control the excess electron density in the

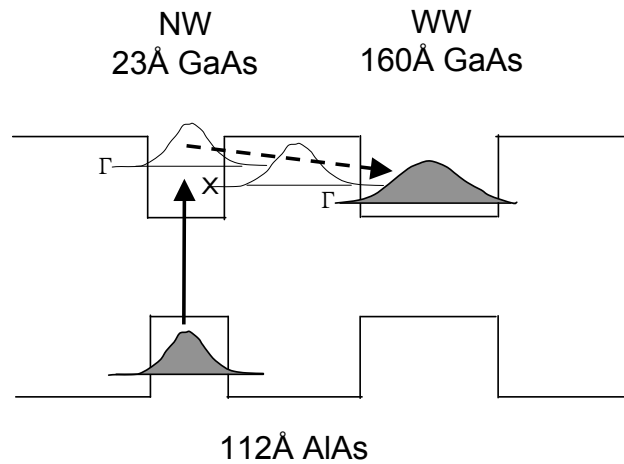


Figure 3.2: *Schematic of the GaAs MTQW Band Structure.* Electrons excited above the narrow well (NW) band gap thermalize and transfer via the X-valley in the AlAs barrier to the conduction band of the wide well (WW). The holes remain trapped in the NW valence band preventing recombination.

WW [59]. In our experiments, a laser beam at 2.33 eV serves this purpose, and is referred to as the *green injection* beam. A green injection intensity of  $0.5 \text{ mW/cm}^2$  is estimated to produce an excess electron density in the WW on the order of  $n_e = 10^9 \text{ e}^-/\text{cm}^2$ , with the assumption that the excess electron lifetime is limited by a hole-tunneling time on the order of  $10 \text{ } \mu\text{s}$  [59].

### 3.2 Trion Characterization in a GaAs MTQW

We have carried out extensive photoluminescence (PL) studies to elucidate the formation of trions in the WW. Fig. 3.3 shows PL spectra from the WW obtained under various excitation conditions at 10 K. When the sample is optically excited by a red Ti:sapphire laser at 1.54 eV, which is below the NW band gap, a predominantly excitonic emission from the WW is observed slightly above 1.531 eV (see dotted line in Fig 3.3). When the sample is excited additionally with the green injection beam, a strong emission 1.6 meV below the excitonic resonance emerges.

As shown in Fig. 3.3, with increasing green injection beam intensity, the lower energy PL resonance intensifies, accompanied by a decrease in the intensity of the exciton resonance. The PL spectrum obtained when the sample is excited by the green injection beam alone is also shown as a dashed curve in Fig. 3.3 for reference. Fig. 3.4 further shows that the lower energy PL resonance weakens with increasing temperature.

The above PL studies indicate that the lower energy PL resonance arises from radiative recombination of trions. In the MTQW, the trion binding energy, or the energy needed to bind a free electron to an exciton, is 1.6 meV. The competition between the two PL resonances with increasing green injection intensity also shows that excitons convert to trions as the excess electron density in the WW conduction

band is increased. The temperature dependent ratio between the trionic and excitonic PL emissions is in good agreement with earlier experimental studies [60]. Note that even though the MTQW sample is not intentionally doped, residual excess electrons are present in the QW with zero green injection intensity. A trion resonance can be observed in both PL and optical absorption without optical injection from the green injection beam.

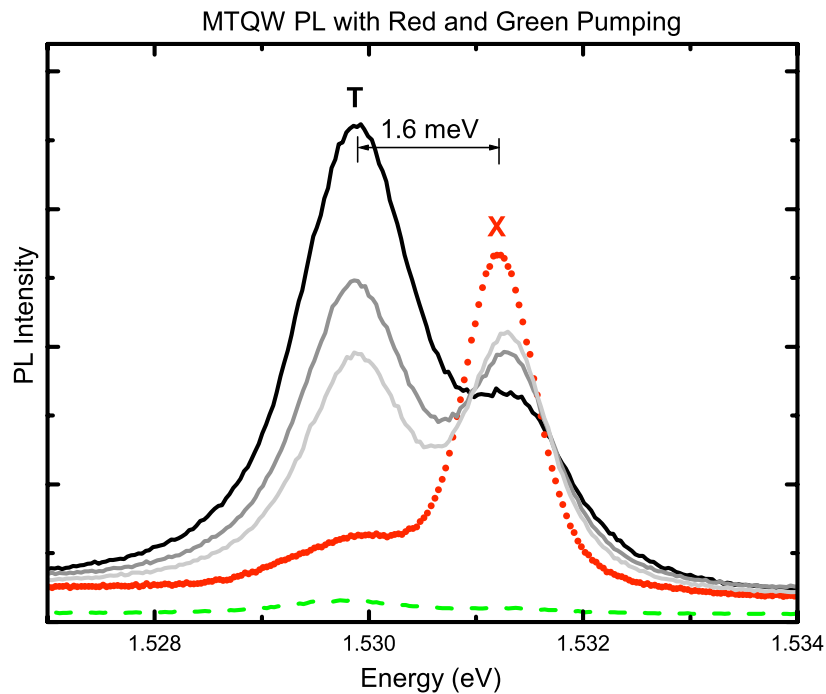


Figure 3.3: *GaAs MTQW PL with Red and Green Pumping.* PL spectra at  $T = 10$  K when GaAs MTQW is excited individually by a pump beam at 1.54 eV with  $I = 2$  W/cm<sup>2</sup> (dotted curve) and by a green injection beam at 2.33 eV with  $I = 2$  mW/cm<sup>2</sup> (dashed curve). Solid curves are PL spectra when the sample is simultaneously excited by both laser beams. From darkest to lightest curves the intensities of the green injection beam are  $I = 2, 1,$  and  $0.5$  mW/cm<sup>2</sup>. Trion emission (labeled T), and heavy hole exciton emission (labeled X) are separated by 1.6 meV, the binding energy of a electron to an exciton.

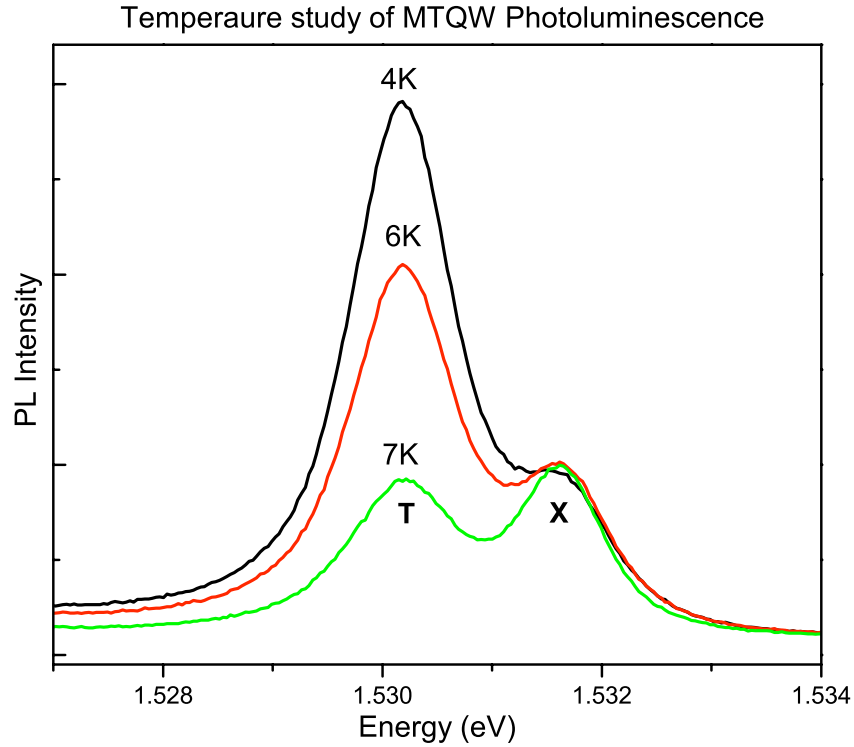


Figure 3.4: *GaAs MTQW PL Temperature Dependence.* Temperature dependence of PL spectra when a GaAs MTQW is excited simultaneously by a red pump beam at 1.54 eV with  $I = 2 \text{ W/cm}^2$  and a green injection beam at 2.33 eV with  $I = 2 \text{ mW/cm}^2$ . From top to bottom, PL taken at  $T = 4, 6,$  and  $7 \text{ K}$ . Trion formation is enabled at lower temperatures.

### 3.3 Continuous Wave Pump-Probe Experimental Setup

With this understanding of trion formation from PL studies, we proceed to discuss studies of CZR using a standard spectral domain pump-probe spectroscopy technique, see Fig 3.5. A vertically-polarized continuous wave tunable Ti:sapphire ring laser, operating in single mode, with  $I = 0.4 \text{ W/cm}^2$  serves as the pump, and a horizontally-polarized diode laser with  $I = 0.03 \text{ W/cm}^2$  acts as the probe. Earlier work confirms that cross-linearly polarized pump and probe beams will, like

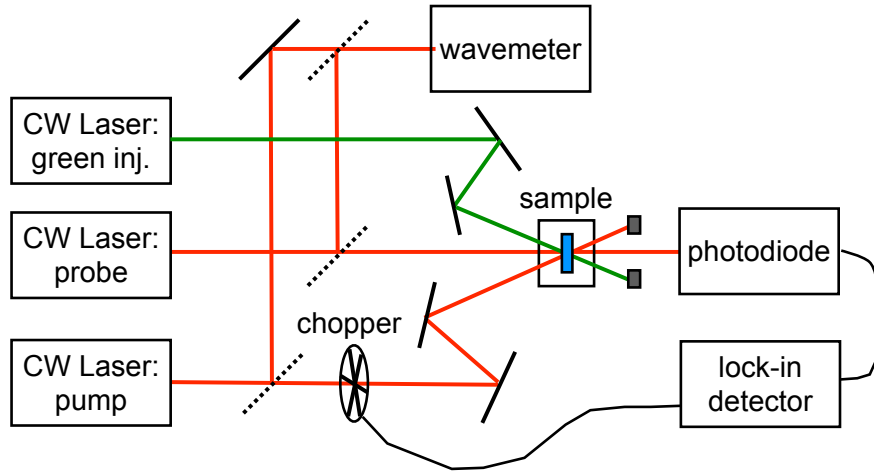


Figure 3.5: *Spectral Domain Pump-Probe Experimental Setup*. Experimental setup for spectral domain pump-probe spectroscopy. The wavelength of the pump is fixed and the probe wavelength is tuned through the pump's wavelength. The green injection laser is used with the MTQW to control the electron density in the conduction band WW.

co-circularly polarized pump and probe beams, excite the three-level system of interest [25].

The relative laser jitter between pump and probe is measured to be  $\sim 10$  MHz by monitoring the heterodyne beating of the lasers slightly detuned from each other on a spectrum analyzer. This relative jitter is much smaller than the decoherence rates of interest, but limits the spectral resolution of the experiment. The pump is mechanically modulated with a chopper and the DT signal is observed along the probe direction using phase-sensitive lock-in detection, which uses the chopper frequency as its reference. The DT signal is a measurement of changes in the probe transmission spectrum induced by the presence of the pump. The pump energy,  $E_{pump}$  remains fixed for each DT spectrum, while the probe energy,  $E_{probe}$ , is tuned across  $E_{pump}$  over a range of about 20 GHz. A wavemeter is used to set the pump energy and monitor the probe energy. The DT spectrum is presented below

as a function of the the detuning,  $\delta$ , which is defined as  $\delta = E_{pump} - E_{probe}$ , expressed as a difference frequency in GHz.

A green injection beam is used to control the excess electron density in the WW of the MTQW. The semiconductor sample is subjected to an external magnetic field produced by a small permanent magnet,  $B \approx 0.4$  T, in the plane of the QW, and the DT measurements were carried out at 10 K using liquid Helium and a cold finger cryostat.

### 3.4 Continuous Wave Results for a GaAs MTQW

The top graph in Fig. 3.6 shows the DT spectrum, where the pump beam is tuned to the trion absorption resonance (and with zero green injection intensity). Two resonances on either side of zero detuning are observed. The asymmetry in the DT signal is due to the nonuniformity of the magnetic field lines produced by the permanent magnet used in the experiment.

The energy separation between the two resonances is 2.7 GHz, which is twice the electron Zeeman splitting and is in good agreement with the expected electron g-factor,  $|g_e| = 0.27$ . We attribute these two resonances to CZRs arising from the electron spin coherence. In Fig. 3.7, we observe similar CZR peaks when the pump and probe have the same circular polarization,  $\sigma+\sigma+$ , as expected from the polarization selection rules for the underlying optical transitions. Fig. 3.7 also shows a dispersive resonance peak at  $\delta = 0$  for co-circularly and co-linearly polarized pump and probe. This central resonance is due to a two-level coherence effect, not involving the electron spin coherence. The CZR peaks are absent in the co-linearly polarized case, YY, because the two electron spin states cannot couple to a common level, and hence electron spin coherence is not induced.

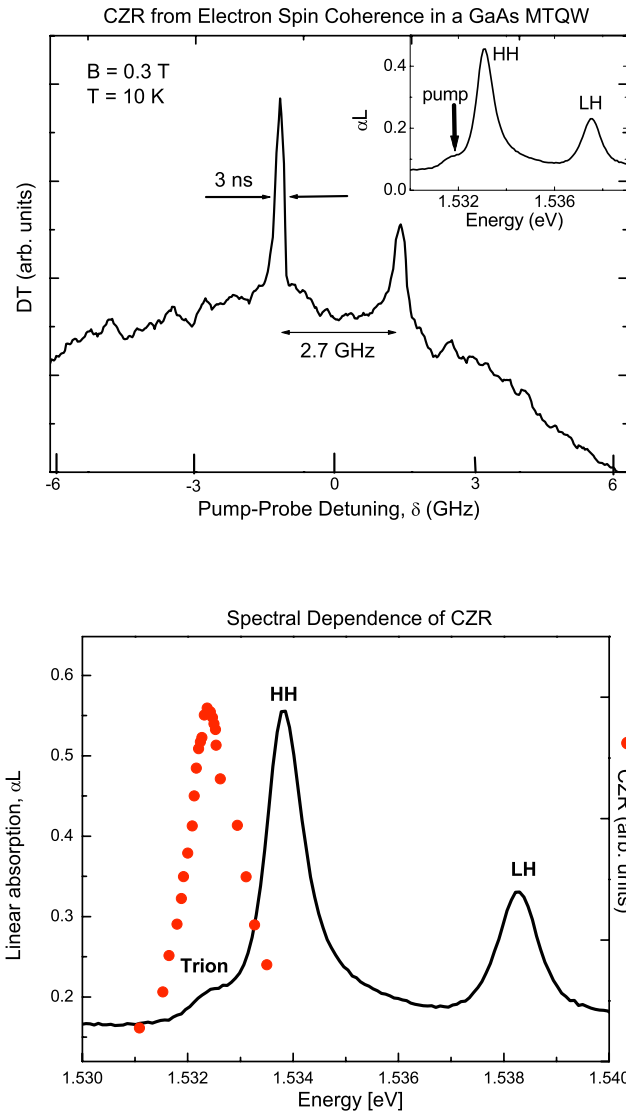


Figure 3.6: *CZR from Electron Spin Coherence in a GaAs MTQW*. *Top*: DT response from GaAs MTQW obtained at  $B = 0.3$  T and  $T = 10$  K, with the pump energy at trion absorption resonance. Sample absorption is shown in the inset, heavy hole and light hole absorption peaks labeled HH and LH respectively, with pump energy indicated by the arrow. *Bottom*: The black curve shows the linear absorption spectrum of the GaAs MTQW at  $T=10$  K with heavy hole (HH) exciton, light hole (LH) exciton, and trion resonances labeled. The dotted curve shows the CZR amplitude from a series of DT responses as a function of pump energy.

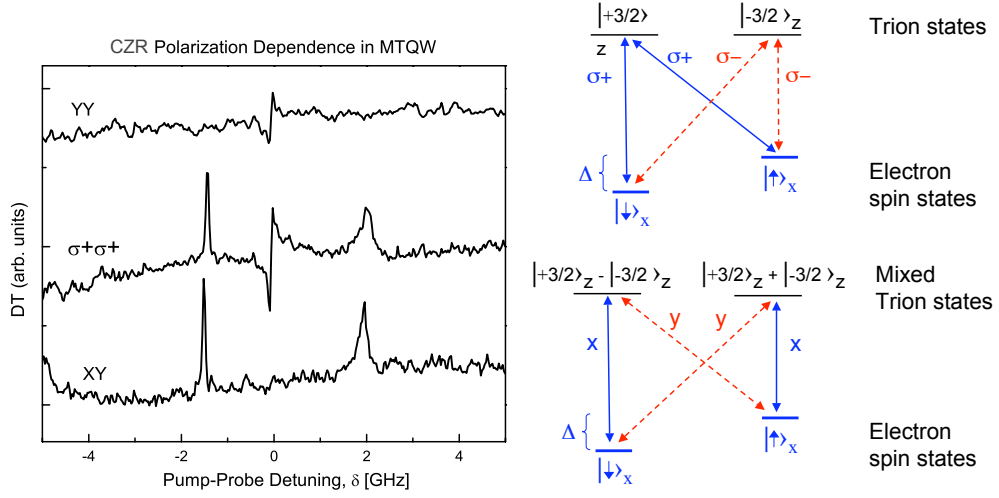


Figure 3.7: *Polarization Dependence of CZR in a GaAs MTQW.* *Left:* DT response from GaAs MTQW with similar conditions as in Fig 3.6 except for the pump and pump polarizations, which are indicated on the figure. *Right:* Relevant optical selection rules for circularly polarized ( $\sigma+$  and  $\sigma-$ ) and linearly polarized ( $x$  and  $y$ ) light.

We have carried out experimental studies of the DT response as a function of pump-probe detuning, with the pump fixed at various spectral positions along the trion resonance. The bottom graph in Fig. 3.6 shows the amplitude of the CZR from a series of DT responses as a function of the pump energy. The CZR amplitude follows the trion absorption resonance, confirming that trions play a central role in the CZRs. The linewidth of the CZRs corresponds to a spin decoherence rate as small as  $\gamma_s/2\pi = 75$  MHz (or a spin decoherence time of 2 ns), significantly smaller than the electron spin decoherence rate of 200 MHz obtained in earlier studies of a V-type three-level system [26]. These behaviors indicate that the CZR arises from a  $\Lambda$ -type three-level system with a trion state as the upper state, and experimentally confirms the advantage of using a  $\Lambda$ -type system over a V-type system for electron spin coherence studies, as discussed in Section 1.2.2.

### 3.4.1 Theoretical Analysis of CZR

The CZRs shown in Fig. 3.6 can be qualitatively understood by applying the density matrix approach to an analogous  $\Lambda$ -type three-level atomic-like system interacting with two external optical fields. The interaction Hamiltonian used employs the dipole approximation. The density matrix equations of motion are solved in the steady state using order-by-order perturbation. The electron spin coherence to the second order in the external fields leads to a third order DT response which we observe as CZR. The details of this calculation can be found in Appendix A, but the main result is shown below.

By considering the method of detection and nature of the polarization-included electric field, we see that the differential transmission signal (DT) is proportional to the imaginary part of the sum of the third order dipole coherence matrix elements,  $\rho_{bc}^{(3)}$ ,  $\rho_{cb}^{(3)}$ ,  $\rho_{ac}^{(3)}$ ,  $\rho_{ca}^{(3)}$ . That is,

$$DT \propto [\rho_{bc}^{(3)} + \rho_{ac}^{(3)}] + c.c. \quad (3.1)$$

Where  $\rho_{bc}^{(3)}$  is calculated to be:

$$\begin{aligned} \rho_{bc}^{(3)} = \frac{-i|\Omega_1|^2\Omega_2\mu_a^2\mu_b e^{-i\nu_2 t}}{i\Delta_{2b} + \gamma_b} & \left[ \frac{1}{(\omega_{ab} - \delta) + i\gamma_{ab}} \underbrace{\left( \frac{1}{i\gamma_a + \Delta_{1a}} + \frac{1}{i\gamma_b - \Delta_{2b}} \right)}_{spin.coh} \right. \\ & - \frac{1}{\gamma_{ab} - i\omega_{ab}} \underbrace{\left( \frac{1}{\gamma_a - i\Delta_{1a}} + \frac{1}{\gamma_b + i\Delta_{1b}} \right)}_{spin.DC} \\ & \left. + \dots \right] \end{aligned}$$

$$\begin{aligned}
& \dots + \frac{1}{\Gamma_a + i\delta} \underbrace{\left( \frac{1}{\gamma_a - i\Delta_{1a}} + \frac{1}{\gamma_a + \Delta_{2a}} \right)}_{pop.coh_1} \\
& \quad + \frac{1}{\Gamma_a} \underbrace{\left( \frac{1}{\gamma_a - i\Delta_{1a}} + \frac{1}{\gamma_a + i\Delta_{1a}} \right)}_{pop.DC_1} \\
& \quad + \frac{2}{\Gamma_b + i\delta} \underbrace{\left( \frac{1}{\gamma_b - i\Delta_{1b}} + \frac{1}{\gamma_b + \Delta_{2b}} \right)}_{pop.coh_2} \\
& \quad \left. + \frac{2}{\Gamma_b} \underbrace{\left( \frac{1}{\gamma_b - i\Delta_{1b}} + \frac{1}{\gamma_b + i\Delta_{1b}} \right)}_{pop.DC_2} \right] \tag{3.2}
\end{aligned}$$

In Eqn. 3.2, the index  $n = 1, 2$  refers to the pump or probe respectively, and the index  $i = a, b$  refers to dipole transition  $\mu_a$  or  $\mu_b$ .  $\Omega_{1,2}$  are the Rabi frequencies and  $\nu_{1,2}$  are the laser frequencies. The Zeeman splitting between the electron spin states is written  $\omega_{ab}$ , and further  $\omega_{bc}$  and  $\omega_{ac}$  are the energy level separations of the dipole-allowed transitions.  $\Gamma_{a,b,c}$  are the population decay rates, and  $\gamma_{ab,bc,ac}$  are the decoherence rates between relevant energy levels. We define  $\delta$ , the parameter scanned during the experiment, the detuning between the laser frequencies as  $\nu_2 - \nu_1 = \delta$ . Finally to simplify notation, we have made the following definitions for the detunings:

$$\begin{aligned}
\Delta_{1a} &= \omega_{ac} - \nu_1 & \Delta_{2a} &= \omega_{ac} - \nu_2 \\
\Delta_{1b} &= \omega_{bc} - \nu_1 & \Delta_{2b} &= \omega_{bc} - \nu_2
\end{aligned}$$

Each term in Eqn. 3.2 is labeled according to its origin—whether the term derives from spin coherence or dipole (population) coherence and also whether the

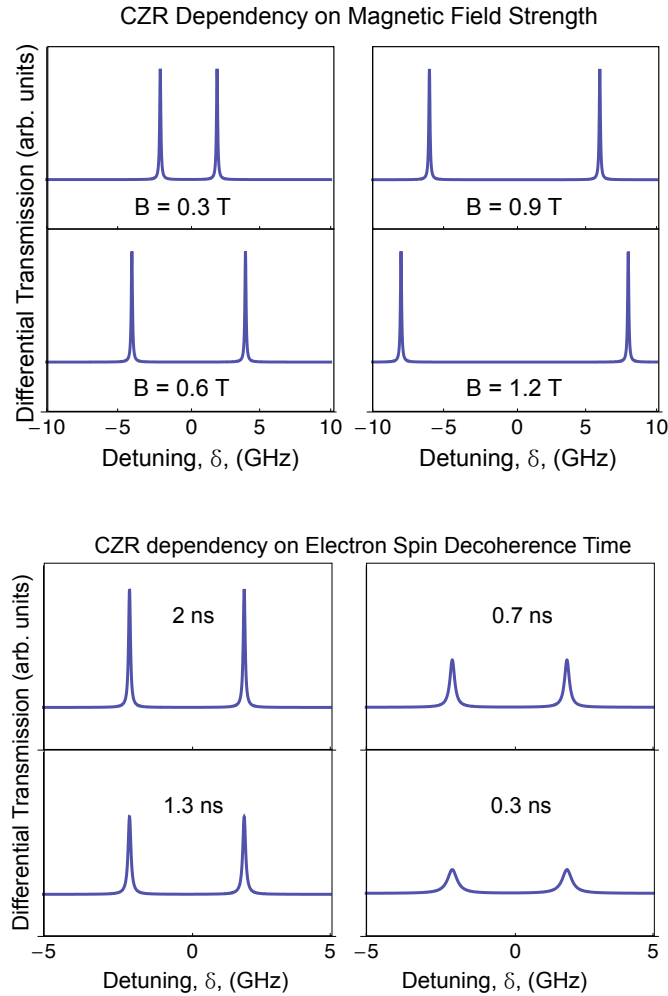


Figure 3.8: *Calculated Nonlinear Optical Response for a GaAs MTQW. Top: Magnetic field dependency. Bottom: Electron spin decoherence time dependency.*

two fields were acting coherently in the second order or incoherently (so-called “D.C.”-terms). Further, the dipole matrix element  $\rho_{ac}^{(3)}$  can be found simply by replacing a with b in the above expression. The calculated DT responses shown in Fig. 3.8 show how the CZR signal is affected by a magnetic field applied externally in the Voigt geometry. As the magnetic field strength increases, the electron spin states Zeeman split further and further apart, causing the CZR peaks to spread away from zero detuning. The calculation uses parameters taken from the

experiment, specifically a spin decoherence rate of  $\gamma_s/2\pi = 75$  MHz and an electron Zeeman splitting of  $\Delta = 1.35$  GHz. The calculated DT response is in qualitative agreement with the experimental observation.

### 3.4.2 Carrier Injection and Manybody Interactions

As mentioned in Chapter I, it is well known that nonlinear optical responses in semiconductors are strongly modified by the underlying manybody interactions [39]. In fact, the primary distinction between semiconductor optical phenomena and the optical responses of atomic systems is the strong effect in semiconductors of correlations induced between particles by an interacting field. In atomic systems and in the calculation described in Appendix A, the optical response is well characterized by independent transitions between atomic levels, and the nonlinear dynamics can be understood by band-filling [36]. However, in dense manybody systems, like semiconductors, the particles do not behave independently. Coulombic interactions between charged particles play an especially dominant role in semiconductors [43]. Coulomb interactions can be so strong that new quasiparticles such as excitons and trions form. Also, dynamic interactions between particles can destroy previously-initialized coherences.

To investigate how manybody interactions affect the CZR from the electron spin coherence, we monitor the DT response as a function of the excess electron density by varying the green injection intensity. Fig. 3.9 shows that as the intensity of the green injection beam is increased, the amplitude of the CZR becomes suppressed. Without understanding the decoherence effect that can result from manybody interactions, this result may be somewhat counter-intuitive by the following logic: As shown in Section 3.2, an increase of the green injection intensity

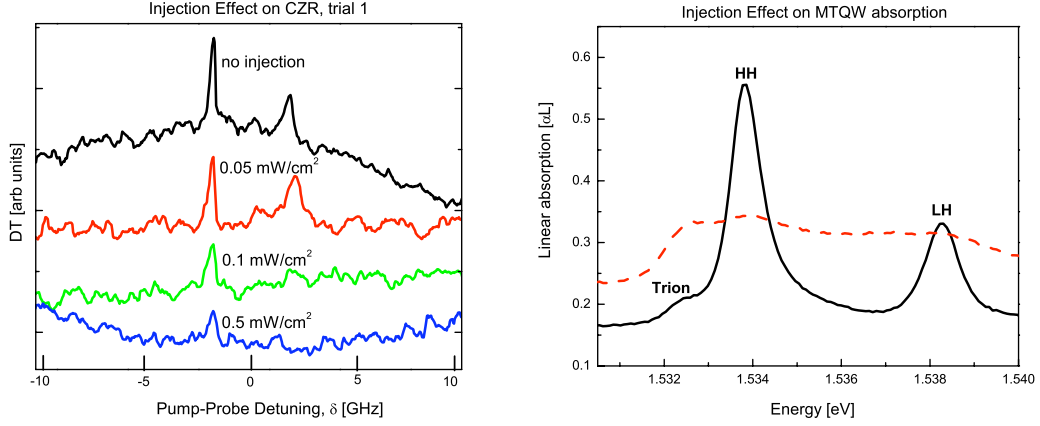


Figure 3.9: *Injection Effect on CZR and Absorption in GaAs MTQW.* *Left:* DT responses are shown with increasing green injection beam intensity, from top to bottom curves,  $I = 0, 0.05, 0.1,$  and  $0.5$  mW/cm<sup>2</sup>. *Right:* Solid curve shows absorption with no green injection. Dashed curve shows absorption with injection of  $I = 0.05$  mW/cm<sup>2</sup>

leads to a corresponding increase in the density of excess electrons and hence an effective increase in the number of  $\Lambda$ -type three-level systems in the WW. One might expect that with an increased density of  $\Lambda$ -type three-level systems, a stronger signal from the induced electron spin coherence would be observed. But, instead, we observe the opposite effect—the CZR signal decreases with increasing electron density.

To understand the suppression of the CZR, we compare the absorption spectra of the sample with and without optical injection from the green injection beam, see Fig. 3.9. Without optical injection, the linear absorption spectrum shows a small trion absorption resonance below the energy of the heavy hole exciton resonance. With green injection beam of  $I = 0.05$  mW/cm<sup>2</sup>, the amplitude of the trion absorption increases, as we would expect. But simultaneously, the heavy hole (HH) and light hole (LH) exciton resonances broaden dramatically. The broadening of the excitonic absorption resonances corresponds to a rapid decay of the excitonic

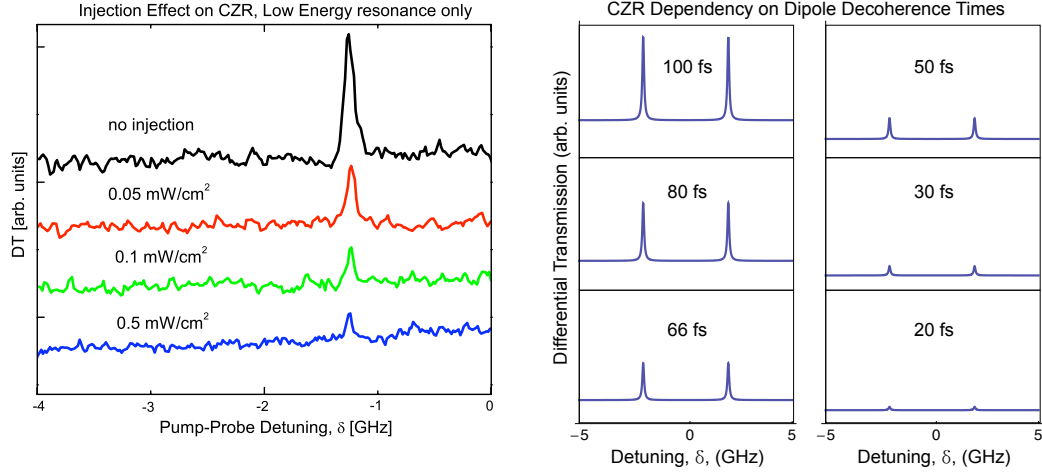


Figure 3.10: *Comparison of Injection Experiment and Calculated Responses.* *Left:* A second trial of experiment shown on the left in Fig 3.9. *Right:* Dependency of CZR signal on dipole decoherence time.

or dipole coherences. As this broadening is caused by injecting electrons into the conduction band of the WW, we attribute the effect to exciton-electron scattering. Earlier studies have also shown that exciton-electron scattering leads dephasing of dipole coherence [61]. Theoretically, the amplitude of the CZR is inversely proportional to the square of the dipole decoherence rate,  $\gamma$ , as can be seen in Eqn. 3.2 by setting  $\gamma_a = \gamma_b$ . With increasing green injection intensity, the large increase in the dipole decoherence rate thus overwhelms the modest increase in the number of trions in the WW, leading to a suppression, instead of an enhancement, of the CZR.

Although increasing the electron density in the WW conduction band causes the overall amplitude of the CZR peaks to decrease, we observe that the CZR linewidth is not appreciably affected, as can be readily observed in the left graph in Figs. 3.9 and 3.10. This observation confirms the robust nature of the electron spin coherence. The CZR peaks do not broaden, and thus we know that the electron spin coherence is immune to the manybody interactions induced by the green injection

beam. The right graph in Fig. 3.10 shows the calculated DT signal for decreasing dipole coherence times, leaving all other parameters fixed. The results show that with decreasing dipole coherence time, the CZR amplitudes decrease where we have assumed that the CZR linewidths, determined by the electron spin decoherence rate, remain unchanged. These results match well with our experiments.

### 3.5 The Modulation-Doped CdTe Quantum Well

Encouraged by the robust electron spin coherence enabled by trions in the above work on GaAs MTQWs, but seeking a semiconductor nanostructure that will be robust against manybody interactions that will diminish dipole coherences, we turn to a II-VI semiconductor quantum well—a modulation-doped CdTe QW. The sample was provided by R. T. Cox and K. Kheng of the Nanophysics and Semiconductors team at the Néel Institute and the CEA in Grenoble, France.

Like the GaAs MTQW, the modulation-doped CdTe QW also holds the promise of supporting  $\Lambda$ -type three-level systems for electrons spins via trions. In addition, the trion binding energy in CdTe is large compared to that in the GaAs MTQW (2.6 meV versus 1.6 meV), so we can expect that the coherences induced in CdTe will be less likely to ionize, and therefore more robust.

The sample is a high quality n-doped CdTe QW grown by molecular beam epitaxy on a transparent  $\text{Cd}_{0.88}\text{Zn}_{0.12}\text{Te}$  substrate [50]. The nanostructure consists of 10 periods of 10 nm CdTe wells and 45 nm  $\text{Cd}_{0.84}\text{Zn}_{0.16}\text{Te}$  barriers (see Fig 3.11). The indium doping density is estimated to be  $3 \times 10^{10} \text{ e}^-/\text{cm}^2$ . The graph in Fig. 3.11 plots the absorption spectrum at  $T = 10 \text{ K}$ , showing clearly resolved trion and heavy-hole (HH) exciton resonances, with a trion binding energy of 2.6 meV.

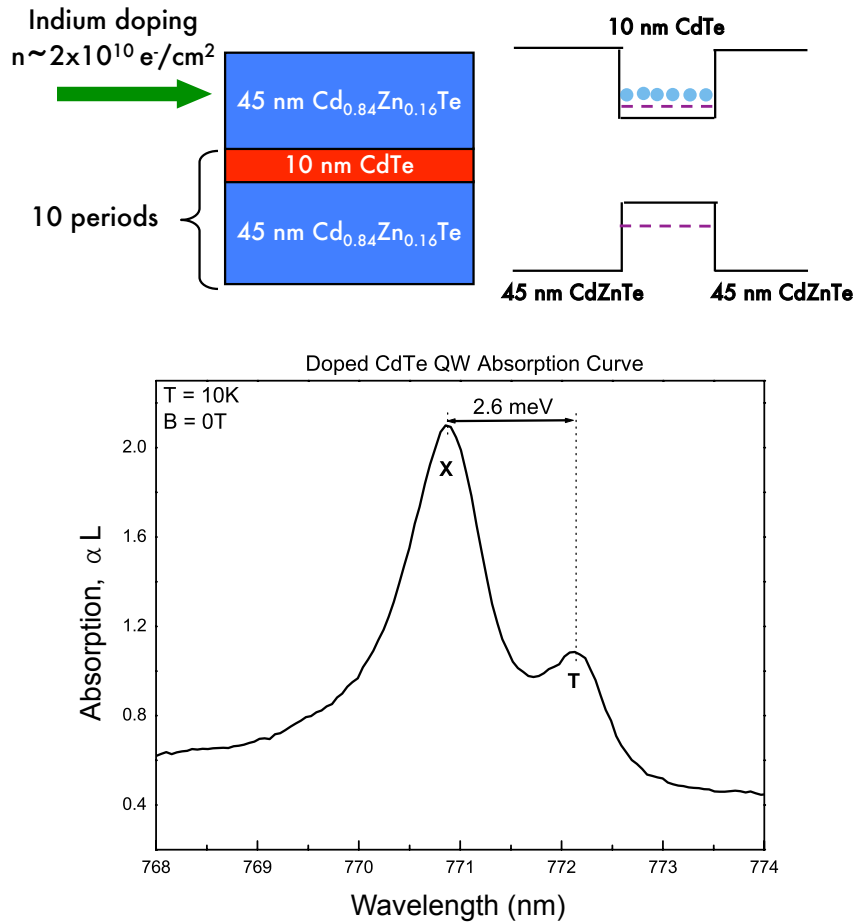


Figure 3.11: *Physical Structure and Absorption of a Modulation-Doped CdTe QW.* *Top:* The CdTe QW structure consists of 10 periods of 10 nm CdTe wells and 45 nm  $\text{Cd}_{0.84}\text{Zn}_{0.16}\text{Te}$  barriers, with indium doping in the barriers providing excess electrons in the CB of the CdTe QW. *Bottom:* The heavy hole exciton (X) and trion (T) are clearly resolved, separated by the trion binding energy of 2.6 meV.

As in the GaAs MTQW, a trion forms when an excess electron in the conduction band binds with an exciton. In the CdTe QW, the excess electrons are provided by the indium doping. The relevant energy level diagrams are the same as those depicted in Fig. 2.5. An in-plane magnetic field mixes the electron spin-up and spin-down states in the conduction band and enables dipole coupling to a common trion state, which produces a  $\Lambda$ -type three-level system.

### 3.6 Continuous Wave Results for Modulation-Doped CdTe QW

An identical experimental setup as that described in section 3.2 was used to probe the nonlinear response of the modulation-doped CdTe QW via DT. Fig. 3.12 shows the DT spectrum for the CdTe QW, where the pump beam is fixed at the trion absorption resonance. The CdTe exhibits the CZR signature spectrum with two resonance peaks symmetrically offset from zero detuning. Again, the asymmetry in the peak heights is due to the nonuniformity of the magnetic field lines produced by the permanent magnet used in the experiment. The energy separation between the two resonances is an order of magnitude larger than that of the GaAs MTQW CZR, at 18 GHz. This separation is expected, given the electron g-factor of the CdTe QW is a factor of five larger, at  $|g_e| = 1.4$ .

The striking difference between Fig. 3.6 and Fig. 3.12 is the comparative amplitudes of the CZR peaks. Whereas the GaAs MTQW peak corresponds to a small fraction of a percent of reduction in sample absorption, the higher energy CdTe CZR peak shows  $\sim 20\%$  reduction in absorption. This result is encouraging, and we will continue to pursue electron spin coherence studies using CdTe QWs in the next chapter, albeit in the transient regime.

### 3.7 Chapter Summary

In this chapter, we motivated our spectral-domain pump-probe study of Coherent Zeeman Resonance (CZR) in two semiconductor nanostructures with Electromagnetically Induced Transparency (EIT). Photoluminescence (PL) studies of a GaAs/AlAs mixed-type quantum well (MTQW) revealed trion formation by taking advantage of the unique optical tunability of the electron density in the wide well (WW) conduction band. Through the PL work, details of trion formation were

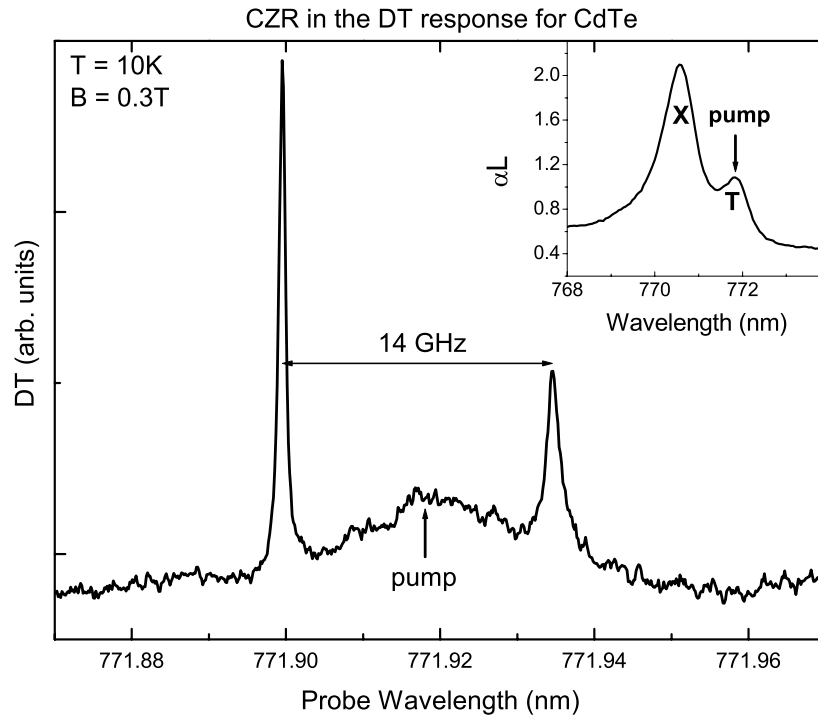


Figure 3.12: *CZR for a Modulation-Doped CdTe QW*. DT response for the CdTe QW obtained at  $B = 0.3$  T and  $T = 10$  K, with the pump energy at the trion absorption resonance. Sample absorption is shown in the inset, heavy hole exciton and trion absorption peaks labeled **X** and **T** respectively, with pump energy indicated by the arrow.

observed, including conversion of excitons into trions as well as trion formation temperature dependence.

An external in-plane magnetic field was used to modify the intrinsic selection rules of the system such that a  $\Lambda$ -type three-level system for electron spins via optical dipole transitions to trions was enabled. Continuous-wave differential transmission (DT) spectroscopy fostered the experimental realization of CZR arising from electron spin coherence between two Zeeman split electron energy levels in the MTQW. The role of trions was confirmed through a spectral study of the CZR.

Analytical solutions for the DT signal, derived from effective density matrix elements were shown to be in qualitative agreement with the experiment.

The role of manybody interactions was explored in the MTQW by injecting increasingly higher densities of electrons in the WW conduction band, while simultaneously monitoring the CZR signal in the DT. The result of the higher electron density was a suppression of the CZR amplitude with no appreciable broadening of the CZR linewidth. This result is understood as increased electron-exciton scattering destroying the dipole coherences, while the electron spin coherence remains intact.

Finally, encouraged by the robust electron spin coherence enabled by trions, but looking to minimize manybody effects which damage other quantum coherences, the spectral-domain pump-probe study of CZR turned to a modulation-doped CdTe QW. Strong CZR was observed, warranting further study of the system in the time domain in the next chapter.

## CHAPTER IV

TRANSIENT INITIALIZATION, DETECTION AND MANIPULATION  
OF ELECTRON SPINS

In the previous chapter we present spectral-domain resonance peaks in the differential transmission (DT) due to electron spin coherence via trions in two semiconductor nanostructures. In our studies of the GaAs MTQW, we see that manybody interactions can cause dephasing of the dipole coherences, reducing the resonance amplitude. This effect is obviously incompatible with the goal of achieving EIT. However, these studies are a promising demonstration of the robust nature of electron spin coherence enabled through trions. Thus motivated to find a nanostructure similarly supporting trions, but not suffering unduly from manybody interactions, we turned to a modulation-doped CdTe QW, which benefits from a larger trion binding energy than the GaAs MTQW.

Successfully observing Coherence Zeeman Resonance peaks in the spectral-domain, corresponding to a 20% reduction in the absorption, leads us to question how the EIT-like signal can be improved. We seek to understand how manybody processes affect the nonlinear optical response, which will be crucial for improving the reduction in absorption. Further, we are interested in manipulating the electron spin coherence within the lifetime of the coherence. In this vein, this

chapter supplements the steady-state experimental methods of the previous chapter with an ultrafast spectroscopic study of the modulation-doped CdTe QW.

This chapter begins with a discussion of a three-pulse differential transmission experimental setup, which adds a control pulse to a conventional pump-probe setup. Two synchronized pulsed lasers, a pulse-shaper and a spectrometer permit two-color spectroscopy in which each of the three pulses can be tuned to either the exciton or trion absorption resonance wavelength. Presentation of the experimental studies begins with two-pulse transient DT signals. We observe that detection wavelength—whether the probe is at the exciton or at the trion—causes a  $\pi$ -phase difference in the quantum beats. However, the pumping wavelength does not change the quantum beat behavior. We can infer the spin initialization process from these data, as well as hypothesize about the origins of the nonlinear optical responses.

We then present three-pulse two-color DT experiments. These studies reveal that a control pulse can dramatically alter the oscillatory nonlinear response of electron spin coherence when tuned to the exciton resonance and the signal is detected at the exciton wavelength. The response remains qualitatively the same when trions are injected. We discuss a model for these behaviors which involves an interplay between carrier heating generated by trion formation from excitons and manybody Coulomb effects such as exciton-polaron interaction. Injection of excitons at an appropriate time enables the effective manipulation of both the amplitude and phase of the oscillatory nonlinear response from electron spin coherence. In comparison to earlier studies, the manipulation takes place without electron spin rotation, opening up a new avenue for control as well as applications of electron spins in semiconductors.

#### 4.1 Time-Domain Differential Transmission Experimental Setup

For two-pulse DT, nearly transform-limited pump pulses with bandwidths of 0.4 nm and durations of 4 ps, are derived from a femtosecond mode-locked Ti:Sapphire laser (82 MHz repetition rate) with the use of an external pulse-shaper. The pulse shaper consists of four elements: a diffraction grating, a biconvex lens with focal length  $f$ , a mirror, and an adjustable slit. In the  $4f$  configuration, the grating separates the incoming pulse spatially and spectrally, and the slit, placed approximately at the focal plane of the lens is used to select the bandwidth. The pulse is recombined at the grating and exits the pulse shaper with the desired shape.

Probe pulses with a bandwidth of 5 nm come directly from the femtosecond Ti:Sapphire laser. After propagating through the sample, the probe is spectrally resolved by a spectrometer. In this way, changes in the probe transmission induced by the pump can be measured at a given wavelength using lock-in detection. The relative timing of the pump and probe is controlled by changing the path length of the pump beam, using a corner cube mounted on a programmable translation stage (see Fig. 4.1).

For two-color three-pulse DT, pump, control, and probe arrive at the QW sample at times  $t_1$ ,  $t_2$ , and  $t_3$ , respectively, as shown schematically in Fig. 4.1. The control, with a spectral bandwidth of 0.45 nm, comes from a picosecond mode-locked Ti:Sapphire laser that is synchronized with the femtosecond mode-locked Ti:Sapphire laser. In this setup, the probe can detect the DT response at either the trion or exciton resonance, while the pump and control can couple to either the trion or exciton transition.

The modulation-doped CdTe QW sample is identical to that used in the CZR experiments described in the last chapter in Section 3.5, with the absorption

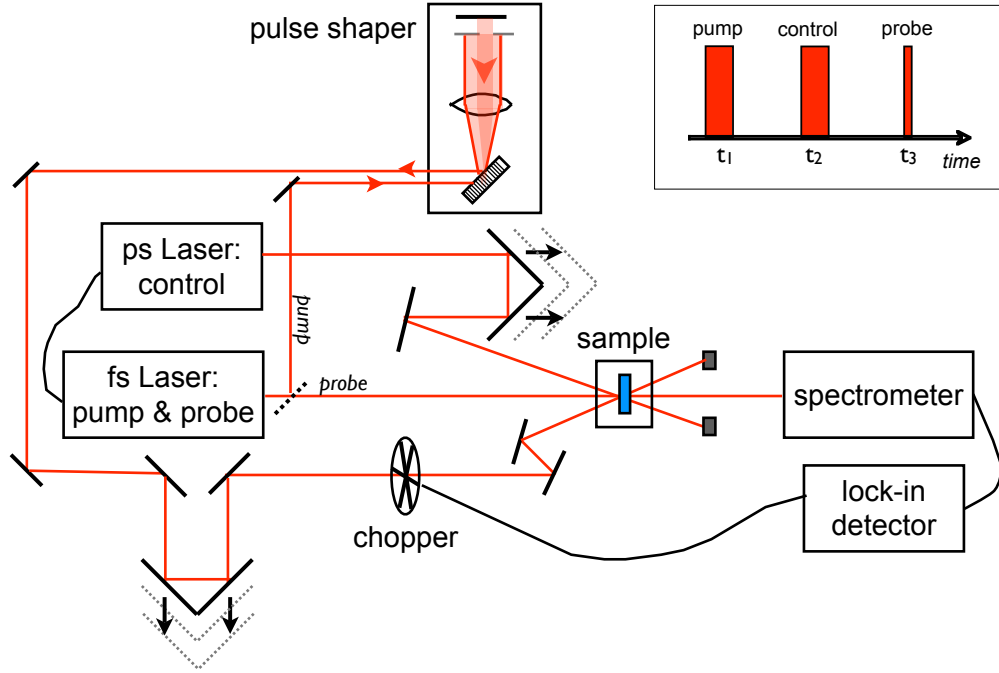


Figure 4.1: *Experimental Setup for Transient Differential Transmission.* The femtosecond (fs) laser provides both the pump and probe pulses for two-pulse DT. The pump's bandwidth is selected with an external pulse shaper, and its pathlength is scanned with a programmable translation stage in order to measure the transient DT. The spectrometer detects the DT signal in the probe direction at any given wavelength. For three-pulse DT, the picosecond (ps) laser repetition rate is synchronized with the fs laser. The ps serves as the control beam, whose relative timing to the probe is fixed with another translation stage.

spectrum shown in Fig. 3.11. All measurements in this chapter were carried out at  $T = 10$  K with the sample placed in an in-plane magnetic field ( $B \sim 0.4T$ ) along the  $x$ -axis (the growth axis is defined as the  $z$ -axis), as shown in Fig. 4.2a. All incident optical pulses have the same circular polarization unless otherwise specified.

As described in Section 2.4.1, when a CdTe QW is subject to a weak in-plane magnetic field, a  $\sigma+$  polarized field can enable a  $\Lambda$ -type three-level system. Two electron spin states,  $|s_x = -1/2\rangle$  and  $|s_x = 1/2\rangle$ , are coupled to a common trion state  $|t+\rangle$ , which consists of a hole with  $J_z = 3/2$  and a spin-up and spin-down

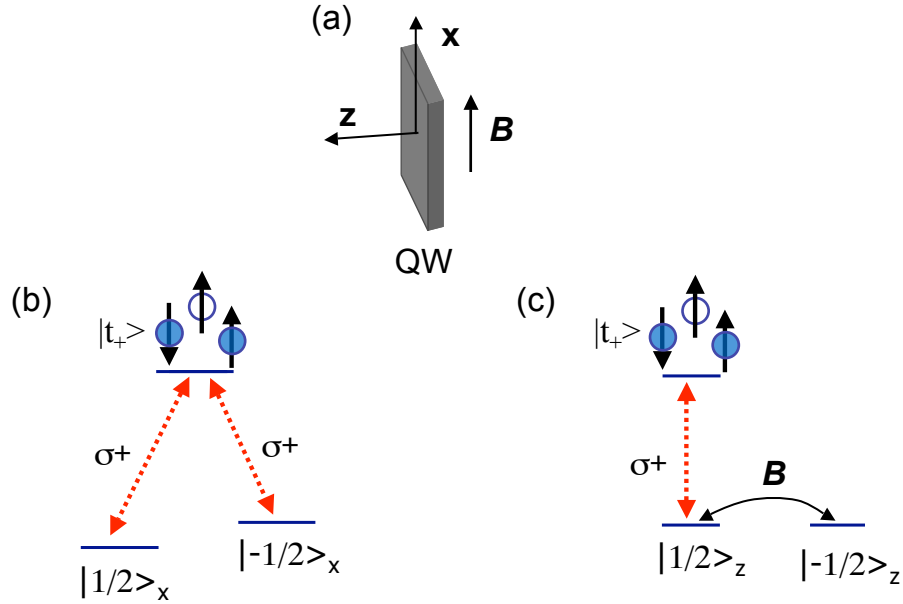


Figure 4.2: *Two Equivalent Three-Level Energy Diagrams.* (a) The direction of the external magnetic field in the Voigt configuration. (b) With the applied magnetic field, trion transitions from  $s_x = |1/2\rangle$  and  $s_x = |-1/2\rangle$  are enabled with  $\sigma^+$  polarized beams to form a  $\Lambda$ -type three-level system. (c) An approximate energy level scheme when the pump bandwidth is much greater than the electron Zeeman splitting.

electron as shown in Fig. 4.2b. In the limit that the pump bandwidth is large compared to the electron Zeeman splitting, transitions in the  $\Lambda$ -type system can be approximated as a transition between  $|t_+\rangle$  and electron spin state,  $|s_z = 1/2\rangle$ , as shown in Fig. 4.2c [32, 62]. In this model, the coupling of the  $|s_z = 1/2\rangle$  and  $|s_z = -1/2\rangle$  states by the external magnetic field leads to a precession of the electron spin around the  $x$ -axis. The electron spin coherence corresponds to the Larmor spin precession of spin-polarized electrons.

## 4.2 Spin Initialization and Detection

### 4.2.1 Resonant Trion Excitation

We first discuss two-pulse DT and the initialization of electron spin polarization. With an initial random orientation of electron spins in the two dimensional electron gas (2DEG) provided by the indium n-doping, the excitation of  $|t+\rangle$  by a pump pulse leaves a net spin-polarized electron population with  $|s_z = -1/2\rangle$  in the 2DEG, see Fig 4.3 [33, 62]. The spin-polarized electrons then precess around the external magnetic field, inducing periodic oscillations or quantum beats (QBs) in the DT response. In the absence of spin decoherence, the population of spin-polarized electron at  $|s_z = -1/2\rangle$  can be described as

$$n_-(t) = n_o \cos(\omega_B(t - t_1)), \quad (4.1)$$

where  $\omega_B$  is the Larmor frequency. For simplicity, we will focus on the dynamics of long-lived QBs and ignore the small amount of electron spin polarization generated by trion radiative recombination, which takes place within 100 ps [63].

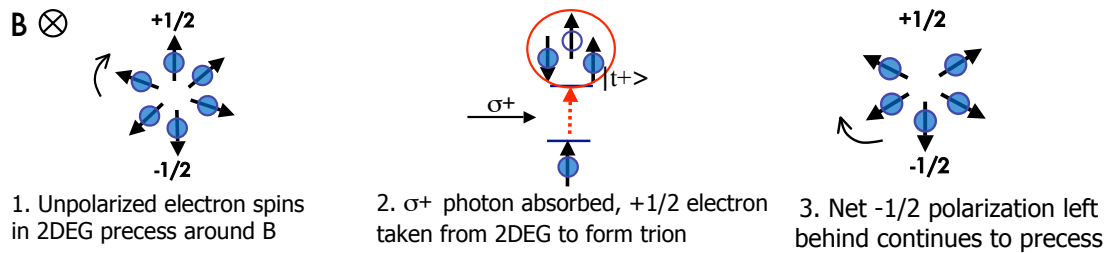


Figure 4.3: *Cartoon of Spin-Polarization Initialization using Trion Excitation.* Cartoon depicts how  $\sigma+$  polarized pump pulse, tuned to trion resonance initializes a net  $-1/2$  polarization in the 2DEG by taking a  $+1/2$  electron for trion formation, cartoon adapted from [62].

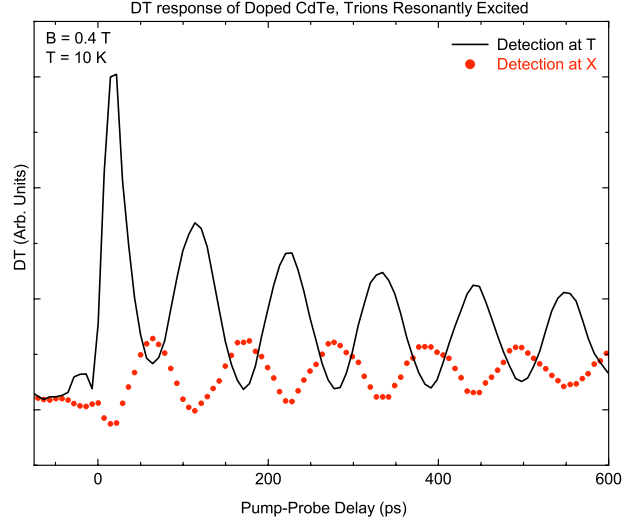


Figure 4.4: *Doped CdTe Two-Pulse Measurement: Resonant Trion Excitation.* Two-pulse DT responses obtained with the pump at the trion resonance. The solid curve is detected at the trion resonance, and the dotted curve is detected at the exciton resonance.

Fig. 4.4 shows two-pulse DT responses obtained with the pump at the trion resonance and detected at either the trion or exciton resonance. The DT responses feature QBs with  $\omega_B/2\pi = 9$  GHz, corresponding to  $|g_e| = 1.4$ . The QBs detected at the trion and exciton resonances feature a  $\pi$ -phase difference. Similar behaviors have also been observed in earlier time-resolved Kerr rotation studies [33, 62]. We note that electron spin polarization induced by trion radiative recombination would lead to a phase shift in the QBs, causing a deviation from the  $\cos[\omega_B(t - t_1)]$  or  $\sin[\omega_B(t - t_1)]$  behavior [33]. However, no significant phase shift is observed in the QBs shown in Fig. 4.4.

From the selection rules and spin polarization initialization process, we know that the peaks of the DT oscillation detected at the trion resonance and the valleys of DT oscillation detected at the exciton resonance occur when the spin-polarized

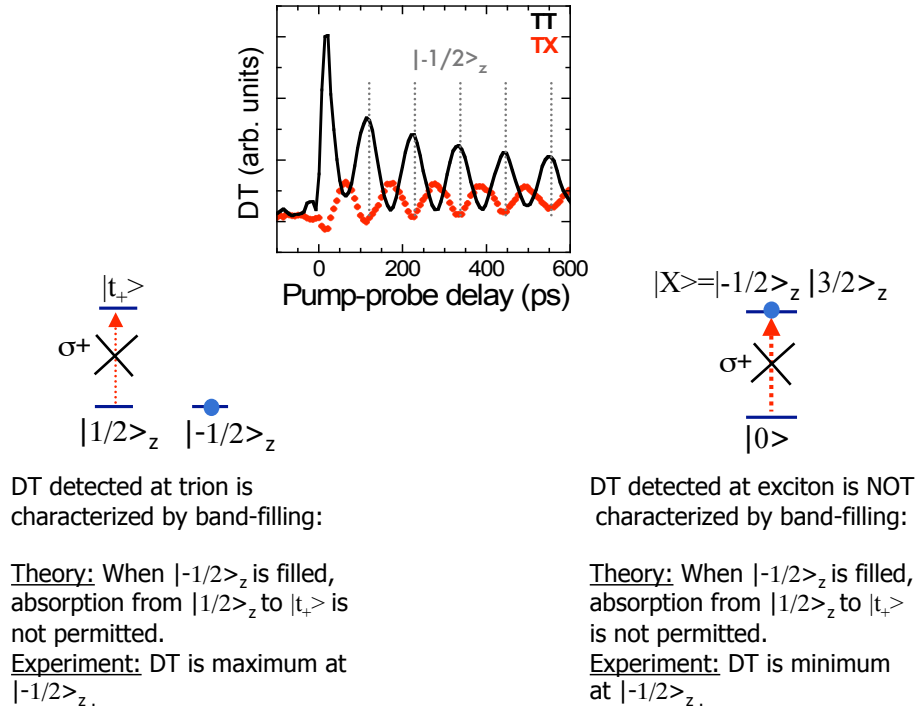


Figure 4.5: *Band-filling Cartoon for the Exciton and Trion.* While band-filling explains the DT signal detected at the trion, a different mechanism must be used to understand the DT signal detected at the exciton.

electrons are at  $|s_z = -1/2\rangle$ , see Fig. 4.5. For the DT detected at the trion resonance, the peak of the oscillation in the DT corresponds to a maximum bleaching of the optical absorption. This behavior is well explained by band-filling, because when the spin-polarized electrons are at  $|s_z = -1/2\rangle$ , the lower energy level for the trion transition,  $|s_z = 1/2\rangle$ , is left unoccupied. In contrast, the DT response at the exciton resonance can not be understood by band-filling alone because band-filling for the exciton transition also occurs when the spin-polarized electrons are at  $|s_z = -1/2\rangle$ . Yet the DT response at the exciton is a valley when the spin-polarized electrons are at  $|s_z = -1/2\rangle$ , not an absorption bleaching peak. We therefore posit that manybody interactions must be playing a dominant role in the DT response for the exciton, which will be discussed in detail in the next section.

### 4.2.2 Resonant Exciton Excitation

Spin-polarized electrons can also be initialized via resonant exciton excitation and subsequent trion formation, given that the trion formation time ( $< 30$  ps) is short compared with the electron spin decoherence time ( $\sim 1$  ns) [33, 62]. Specifically, excitons containing electrons with  $|s_z = -1/2\rangle$  form trions by capturing electrons with  $|s_z = 1/2\rangle$  from the 2DEG, leaving a net spin-polarized electron population with  $|s_z = -1/2\rangle$  in the 2DEG. This process is confirmed by the long-lived QBs shown in Fig. 4.6, where the pump is at the exciton resonance. Fig. 4.7 plots QB amplitudes as a function of the detection wavelength, where we obtained the QB amplitude by numerically fitting the QBs to

$$I_{QB} = Ae^{-\gamma(t_3-t_1)} \cos \omega_B(t_3 - t_1) \quad (4.2)$$

with  $A$  being the amplitude and  $\gamma$  being the spin decoherence rate. Comparing Fig. 4.4 and Fig. 4.6, we observe that QBs in the two-pulse DT responses exhibit qualitatively the same behavior, regardless of whether spin-polarized electrons are initialized by direct trion excitation or by trion formation from resonantly excited excitons.

The spectral dependence of the QB amplitude in Fig. 4.7 further shows that the loss in the trion transition strength is to a large extent compensated by the increase in the exciton transition strength, indicating that electron spin precessions have a minimal effect on the overall oscillator strength for the interband optical transition. This oscillator strength sharing or transfer between the exciton and trion resonances is in agreement with an earlier study on the electron density dependence of the exciton and trion absorption spectra in similar CdTe QW structures [64]. A microscopic theoretical analysis, beyond the scope of this dissertation, is needed in

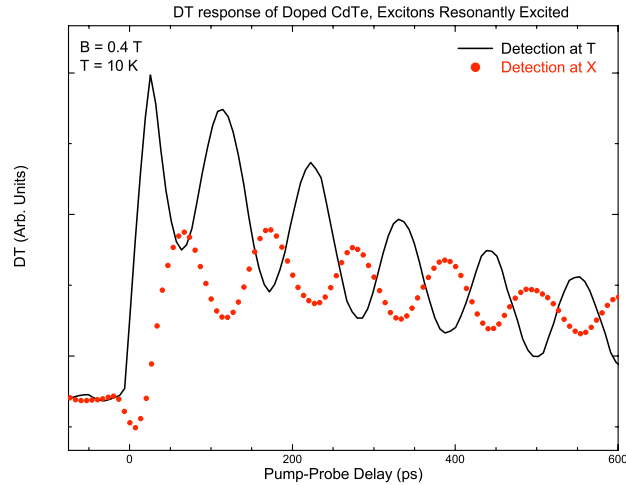


Figure 4.6: *Doped CdTe Two-Pulse Measurement: Resonant Exciton Excitation.* Two-pulse DT responses obtained with the pump at the exciton resonance. The solid curve is detected at the trion resonance, and the dotted curved is detected at the exciton resonance.

order to determine the underlying manybody interactions responsible for the increase in the exciton oscillator strength. However, a likely mechanism is the exciton-polaron effect. A spin-polarized electron cloud surrounding an exciton can induce changes in the effective mass of the constituent electron in the exciton, leading to corresponding changes in the exciton oscillator strength [65].

### 4.3 Three-Pulse DT Studies

With an understanding of spin polarization initialization and detection, gained from studies we present in the previous section, we now move on to three-pulse DT studies. A third pulse, called the control, arrives at the system after the pump has initialized the polarization. The timing of the control, as well as the energy resonance, can be varied. The role of the control pulse is to excite the excitons and trions far beyond equilibrium, and study the role of the induced

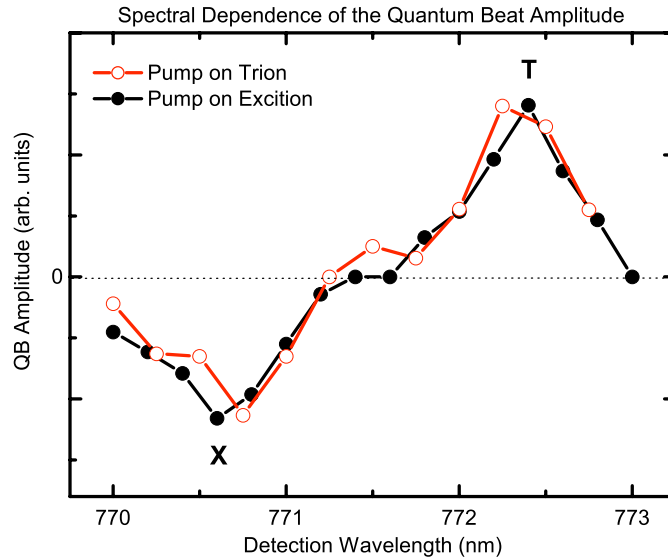


Figure 4.7: *Spectral Dependence of QB Amplitude.* Amplitudes of Quantum Beats (QBs) fitted to Eqn. 4.2 for a range of detection wavelengths. The open (closed) circles show QB amplitudes when pump at trion (exciton). The pump and probe intensities are  $0.3I_o$ , and  $0.1I_o$ , respectively, with  $I_o=5 \text{ W/cm}^2$ .

manybody interactions on the nonlinear optical response from spin coherence.

These experiments look toward the possibility of attaining ultrafast manipulation of the electron spins. A control pulse coupling to the trion transition can in principle result in a spin rotation via a geometrical phase shift [32], but no effects of spin rotation have been observed in our experimental studies. However, the control beam does serve to manipulate the nonlinear optical response when excitons are injected into the system, and the response is detected at the exciton resonance, as is shown in this section.

#### 4.3.1 Direct vs. Indirect Quantum Beats

For the three-pulse DT, spin-polarization, or  $n_-(t)$ , initialized by the pump can contribute to the DT response via two processes that feature distinct oscillatory

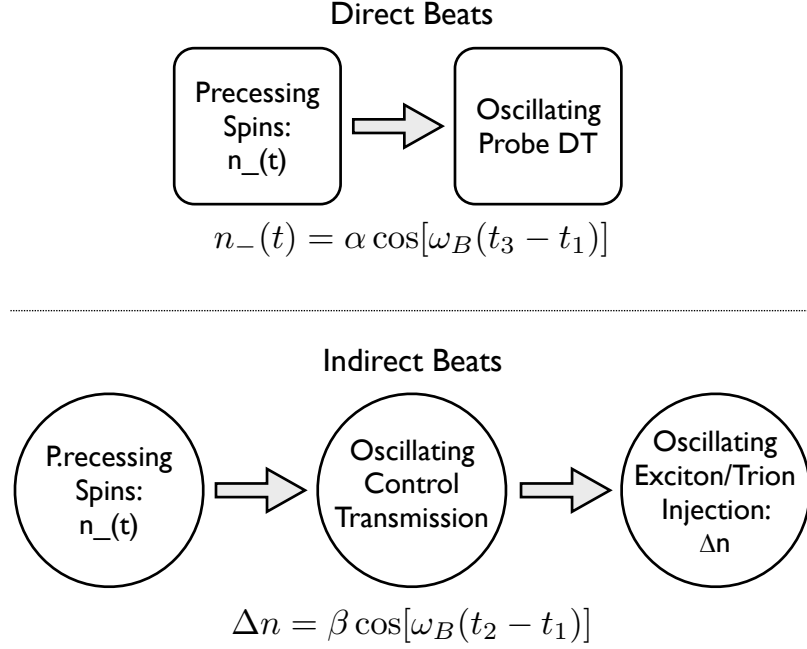


Figure 4.8: *Direct vs. Indirect QBs.* *Top:* The direct beats derive directly from the spin precession, and have a phase independent of the control timing. *Top:* The indirect beats correspond to an oscillation of the control transmission, which derives from the spin precession, and have a phase which is dependent on the control timing.

behaviors, see cartoons in Fig. 4.8. In the first process, the spin-polarization directly induces an oscillatory change in the probe transmission, leading to QBs with a phase that is dependent on  $t_3 - t_1$  and is independent of the control timing,  $t_2$ . This process is readily seen in the two-pulse DT experiments shown above in Section 4.2. In the second process, spin polarization initialized by the pump also induces an oscillatory change as a function of  $t_2 - t_1$  in the control transmission, leading to a corresponding change,  $\Delta n$ , in the trion or exciton population excited resonantly by the control. DT responses induced by  $\Delta n$  thus feature QBs with a phase that is dependent on  $t_2 - t_1$  and is independent of the probe timing,  $t_3$ . For brevity, we refer to QBs induced directly by  $n_-$  as *direct QBs* and QBs induced by  $\Delta n$  as *indirect QBs*. In the absence of any decay process, QBs in the three-pulse DT

response can be described as

$$I_{QB}(t_1, t_2, t_3) = \alpha \cos[\omega_B(t_3 - t_1)] + \beta \cos[\omega_B(t_2 - t_1)], \quad (4.3)$$

where  $\alpha$  and  $\beta$  are the amplitudes of the direct and indirect QBs, respectively. Because  $\Delta n$  derives from  $n_-$ , we know that  $|\Delta n| < |n_-|$ . We therefore expect  $|\beta|$  to be small compared with  $|\alpha|$ , and a correspondingly small effect from the indirect beats. However, we find that indirect QBs dominate in two specific configurations in the DT response. As we discuss below, these unusual nonlinear optical processes are otherwise inaccessible with two-pulse DT.

#### 4.3.2 Two-Color Three-Pulse DT Results

The DT responses are obtained as a function of the pump-probe delay, with a fixed control-probe delay,  $\tau = t_3 - t_2$ . By modulating the pump intensity and using lock-in detection, we eliminate control-induced nonlinear contributions that do not involve the pump. Because each of the three pulses are either resonant with the trion (T) or the exciton (X), eight experimental configurations can be studied, as shown in Table 4.1. For each configuration, we observe dependencies in the DT signal on the control timing and intensity. And as stated above, all experiments are performed at  $T = 10$  K and  $B = 0.4$  T.

The top graphs in Fig. 4.9 plot three-pulse DT responses obtained with the pump, control, and probe degenerate at the trion resonance, denoted TTT (configuration 1 from Table 4.1.) The control timing,  $\tau$ , is  $\pi/\omega_B$  and  $2\pi/\omega_B$  in the left and right graphs, respectively, indicated by arrows. The intensity of the control is increased from 0 to 80 mW/cm<sup>2</sup> from the top to the bottom of each graph. We observe a slight decrease in the overall QB amplitude with increasing control

Table 4.1: *Two-Color, Three-Pulse Experimental Configurations.* The three pulses can be tuned to either the trion (T) or exciton (X) absorption resonances, at  $\lambda = 772.5$  nm and 770.5 nm respectively. Checkmarks in the last column indicate configurations in which the control induced significant change in the nonlinear optical response through indirect QBs.

	Pump Color	Control Color	Probe Color	Ind. QBs
1	T	T	T	
2	T	T	X	
3	T	X	T	
4	T	X	X	✓
5	X	X	X	✓
6	X	X	T	
7	X	T	X	
8	X	T	T	

intensity, and for  $\tau = 2\pi/\omega_B$ , a small dip corresponding to the overlap of pump and control pulse becomes visible. But otherwise, there is no indication that the control pulse has an effect on the nonlinear optical response for the TTT configuration.

These three-pulse DT responses are dominated by the direct QBs.

The bottom graphs in Fig. 4.9 depicting experiments performed for the degenerate exciton configuration, XXX, show different results. For  $\tau = \pi/\omega_B$ , beyond a slight decrease in amplitude, the QBs remain unaffected by the addition of the control. However, for  $\tau = 2\pi/\omega_B$ , the results are qualitatively different. The QBs decrease in amplitude and then reemerge with a  $\pi$ -shifted phase as the control intensity is increased. We also note here that for both control timings, the initial coherent spike at zero-delay becomes suppressed with increasing control intensity.

The results of the experiments in Fig 4.9 are summarized by Fig 4.10. The QBs in the TTT configuration are independent of the control timing, whereas the QBs in the XXX configuration undergo a phase shift of  $\pi$  when the fixed control-probe delay is changed from  $\tau = \pi/\omega_B$  to  $\tau = 2\pi/\omega_B$ . Additional studies of

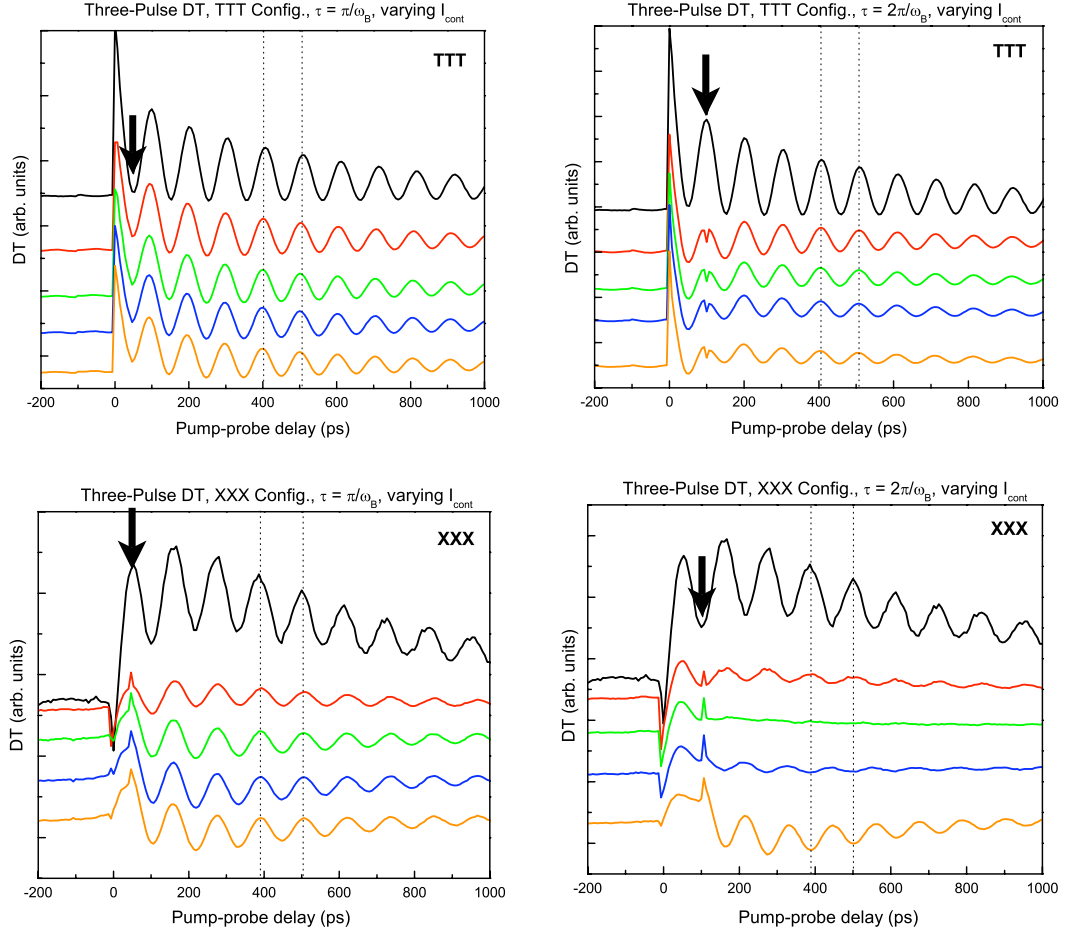


Figure 4.9: *3-Pulse DT: Degenerate on Trion and Exciton.* Three-pulse DT with a fixed control and probe delay. Pump, control, and probe degenerate at the trion, denoted TTT (*Top*) and at the exciton, XXX (*Bottom*). Pump and probe intensities are  $0.3I_o$  and  $0.1I_o$ , and the control intensities from top to bottom of each graph are  $0$ ,  $I_o$ ,  $5I_o$ ,  $10I_o$ , and  $16I_o$  with  $I_o = 5 \text{ mW/cm}^2$ . Control timings, indicated on each graph with an arrow, are *Left*:  $\tau = \pi/\omega_B$ , and *Right*:  $\tau = 2\pi/\omega_B$ .

the XXX configuration further confirm that under these conditions the phase of the QBs is independent of the probe timing, indicating that the three-pulse DT responses are now dominated by the indirect QBs.

We observe the indirect beats in only one of the six non-degenerate configurations, when the pump is resonantly exciting the trion, and the control and probe are both tuned to the exciton resonance, denoted TXX (see Fig. 4.11). As in

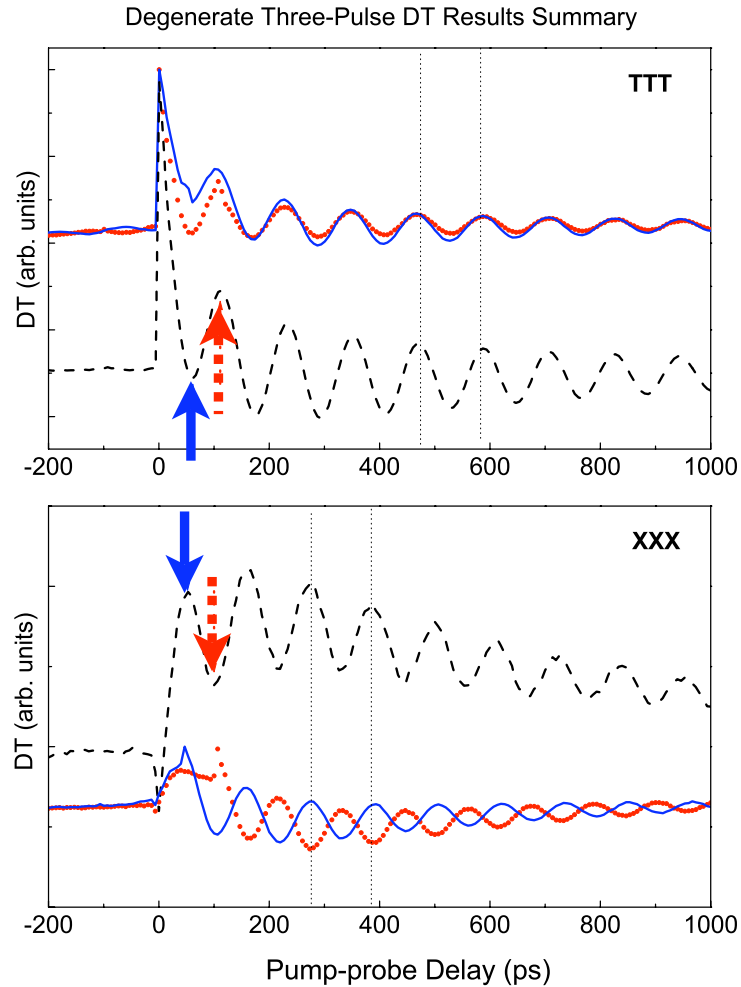


Figure 4.10: *3-Pulse DT: Degenerate Wavelengths Summary.* Summary of Fig. 4.9. Pump, control, and probe are degenerate at the trion, denoted TTT (*Top*) and at the exciton, XXX (*Bottom*). The dashed curves are the responses obtained with no control. The solid curves are the responses with  $\tau = \pi/\omega_B$ . The dotted curves are the responses with  $\tau = 2\pi/\omega_B$ . The arrows indicate the pump-probe delay, at which the control and pump overlap. Pump, control and probe intensities are  $0.3I_o$ ,  $20I_o$ , and  $0.1I_o$ , respectively, with  $I_o = 5 \text{ W/cm}^2$ .

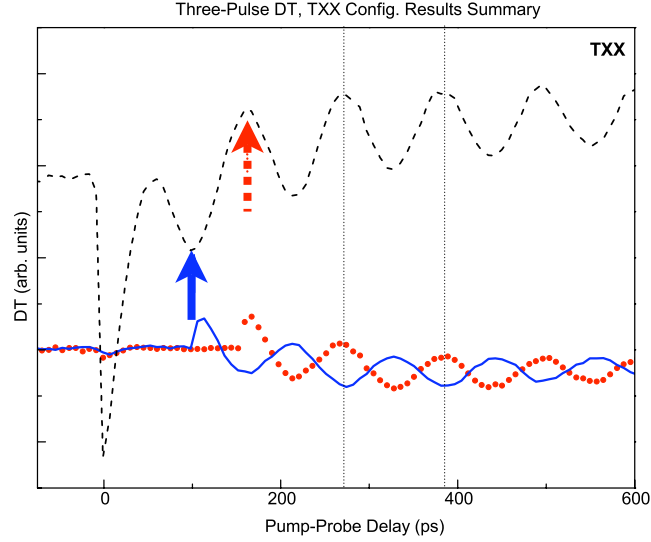


Figure 4.11: *3-Pulse DT: TXX Configuration.* Pump is resonant with the trion, while control and probe are at the exciton (TXX). Same conditions as in Fig. 4.10, except the dotted curve is the responses with  $\tau = 3\pi/\omega_B$ , instead of  $\tau = \pi/\omega_B$ .

the XXX configuration, the nonlinear optical response depends critically on the control timing. For TXX in Fig. 4.11, we show the response for  $\tau = 2\pi/\omega_B$  and  $3\pi/\omega_B$ , in order to better observe the effects of the control on the DT signal in the time the control precedes the pump. For XXX and TXX, the nonlinear response is  $\pi$ -phase shifted from the original two-pulse signal for all control timings  $\tau = m\pi/\omega_B$ , where  $m$  is an even integer. If  $m$  is an odd integer, the three-pulse DT response is in phase with the original two-pulse signature.

All other configurations look qualitatively the same as configuration TTT, in that the control timing does not affect the nonlinear optical response, and the overall effect of the control is little more than an amplitude suppression of the QBs. We show two representative plots for the direct beats-dominated configurations in Fig. 4.12.

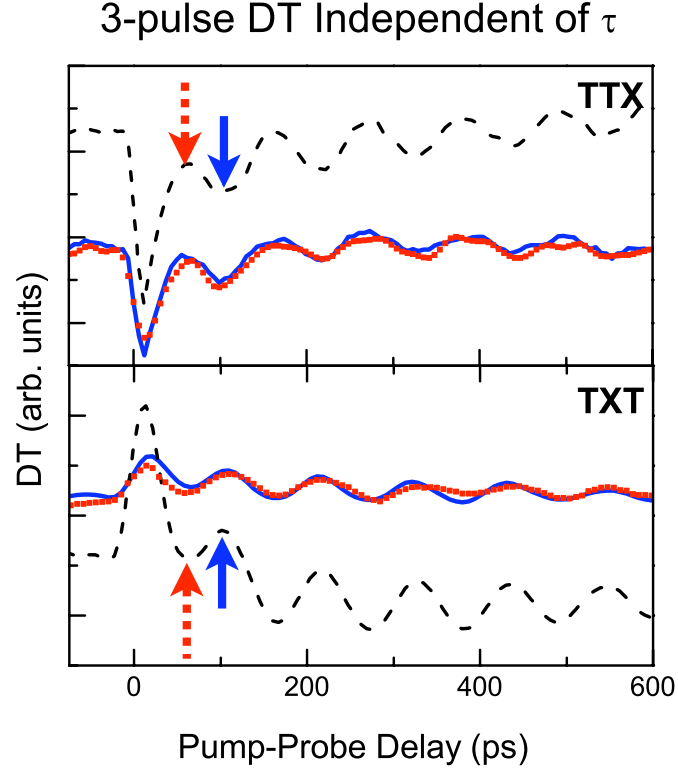


Figure 4.12: *3-Pulse DT: Configurations TTX and TXT*. Same conditions as in Fig. 4.10, for the TTX and TXT configurations.

#### 4.3.3 Analysis

The left graph in Fig. 4.13 shows the dependence of the TXX QBs on the control intensity with  $\tau = 2\pi/\omega_B$ , under otherwise similar conditions as those used in Fig. 4.11. Just as in the XXX graph in Fig. 4.9, with increasing  $I_{control}$ , the QB amplitude decreases and then eventually flips sign. This behavior indicates that  $\alpha$  and  $\beta$  have opposite signs.

Recalling that the control timing,  $\tau$ , is defined by the control-probe delay,  $\tau = t_3 - t_2$ , we can rewrite Eqn. 4.3, as follows:

$$I_{QB}(t_1, t_2, t_3) = \alpha \cos[\omega_B(t_2 - t_1) + \omega_B\tau] + \beta \cos[\omega_B(t_2 - t_1)]. \quad (4.4)$$

If  $\tau = n\pi/\omega_B$ , where  $n$  is an even integer, Eqn. 4.4 reduces to

$$I_{QB}(t_1, t_2, t_3) = (\alpha + \beta) \cos[\omega_B(t_2 - t_1)] \quad (4.5)$$

by virtue of the  $2\pi$  periodicity of the cosine function, and the QBs have an overall amplitude of  $\alpha + \beta$ . Similarly, if  $\tau = m\pi/\omega_B$ , where  $m$  is an odd integer, Eqn. 4.4 reduces to

$$I_{QB}(t_1, t_2, t_3) = (\beta - \alpha) \cos[\omega_B(t_2 - t_1)]. \quad (4.6)$$

and the overall QB amplitude is  $\beta - \alpha$ . If we add the signals expressed in Eqns. 4.5 and 4.6, we obtain a signal whose overall amplitude is  $2\beta$ . Likewise, if we subtract the two signals, we obtain a signal whose overall amplitude is  $2\alpha$ . The right graph in Fig. 4.13 shows  $|\alpha|$  and  $|\beta|$  as a function of  $I_{control}$ .  $|\alpha|$  and  $|\beta|$  were obtained by numerically fitting the sums and differences of three-pulse DT responses in the TXX

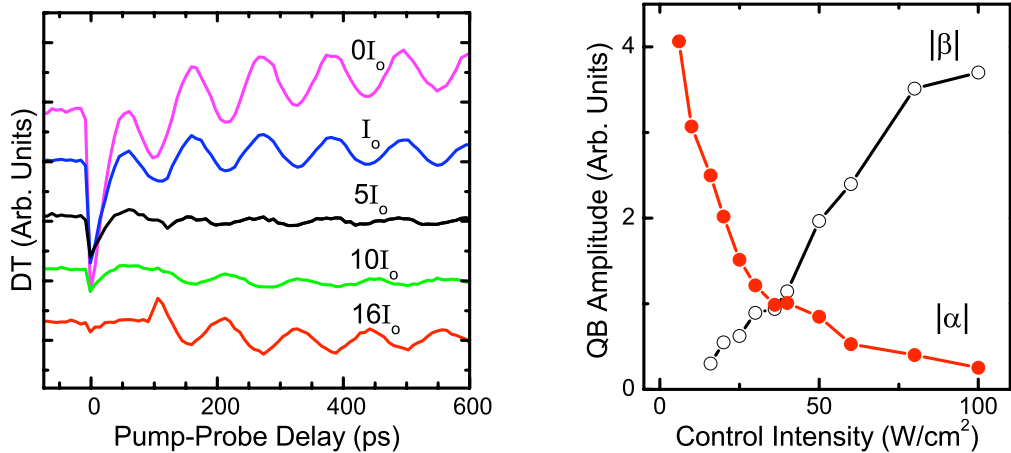


Figure 4.13: *Control Intensity Dependency of  $|\alpha|$  and  $|\beta|$ .* *Left:* Control intensity dependence of three-pulse DT responses obtained under conditions otherwise similar to those for Fig. 4.11. The control intensities used are 0,  $I_o$ ,  $5I_o$ ,  $10I_o$ , and  $16I_o$  with  $I_o = 5 \text{ mW/cm}^2$ . *Right:* Closed (open) dots show the amplitude modulus for direct (indirect) QBs.

configuration with  $\tau = 2\pi/\omega_B$  and  $\tau = 3\pi/\omega_B$ . At high  $I_{control}$ ,  $|\beta|$  far exceeds  $|\alpha|$ , which is unexpected as discussed in Section 4.3.1. In the next section we offer a model as to why the indirect beats dominate at high control intensities when injecting excitons and detecting at the excitonic resonance.

Note that with  $\tau = \pi/(2\omega_B)$ , the direct and indirect QBs have a phase difference of  $\pi/2$ , as can be seen from Eqn. 4.3. In this case, exciton injection varies the phase of the overall QBs by changing the relative contributions of the direct and indirect QBs. This phase manipulation is similar to earlier three-pulse DT studies in an excitonic system [34]. The underlying physics, however, is qualitatively different, as we discuss below. In particular, in the 2DEG, the manipulation of the QBs takes place without electron spin rotation.

#### 4.3.4 Discussion

We have shown that resonant excitation of trions and excitons initializes spin-polarized electrons and produce similar two-pulse DT responses. Figs. 4.10 and 4.11, however, reveal the surprising result that the color of the control pulse—whether it is applied at the exciton or trion resonance—makes a qualitative difference in the three-pulse DT response at the exciton resonance. There is an important distinction, which we have not yet discussed, between resonant trion excitation and trion formation from resonantly excited excitons. For the latter case, the excess energy, determined by the trion binding energy, is absorbed by the 2DEG via rapid carrier-carrier scattering (and at longer timescales by the crystal lattice), leading to heating of the 2DEG. In the limit that a large fraction of electrons in the 2DEG are converted to trions via interactions with excitons, the increase in the electron temperature can be very significant,  $\sim 10$  K. (The heating of a single

electron by the amount of the trion binding energy, which is 2.5 meV, can lead to an increase in temperature by 30 K. Under strong excitonic excitation, a large fraction of the electrons bind with excitons. The initial increase in the electron temperature can thus be on the order of 10 K.)

The initial transient behavior of three-pulse DT responses provides a direct signature of the interplay between carrier heating and manybody effects. As shown in Fig. 4.11, a strong control at the exciton resonance completely quenches the DT response, including the direct QBs, when the control precedes the pump (note that at zero pump-probe delay, the control precedes the pump by  $\tau$ ). It is well known that in a 2DEG, manybody effects, such as exciton-polarons and Fermi edge singularities, depend strongly on carrier temperature and are highly susceptible to carrier heating [65, 66]. Carrier heating generated by trion formation from excitons can thus weaken or quench DT responses, such as the direct QBs at the exciton resonance, that are induced by the manybody effects. In comparison, direct QBs detected at the trion resonance but under otherwise the same conditions persist, as shown in the bottom graph in Fig. 4.12. These nonlinear responses arise from band-filling and are thus more robust against carrier heating.

Carrier heating can quench direct QBs, but can also serve as a nonlinear mechanism for indirect QBs, which arise when the control arrives after the pump. For the indirect QBs in Fig. 4.11, spin-polarized electrons initialized by the pump induce a change,  $\Delta n$ , in the exciton population excited by the control. This induced change takes place before the formation of trions and is thus not affected by carrier heating. In this case,  $\Delta n$  can contribute to the DT response by inducing an oscillatory change (as a function of  $t_2 - t_1$ ) in carrier heating associated with the subsequent trion formation. Carrier heating as a nonlinear mechanism for the indirect QBs also accounts for the sign difference between  $\alpha$  and  $\beta$  shown in Fig.

4.13. A detailed theoretical description on how carrier heating affects the manybody interactions, however, still remains a difficult theoretical problem.

#### 4.4 Chapter Summary

In summary, this chapter presents three-pulse DT studies in a modulation-doped CdTe QW. These studies show that injection of excitons into a 2DEG by a control pulse can significantly alter the oscillatory nonlinear response from electron spin coherence when detected at the exciton resonance. However, the response remains qualitatively the same when trions are injected. These behaviors are unexpected since in two-pulse DT, resonant excitation of trions and excitons produces similar nonlinear responses. We attribute these surprising nonlinear optical processes to an interplay between manybody effects and carrier heating generated by trion formation from excitons. Exciton injection at an appropriate time provides an effective tool for manipulating the oscillatory nonlinear response from electron spin coherence. The physical insights gained from these studies are important for the understanding of coherent nonlinear optical processes in semiconductors. Our experimental results should also stimulate further theoretical efforts in developing a microscopic description for coherent optical interactions in an interacting electron spin system in semiconductors.

## CHAPTER V

## TRANSIENT ROTATIONS OF LOCALIZED ELECTRON SPINS

## 5.1 Introduction

Experimental studies presented in the preceding chapters have focused on electron spins in QWs, for which the motion of electrons in the CB is quantized along the direction of the QW growth axis. For these systems, manybody Coulombic interactions between optical excitations including excitons and trions play an essential role in understanding optical properties of electron spins. In this chapter, we turn our attention to localized electron spins, for which the motion of electrons is quantized in all three dimensions and interactions between relevant electron spins play only a minor role.

This chapter begins with a discussion of the motivations for studying donor-bound electrons. Photoluminescence and absorption spectra from bulk GaAs are then shown to characterize the donor-bound exciton system. The characterization studies reveal issues with crystal strain when the etched sample is adhered to a sapphire substrate, and prominent thin film Fabry-Pérot fringe features when the sample is free-standing. Using the free-standing sample, a spectrally sharp pump initializes donor-bound electron spin coherence via dipole-coupling to the bound exciton, and the induced spin polarization precesses

around an externally applied magnetic field. As a result long-lived quantum beats on the order of 10 ns are observed. The nonlinear spectrum exhibits two prominent resonances arising from the donor-bound exciton and an excited state of the donor-bound exciton. We observe that the quantum beat amplitude and phase is dependent on the detection wavelength across the nonlinear spectrum. Quantum beats detected at the donor-bound exciton are  $\pi$ -out-of phase from QBs detected at its excited state. Pump intensity studies reveal a QB amplitude and phase dependence on the excitation intensity. This dependency is approached through a density matrix formulation, and an interpretation of the role of the pump intensity is given. Finally, we conclude this chapter with a summary and look to the next chapter on the outlook of future directions of this research.

## 5.2 Motivation for Donor-Bound Electrons

Localized electron spins in a semiconductor are a paradigmatic system for investigating fundamental decoherence processes in a solid state environment. For single localized electron spins and at temperatures below a few K, incoherent electron spin flips as well as spin decoherence by phonon scattering can be suppressed by a relatively large electron Zeeman splitting. Spin decoherence, however, can arise from the coupling between an electron spin and the surrounding mesoscopic nuclear spin bath [13, 14, 27]. In semiconductors such as GaAs, the coupling to the nuclear spin bath limits decoherence time ( $T_2^*$ ) to approximately 5 to 10 ns [67], even though the spin lifetime is many orders of magnitude longer [68, 69].

Quantum decoherence, while inevitable, can in principle be mitigated with dynamical decoupling. The simplest example is the Hahn echo, in which a single

$\pi$ -pulse coherently flips the electron spins and reverses dephasing arising from static inhomogeneous broadening. A sequence of  $\pi$ -pulses, such as the Carr-Purcell or the concatenated sequence, repeating on a timescale much shorter than the bath correlation time can in principle suppress dephasing due to dynamical interactions with a nuclear spin bath [27]. A recent theoretical study by Uhrig discovered a special sequence of  $\pi$ -pulses for which the number of  $\pi$ -pulses scales linearly, instead of exponentially, with the improvement in decoherence time [70, 71].

Recent experimental efforts on localized electron spins in semiconductors have focused on electrons in quantum dots (QDs). Most of these studies, however, are complicated and hindered by the large inhomogeneous broadening of optical transitions common to even the best epitaxially grown QDs. An alternative system for localized electron spins is donor-bound electrons in semiconductors. Neutral donors are naturally-formed QDs, but without the complication of large inhomogeneous broadening. Since each donor-bound electron is in a similar local environment, the inhomogeneous absorption linewidth for donor-bound excitons ( $D^0X$ ) can be a few orders of magnitude smaller than that of quantum dot systems. For example, in high purity n-type GaAs, the absorption linewidth for the  $D^0X$  transition can be as small as  $10 \mu\text{eV}$ .

As we will discuss in the following chapter in the context of future research directions, the longer term goal of research in this area is to decouple electron spins from the surrounding nuclear spin bath with dynamical decoupling, thus protecting the electron spins from decoherence. The goal of the experimental study presented here is to demonstrate the optical excitation and detection of donor-bound electron spins and to determine the decoherence time set by the hyperfine interaction between the electron and the nuclear spin bath. These results pave the way for future work on optical spin echo studies of localized electron spins.

### 5.3 Characterization of Donor-Bound Electron System

The semiconductor material studied in this chapter is a high-purity bulk GaAs sample 10  $\mu\text{m}$  thick; it was grown by John Prineas at the University of Iowa. The purity of the sample limits the density of neutral donors present at low temperatures. These neutral impurities efficiently attract excitons via van der Waals interactions. The photoluminescence (PL) in Fig. 5.1 reveals the characteristically sharp and strong emission peak associated with recombination of excitons bound to neutral donors, or  $D^0X$  [72]. The large peak appearing 0.5 nm blue of the  $D^0X$  peak is emission associated with the free excitons, labeled X. Further, we have identified the emission peak associated with the ionized-donor-bound exciton,  $D^+X$ , based on previous findings [73]. The small peaks appearing between the  $D^0X$  and X are excited states of the  $D^0X$  [74].

The absorption spectrum of bulk GaAs, affixed to a sapphire disk, and measured at  $T = 4$  K exhibits prominent HH and LH resonances (see Fig. 5.2). In a perfectly symmetric bulk GaAs sample, the LH and HH excitons are degenerate, as described in Section 2.1, with their common resonance peak appearing just red of the band edge. But as we can see in Fig. 5.2, this degeneracy is lifted by stress on the crystal structure induced by the sample's adherence to the sapphire disk. We note here that this form of symmetry-breaking red-shifts the LH exciton resonance a few nm more than the HH exciton, also seen in [75]. Whereas when the degeneracy is lifted via 2D quantum confinement, the HH exciton resonance red-shifts more than that of the LH exciton. As an example, refer to the absorption spectrum of GaAs MTQW in Fig. 3.9.

The inset of Fig. 5.2 shows an enlargement at the base of the LH exciton absorption resonance. The sharp resonance at 821.9 nm, 0.5 nm red of the LH, is

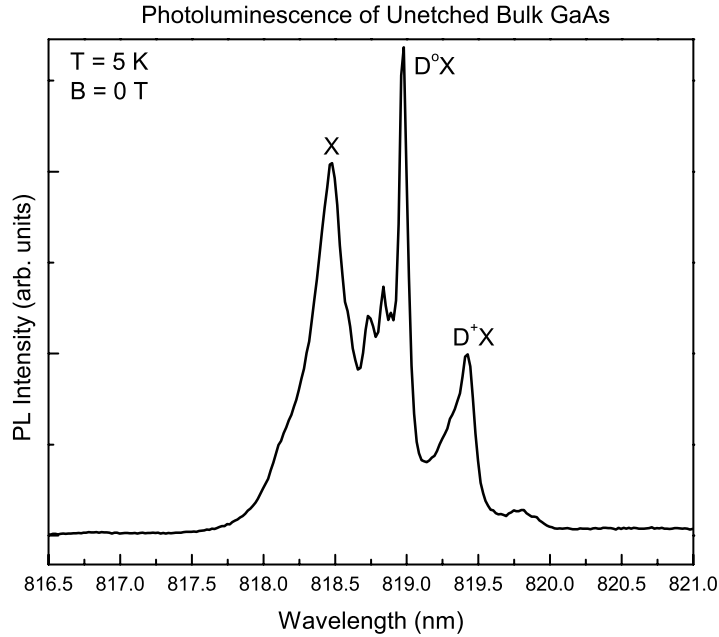


Figure 5.1: *Photoluminescence Emission Spectrum of Bulk GaAs*. Photoluminescence of unetched bulk GaAs. We label the narrow emission characteristic of recombination of excitons bound to neutral donors ( $D^0X$ ), as well as free excitons (X), and excitons bound to ionized donors ( $D^+X$ ). Small peaks between  $D^0X$  and X are excited states of the  $D^0X$ . Spectrum provided courtesy of Dr. Mats Larsson.

attributed to  $D^0X$  absorption, with a width of about 0.07 nm. The peak at 821.7 nm, is attributed to the first excited state of the  $D^0X$ .

The prominent fringes seen in Fig 5.2 are due to Fabry-Pérot interference in the presence of a wavelength-dependent absorption coefficient, observed in thin films [76]. The wavelength-dependent periodicity of the fringes can be understood by using analysis based on multibeam interference within a plane plate parallel [77]. We can readily observe that fringe size gets shorter as wavelengths approach the strong excitonic absorption resonance.

In order to minimize strain-induced broadening effects, we used a custom-built sample holder to mount an etched sample without a sapphire

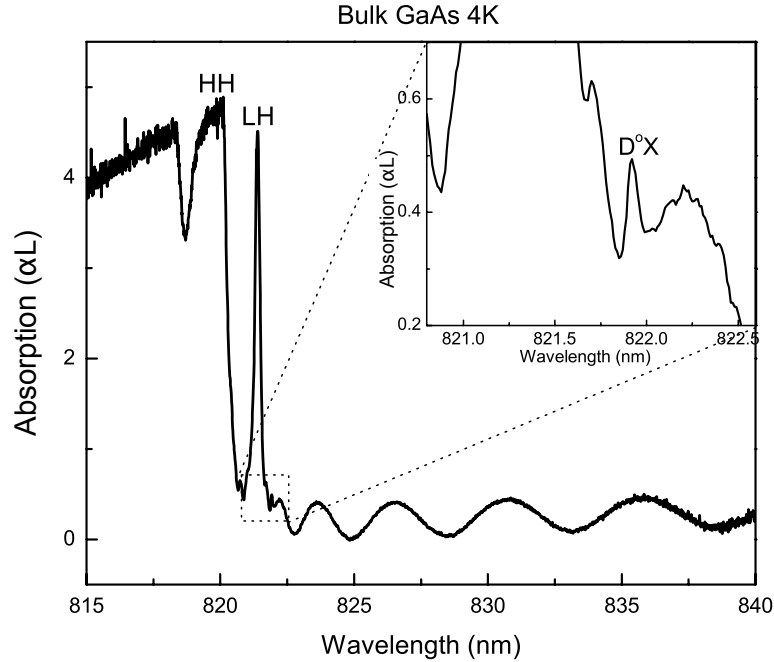


Figure 5.2: *Absorption Spectrum of Bulk GaAs.* Absorption spectrum taken at  $T = 4$  K and  $B = 0$  T, of a bulk GaAs sample affixed to a sapphire substrate. Heavy hole (HH) and light hole (LH) excitons are labeled, as is the neutral donor-bound exciton  $D^0X$  in the figure inset.

substrate. We refer to this sample as “free-standing,” because the  $10 \mu\text{m}$  thick sample was vertically caged within a  $100 \mu\text{m}$  deep frame without the use of an adhesive substance. The absorption spectrum of the free-standing GaAs sample (see Fig. 5.3) shows that the LH exciton absorption resonance merges with the HH exciton resonance in the stress-reduced conditions of the free-standing geometry. We observe that the HH exciton absorption is less broad. Unfortunately, the Fabry-Pérot interference fringes become enhanced by the boundary conditions of the free-standing structure. The sharp  $D^0X$  absorption feature observed in Fig. 5.2 appears to be overwhelmed by these fringe features. The nonlinear experiments in this chapter, however, were performed on the free-standing sample. These studies reveal long-lived nonlinear signals attributable to electron spin coherence in the

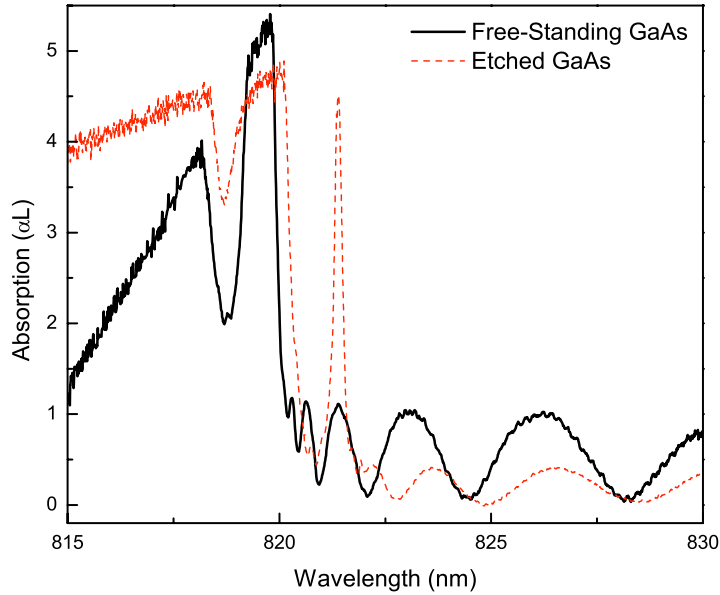


Figure 5.3: *Absorption Spectra: Free Standing vs. Sapphire-Affixed Bulk GaAs.* Absorption spectrum from the free-standing GaAs sample is overlaid with etched GaAs absorption spectrum shown in Fig. 5.2.

wavelength region we expect to observe the  $D^0X$ , which is approximately 0.6 nm red of the exciton absorption peak.

## 5.4 Transient DT of Donor-Bound Electrons

### 5.4.1 Experimental setup

Two pulses, both derived from the same picosecond laser, are incident on the sample. Their relative arrival time is controlled by a programmable delay stage. The probe pulse derives directly from the laser with a width of 0.45 nm, and a duration of 6ps. The pump pulse is narrowed by an external pulse-shaper (as discussed in Section 4.1) to match the  $D^0X$  linewidth, with a width of 0.05 nm and a corresponding duration of 25 ps. As in the previous chapters, the nonlinear

experiments are performed in the DT; the pump beam is modulated using a mechanical chopper and the signal along the probe beam is measured via lockin detection. Light fields are co-circularly polarized unless otherwise noted. The experiments were carried out at  $T = 2.5$  K, unless otherwise noted, in a superconducting magnet cryostat in order to provide a variable magnetic field.

#### 5.4.2 *The $D^o - D^oX$ $\Lambda$ -type System*

A  $\Lambda$ -type three-level system for donor-bound electrons,  $D^0$ , is formed by dipole coupling both spin states of a  $D^0$  to the  $D^0X$  ground state, see Fig. 5.4. To enable this system, an external magnetic field must be applied to mix the electron spin states, as was necessary in the two previously discussed semiconductor nanostructures. The  $D^0$  spin states are Zeeman split by the magnetic field. However, if this splitting is much smaller than the pump bandwidth, we can consider an equivalent energy level diagram [32], also shown in Fig. 5.4. Another way of stating the condition for equivalency is that the Larmor precession period,  $2\pi/\omega_B$ , must be long compared to the pump pulse duration time. The L-type system consists of one dipole-allowed transition between an electron spin state in the z-basis and the  $D^0X$  state. The two spin states remain coupled to each other via the B-field, indicated on the diagram with the curved arrow labeled  $\omega_B$ .

#### 5.4.3 *Transient Response of the Nonlinear Signal*

The transient differential transmission response is measured by varying the delay time of the probe and measuring the amplitude of the nonlinear signal. We see a sharp peak at zero delay corresponding to a temporal and spatial overlap of the pump and probe pulses in the sample. The pump initializes the electron spin

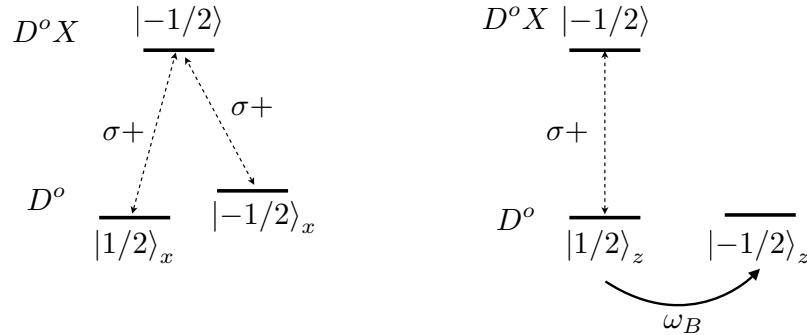


Figure 5.4: *The  $D^0 - D^0X$   $\Lambda$ -type System.* *Left:* A  $\Lambda$ -type three level system for donor-bound electrons,  $D^0$  are formed by dipole coupling to the  $D^0X$  ground state. The  $D^0$  states are labeled by electron spin, and  $D^0X$  state is labeled by its constituent hole spin. Selection rules are given in the presence of an externally applied magnetic field in the Voigt geometry. *Right:* An L-type three-level system equivalent to left diagram when the Larmor precession period,  $2\pi/\omega_B$ , is slow compared to the pump pulse duration time.

coherence or polarization at zero delay, and the presence of the magnet causes the spin polarization to precess. The probe measures the precession, and we observe quantum beats in the DT.

For optimal experimental conditions, such as limited pump scatter into the detector and superior spot overlap in the sample, the measured  $D^0$  spin coherence outlasts the 12 ns repetition rate of the laser. In Figure 5.5, quantum beats appear before the pump has arrived at zero delay. These oscillations are quantum beats initialized in the previous pump cycle.

The amplitude and phase of the quantum beats depend on several parameters. One parameter that strongly affects the nature of the oscillations is the detection wavelength. Using a spectrometer, the detection wavelength can be narrowed to a 0.01 nm window.

With the pump tuned to 819.85 nm, which is 0.1 nm red of the expected  $D^0X$  resonance, a nonlinear spectrum can be observed in the differential

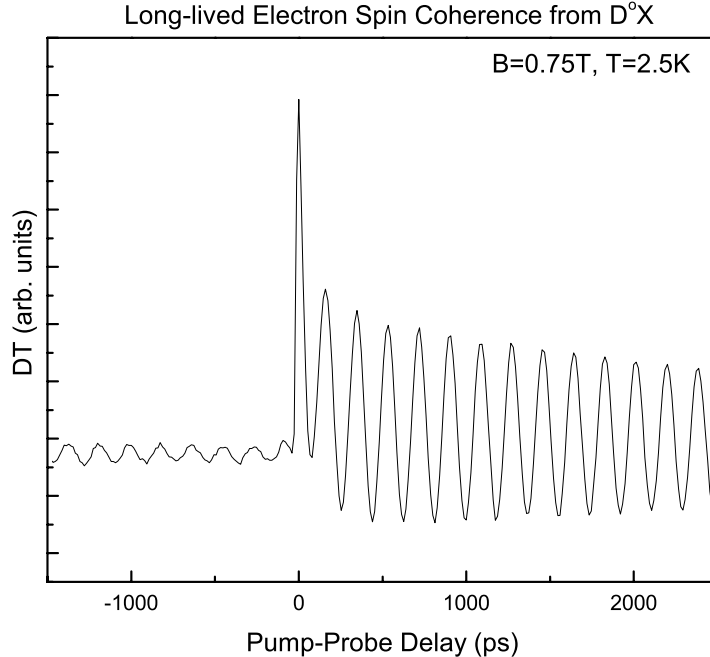


Figure 5.5: *Long-lived QBs from Donor-Bound Electrons.* Spin coherence from  $D^0$  observed in the DT as long-lived quantum beats. The oscillatory signal present at negative delay times are quantum beats initialized in the previous pump cycle, 12 ns earlier.

transmission at zero delay (see right plot in Fig. 5.6). We observe two nonlinear peaks emerge at temperatures  $T < 5$  K, at 819.85 nm and 819.52 nm. We attribute the lower energy nonlinear resonance to the ground state  $D^0X$ , and the higher energy nonlinear resonance to an excited state of the  $D^0X$ .

The transient nonlinear response for a range of detection wavelengths across the nonlinear spectrum is shown in the left plot of Fig. 5.6. The detection wavelength of each curve is indicated on the right graph of Fig. 5.6 by the heavy dots. The two bold curves in the left graph of Fig. 5.6 are detected at the peaks of the nonlinear spectrum, i.e. from the  $D^0X$  and its excited state. The quantum

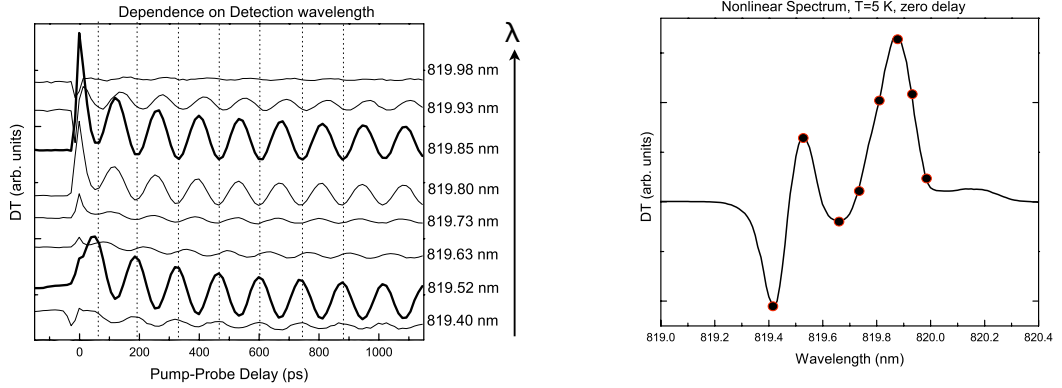


Figure 5.6: *Nonlinear Signal Detected over a Range of Wavelengths.* *Left:* The transient nonlinear response of the system at eight detection wavelengths, starting at  $\lambda = 819.40$  nm for the bottom curve, up to  $\lambda = 819.98$  nm for the top curve. Wavelengths are indicated by the dots on the graph to the right. Quantum beats from the  $D^0X$  and the excited state (in bold) are  $\pi$ -out-of-phase from each other. *Right:* Nonlinear spectrum at zero delay between pump and probe. Resonances at  $D^0X$  and an excited state are visible at  $\lambda = 819.85$  nm and  $\lambda = 819.52$  nm respectively.

beats at these two wavelengths have the greatest amplitudes out of the series, and they are  $\pi$ -out-of phase from each other.

#### 5.4.4 Pump Intensity Dependency

The amplitude and phase of the quantum beats depends on the initialization of the  $D^0$  spin polarization, which is determined by the pulse area of the pump, as well as pump detuning from the  $D^0X$  absorption line center. In the following experiments the width of the pump pulse is fixed at 0.05 nm, red-detuned from the  $D^0X$  by approximately 0.1 nm and the pulse area is experimentally varied via the pump intensity,  $I_{pump}$ .

Referring to Fig 5.7, we observe that detection at either the  $D^0X$  or at the excited state produces similar results. The transient DT response is measured for a series of  $I_{pump}$  values. Initially increasing  $I_{pump}$  causes the quantum beat amplitude

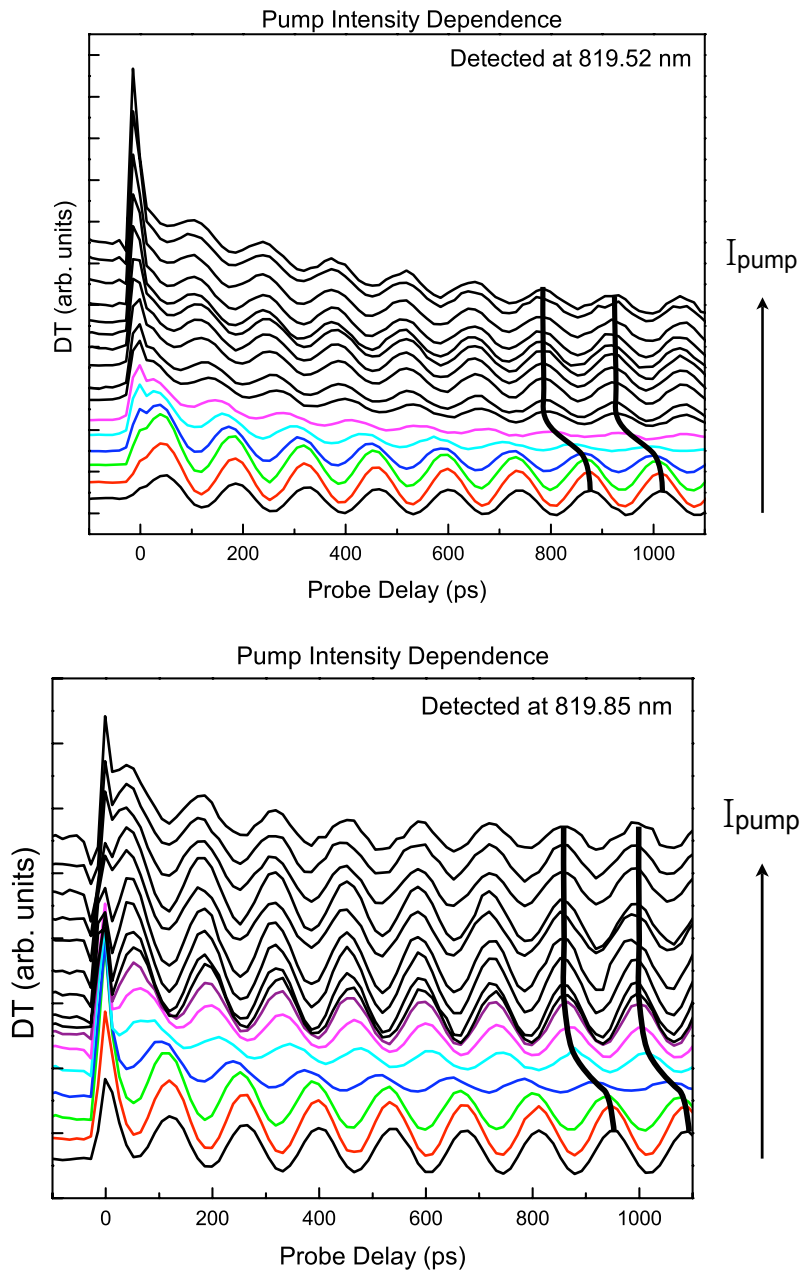


Figure 5.7: *Pump Intensity Dependence of QB Amplitudes.*  $I_{\text{pump}}$  studies at  $B = 1$  T and  $T = 2.3$  K. Curves from the bottom to top of each graph range from  $I_{\text{pump}} = 1.5$  to  $65$   $\text{mW}/\text{cm}^2$  in increments of approximately  $4$   $\text{mW}/\text{cm}^2$ . Heavy black lines serve to guide the reader's eye along the QB phase shift. *Top:* DT detection at the  $D^0X$  excited state nonlinear resonance,  $\lambda = 819.52$  nm. *Bottom:* DT detection at the  $D^0X$  nonlinear resonance,  $\lambda = 819.85$  nm.

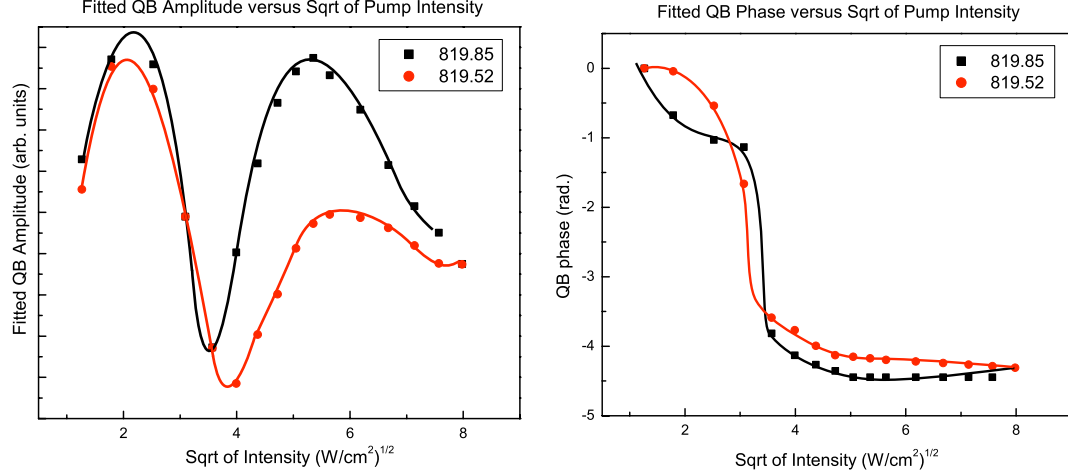


Figure 5.8: *Fitted QB Amplitude and Phase vs  $\sqrt{I_{pump}}$ .* QB amplitude and phase obtained by curve fitting the data in Fig. 5.7 using Eqn. 5.1, plotted against  $\sqrt{I_{pump}}$  for both detection wavelengths. Dots show fitted values for experiments and the curves serve to guide the reader's eye. *Left:* Fitted amplitude values. *Right:* Fitted phase values.

to amplify. But at 3 mW/cm<sup>2</sup> this effect saturates and the quantum beat amplitudes begin to diminish. At 15 mW/cm<sup>2</sup> the amplitudes begin to amplify again, and so on.

The quantum beat amplitudes were extracted from the data by fitting each curve with the following equation:

$$I_{QB_s} = Ae^{\gamma(t-t_o)} \cos(\omega_B + \omega_o)(t - t_o) + y \quad (5.1)$$

where A is the quantum beat amplitude,  $\omega_B$  is the Larmor frequency and correspondingly the quantum beat oscillation frequency,  $\gamma$ , is the  $D^0$  spin decoherence rate. The other variables  $t_o$ ,  $\omega_o$  and y take into account background and phase shifting. These fitted amplitudes as a function of  $\sqrt{I_{pump}}$  are shown in the left plot of Fig 5.8. We chose to plot the fitted amplitudes as a function of  $\sqrt{I_{pump}}$  in order to compare with calculated QB amplitudes in Fig. 5.9, which is

plotted against pulse area. Recall that pulse area,  $\theta(z)$  is defined as

$$\theta(z) = \int_{-\infty}^{\infty} dt \frac{\mu E(t, z)}{\hbar}, \quad (5.2)$$

where  $|E|^2 = I$ .

We also observe in Fig. 5.7 that as the quantum beat amplitude decreases with increasing  $I_{pump}$ , there is a corresponding phase shift of the quantum beats. The phase continues to shift with increasing  $I_{pump}$  until the phase is more than  $\pi$ -out-of-phase from the low-intensity signatures. Curve-fitting with Eqn, 5.1 has also yielded the phase of each of curve, and they are shown in the right plot of Fig. 5.8.

In order to understand the dependency of the quantum beat amplitude and phase on pump pulse area, we look to the optical Bloch equations describing an L-type three-level system for the  $D^0$  spin states and  $D^0X$  state, see Fig. 5.4. The L-type system is relevant because the pump duration time of 25 ps is an order of magnitude shorter than the  $B = 1.0$  T Larmor period of approximately 140 ps.

The amplitude of the quantum beats is given by the population inversion,  $w$ , between the two electron spin states, which is found by taking the difference between the diagonal density matrix elements,  $w = \rho_{++} - \rho_{--}$ . These matrix elements are coupled to the spin coherence matrix element,  $\rho_{+-}$ , which depends on the pump pulse area and detuning. An analytical solution for the inversion, calculated by Carey Phelps, gives an expression for the quantum beat amplitude, as a function of the pump pulse area. Fig. 5.9 shows the results for parameters matching experimental conditions in Fig. 5.7 including a pump red-detuned from the excitation resonance by 0.1 nm, with a width of 0.05 nm, and  $B = 1.0$  T.

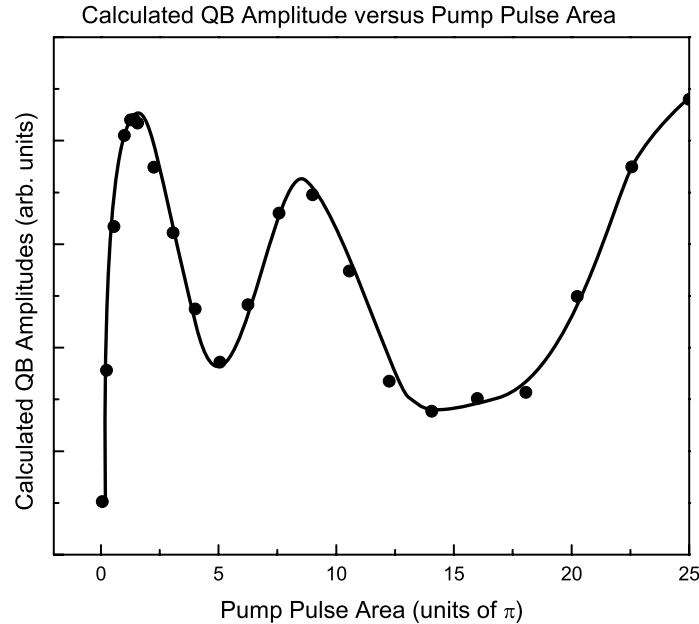


Figure 5.9: *Theoretical Pump Area Dependency of QB Amplitudes.* QB amplitude as function of the pump pulse area, calculated by Carey Phelps. Dots show calculated values and the black curve serves to guide the reader's eye. Calculation parameters were set to match experimental conditions, particularly the pump is was red-detuned from the resonance by 0.1 nm, with a width of 0.05 nm, and a splitting given by  $B = 1.0$  T.

Comparing Figs. 5.8 and 5.9, we see a qualitative agreement in the oscillation trend of the QB amplitude with increasing pump pulse area. By considering the L-type system, we can interpret the oscillations of the QB amplitude and phase with increasing  $I_{pump}$  as a competition between two spin polarization initialization mechanisms caused by the pump pulse. On the one hand, the pump causes transitions from the  $D^0 |1/2\rangle_z$  state to the  $D^0 X$  state. As more electrons make this transition, creating bound excitons, a greater net spin polarization in the  $-z$ -direction is initialized. The spin polarization is maximized when the  $D^0 |1/2\rangle_z$  is empty. This corresponds to quantum beats with a maximum amplitude. Likewise, when the intensity of the pump causes the electron to dipole transition up to the

$D^0X$  state and back down again, filling the  $D^0 |1/2\rangle_z$  state, there is no net spin polarization, and hence no quantum beats. This effect is equivalent to Rabi oscillations.

On the other hand, the pump pulse can also cause geometrical rotations of the spin polarization about the  $z$ -axis [32]. If the initial populations of  $D^0 |1/2\rangle_x$  and  $|-1/2\rangle_x$  are unbalanced, as is most likely the case in a realistic system [73], the initial net spin polarization will not be entirely be along the  $z$ -axis, and the pump will rotate the polarization around the  $z$ -axis by some angle,  $\theta$ , determined by the pump area. Projections of the rotated spin polarization onto the  $y - z$  axis correspond to initialized spin polarization, which then precess around the magnetic field according to  $\omega_B$ . These two effects combine to give us the quantum beat amplitude and phase dependencies we see experimentally in Figs. 5.7 and 5.8 and theoretically in 5.9.

## 5.5 Chapter Summary

This chapter presents experimental studies of electron spin coherence between donor-bound electron states coupled to donor-bound exciton states in a bulk GaAs free-standing sample. The spin coherence, i.e. polarization, induced is shown to be long-lived, on the order of 10 ns. Initialization of the polarization amplitude and phase is shown to be dependent on the pump intensity, or more generally, on the pump pulse area.

The homogeneity, and hence long lifetime of the  $D^0X$ , as well as the fact that it enables a  $\Lambda$ -type system for localized spins make it an attractive system for spin work. The next step for this work will be to fully rotate the spins with a  $\pi$ -pulse, in order to enable spin echo studies.

## CHAPTER VI

### CONCLUSIONS, FUTURE WORK, AND OUTLOOK

#### 6.1 Dissertation Summary

This dissertation presents experimental research on inducing, detecting, and manipulating electron spin coherence in semiconductor nanostructures. Electron spin coherence is an ideal system for exploring coherent quantum phenomena in semiconductors because its robust nature allows the coherence to endure over remarkably long time scales, compared to other coherences in semiconductors. The semiconductor nanostructures of interest in this dissertation all support  $\Lambda$ -type three level systems for conduction band electron spins.

In a GaAs/AlAs mixed type quantum well (MTQW) and a modulation-doped CdTe quantum well (QW), the upper level enabling a  $\Lambda$ -type system for electron spins is the ground state energy level of a trion, composed of two electrons of opposite spin and a hole. In these nanostructures, we successfully observe phenomena engendered by electron spin coherence via trions. Using differential transmission (DT) spectroscopy, we observe Coherent Zeeman Resonance (CZR), a precursor to Electromagnetically Induced Transparency (EIT), in the spectral domain, and we detect quantum beats due to electron spin coherence in the time domain. These studies permit investigation of the effects of manybody

interactions on the nonlinear optical response from electron spin coherence. It is the hope that a more complete understanding of the effects of manybody interactions will lead to new techniques for coherent optical control—either by allowing the manybody effects to be harnessed for the benefit of the experiment, or by allowing the manybody effects to be minimized in favor of allowing atomic-like behaviors in semiconductors to flourish.

Photoluminescence (PL) studies of the MTQW reveal trion formation by taking advantage of the unique MTQW band structure feature that allows control of the conduction band electron density through a process involving the optical injection of carriers. By optically controlling the electron density, we first study trion formation and observe the conversion of excitons into trions as well as temperature dependence of trion formation. We then use the MTQW's variable electron density to investigate the influence of manybody interactions on the induced nonlinear resonance from electron spin coherence, the CZR. Our results show that while the electron spin coherence induced via trions remains robust with increasing electron density, the nonlinear signal is suppressed because of the fragility of the relevant dipole coherences [41].

The MTQW studies reveal the persistent character of electron spin coherence enabled through trions, as well as the detrimental impact of manybody interactions on realizing EIT. We are thus motivated to continue our electron spin coherence studies in a sample known for its well-resolved, strong trion absorption resonance—a modulation-doped CdTe QW. In this sample, we observe CZR due to electron spin coherence via trions, corresponding to a 20% reduction in the sample absorption. This encouraging result warranted a time-domain investigation of electron spin coherence in the CdTe QW sample.

The transient study of electron spin coherence in the CdTe QW has two goals. First, we wish to investigate the spin coherence initialization process. Second, we hope to deepen our understanding of how manybody interactions affect the nonlinear optical response. Using a two-pulse pump-probe measurement technique, we learn that the spin coherence is initialized in the two-dimensional electron gas (2DEG) of the CdTe QW through trion formation. This initialization process is instigated either by resonant trion excitation or resonant exciton excitation. Despite the fact that the electron spin coherence can be indiscriminately initialized either by trion or exciton pumping, three-pulse DT studies reveals an interesting difference between injecting excitons or trions into the system using a third pulse called the control. We observe that the quantum beats detected at the exciton resonance can be qualitatively altered by injecting excitons at the appropriate times. However, injecting trions into the system does not significantly affect the nonlinear response [42]. We hope that these experimental results will stimulate further theoretical efforts in developing a microscopic description for coherent optical interactions in an interacting electron spin system in semiconductors.

The study of manybody effects is inherently interesting as a major unsolved problem in condensed matter physics. In our GaAs MTQW and CdTe QW experiments, we observe that manybody effects in semiconductors can, on the one hand, thwart attempts at coherent optical control. Specifically in this dissertation, the manybody effect interfere with the realization of full transparency in the EIT experiments, and prevent optical rotation of the spin polarization in the ultrafast experiments. On the other hand, the effects of manybody interactions can provide new avenues for coherent optical control, as is the case for the three-pulse CdTe QW experiments.

In order to study electron spin coherence in a system that does not experience manybody effects to the same degree as the GaAs MTQW and modulation-doped CdTe QW, we turn our research to a natural atomic-like zero-dimensional system, donor-bound electrons,  $D^0$ , in bulk GaAs. In the limit of a dilute donor concentration, interactions between donors are negligible, and we can therefore expect minimal interference from manybody interactions on nonlinear optical responses derived from electron spin coherence. To enable a  $\Lambda$ -type three level system for  $D^0$ , we use dipole coupling to a donor-bound exciton state,  $D^0X$ . We show spin coherence from  $D^0$  to be long-lived,  $\sim 10$  ns; this coherence time being limited by interactions with the surrounding nuclear spins of the GaAs crystal lattice. We also show pump intensity dependency studies of the nonlinear signal from the  $D^0$  spin coherence suggesting partial spin rotation induced by the pump.

## 6.2 Future Work and Outlook

A previously unmentioned motivation driving the study of electron spin coherence in semiconductors is the field of quantum information processing [51]. In classical computation, a unit of information is called a bit, taking the form of either a 0 or a 1. In quantum computation, the unit of information is a qubit. A qubit is a superposition state of two states  $|0\rangle$  and  $|1\rangle$ . That is,  $|\Psi_{qubit}\rangle = a|0\rangle + b|1\rangle$ , with the normalization condition  $|a|^2 + |b|^2 = 1$ . The power of quantum computation derives from the nature of superposition, so-called quantum parallelism. While a classical bit can only be in one state at a time, a qubit can simultaneously store two states; a classical n-bit system stores n states, while an n-qubit system can simultaneously store  $2^n$  states. Electron spin is a potential candidate for the qubit not only because of the discrete nature of electron spin as a two-level quantum

mechanical system, but also because induced coherence between electron spin states has proven to be exceptionally robust.

The homogeneity and long lifetime of the  $D^0X$  in bulk GaAs, as well as the fact that it enables a  $\Lambda$ -type system for localized spins, make it an extremely attractive system for electron spin coherence research. We observe the electron spin coherence of the  $D^0$  is notably long at  $\sim 10$  ns. However, this decoherence time, restricted by the hyperfine interactions between the electron spins and the surrounding nuclear spins, nevertheless limits the practicality of using the coherence for device applications or in quantum information processing. In quantum information processing, any operations performed on the the qubit would need to be accomplished on a timescale much faster than the decoherence time [78].

A long term goal of this research is to use dynamic decoupling (DD) to decouple the  $D^0$  spins from the surrounding GaAs nuclear spins. If DD is achieved, the electron spin decoherence time could theoretically be increased to the lifetime of the spins ( $\sim$ ms), improving the decoherence time by five orders of magnitude. The first step to achieving DD is to realize a  $\pi$ -pulse. Pulse sequence protocols resembling spin echo studies can then be employed to keep the coherence alive and therefore useable [70].

For the EIT experiments, an obvious immediate goal is to improve the degree of transparency induced in the semiconductor. One specific research direction is to pursue EIT experiments with the modulation-doped CdTe QW using pulsed lasers. In the transient regime, less manybody interactions should be induced than in the case of steady state excitation, and an improvement on the 20% absorption reduction can be attained. Another promising research direction is to use a semiconductor nanostructure fabricated in the waveguide geometry. In this

configuration, the longer optical path length will allow for stronger interactions, allowing for enhanced quantum interference effects.

Of course, the main challenge in pursuing EIT or any coherent phenomena using electron spin coherence in semiconductors is coping with the manybody effects intrinsic in an interacting spin system. Two perspectives can be taken in confronting the issue. We can attempt to limit the manybody interactions and their effects, thereby constraining the semiconductor system to behave like an atomic system. One way to accomplish this goal is by sidestepping the issue altogether by finding a suitable system which inherently has less manybody interactions, such as  $D^0$  in bulk GaAs or electron spins in single quantum dots. Conversely, if we cannot limit the effects of manybody interactions, we need to devise a clever scheme to exploit them for the benefit of the experiment. For example, perhaps future work will find an application harnessing the manybody effects induced by exciton injection in modulation-doped CdTe QWs.

This dissertation presents work that contributes to understanding the initialization, detection, and initialization of electron spin coherence in semiconductor nanostructures, as well as how the effects of manybody interactions can influence the nonlinear optical response from electron spin coherence. It is the hope that the continuation of this research will lead to breakthroughs allowing for solid-state implementation of quantum coherence phenomena involving electron spins such as EIT and perhaps even quantum information processing.

## CHAPTER A

## DENSITY MATRIX CALCULATION FOR THE SPECTRAL DOMAIN

## 1.1 Introduction to the Density Matrix Approach

This appendix details the calculation of the density matrix elements for a  $\Lambda$ -type three-level system interacting with two continuous-wave electric fields in the steady state using an order by order perturbation method. The density matrix elements can then be used to find the polarization induced in the material by the fields. The final goal of the calculation is to find the induced nonlinear optical signal, which is proportional to the imaginary part of the polarization by the Maxwell-Bloch equations.

We will examine the three-level,  $\Lambda$ -configuration system interacting with a pump field,  $E_1$ , and a probe field,  $E_2$ , with frequencies  $\nu_1$  and  $\nu_2$  and directions  $k_1$  and  $k_2$  respectively. Transitions between  $|a\rangle$  and  $|c\rangle$  and between  $|b\rangle$  and  $|c\rangle$  are allowed, but the transition between  $|a\rangle$  and  $|b\rangle$  is dipole forbidden. Both fields couple to both transitions. The frequency difference between levels  $|a\rangle$  and  $|c\rangle$  is  $\omega_{ac}$  and the dipole coupling between these two levels is  $\mu_a$ . The other transition is labeled similarly. Please refer to Figure 1.1.

We write the total Hamiltonian as the sum of the time-independent unperturbed Hamiltonian of the atom plus the perturbation introduced by the two

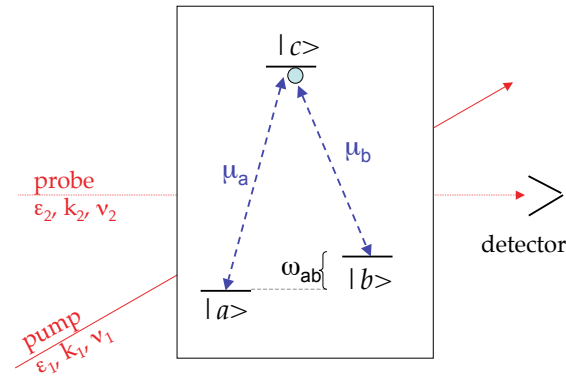


Figure 1.1: Transitions  $|a\rangle$  to  $|c\rangle$  and  $|b\rangle$  to  $|c\rangle$  are allowed. However, the transition between  $|a\rangle$  and  $|b\rangle$  is dipole forbidden. Both fields couple to both transitions.

fields interacting with the atom.

$$H = H_o + V \quad (1.1)$$

The Hamiltonian of the unperturbed atom, in the basis of its eigenstates, is given by the following matrix:

$$H_o = \hbar \begin{bmatrix} \omega_a & 0 & 0 \\ 0 & \omega_b & 0 \\ 0 & 0 & \omega_c \end{bmatrix} \quad (1.2)$$

The interaction potential is given by  $V = -\bar{\mu} \cdot \bar{E}$ . We use the dipole approximation, valid when the wavelengths of the fields are much greater than the Bohr radius ( $\lambda_{1,2} \gg r_B$ ). In this approximation, we write the dipole moment as  $\bar{\mu} = e\bar{r}$ . We see that the diagonal elements of  $\bar{\mu}$  are zero due to parity. The total electric field is written as a linear combination of the pump and probe fields,  $\bar{E} = \epsilon_1 e^{i\bar{k}_1 \bar{r}} \cos \nu_1 t + \epsilon_2 e^{i\bar{k}_2 \bar{r}} \cos \nu_2 t$ , where  $k_{1,2}$  refer to the directions of the pump and probe fields and  $\epsilon_{1,2}$  refers to their respective amplitudes. To simplify the notation, we define the Rabi frequencies (including direction) to refer to the electric fields,  $\Omega_{n_i} = \frac{\mu_i \epsilon_n}{\hbar} e^{i\bar{k}_n \bar{r}}$ . The index  $n = 1, 2$  refers to the pump or probe, and the index  $i = a, b$  refers to dipole transition  $\mu_a$  or  $\mu_b$ . And so the interaction Hamiltonian,  $V$ , is given by the following matrix:

$$-\hbar \begin{bmatrix} 0 & 0 & \Omega_{1_a} \cos \nu_1 t + \Omega_{2_a} \cos \nu_2 t \\ 0 & 0 & \Omega_{1_b} \cos \nu_1 t + \Omega_{2_b} \cos \nu_2 t \\ \Omega_{1_a}^* \cos \nu_1 t + \Omega_{2_a}^* \cos \nu_2 t & \Omega_{1_b}^* \cos \nu_1 t + \Omega_{2_b}^* \cos \nu_2 t & 0 \end{bmatrix}$$

## 1.2 The Density Matrix Equations of Motion

We can now use the Liouville equation of motion for the density matrix:

$$\dot{\rho} = \frac{1}{i\hbar} [H, \rho] \quad (1.3)$$

We solve this equation for each density matrix element, and then phenomenologically add decay terms. As an example, we will solve the  $\dot{\rho}_{aa}$  equation

step-by-step:

$$\begin{aligned}
\dot{\rho}_{aa} &= \frac{1}{i\hbar} \langle a | [H, \rho] | a \rangle = \frac{1}{i\hbar} \langle a | [H_o + V, \rho] | a \rangle \\
&= \frac{1}{i\hbar} (\langle a | [H_o, \rho] | a \rangle + \langle a | [V, \rho] | a \rangle) \\
&= \frac{1}{i\hbar} (\langle a | H_o \rho | a \rangle - \langle a | \rho H_o | a \rangle + \langle a | V \rho | a \rangle - \langle a | \rho V | a \rangle) \quad (1.4)
\end{aligned}$$

We now insert complete sets  $\sum_{i=a,b,c} |i\rangle \langle i|$  into the last two brackets of equation 1.4.

Referring to the interaction Hamiltonian,  $V$ , we keep only non-zero terms:

$$\begin{aligned}
\dot{\rho}_{aa} &= \frac{1}{i\hbar} (\cancel{\hbar\omega_a \rho_{aa}} - \cancel{\rho_{aa} \hbar\omega_a} + \langle a | V | c \rangle \langle c | \rho | a \rangle - \langle a | \rho | c \rangle \langle c | V | a \rangle) \\
&= \frac{1}{i\hbar} (V_{ac} \rho_{ac} - \rho_{ac} V_{ca}) \\
&= i(\Omega_{1_a} \cos \nu_1 t + \Omega_{2_a} \cos \nu_2 t) \rho_{ca} + c.c. \\
&= -\Gamma_a \rho_{aa} + \{i(\Omega_{1_a} \cos \nu_1 t + \Omega_{2_a} \cos \nu_2 t) \rho_{ca} + c.c.\} \quad (1.5)
\end{aligned}$$

In equation 1.5 the population relaxation term  $\Gamma_a \rho_{aa}$  is phenomenologically added in. Following similar procedures for each of the density matrix elements, we

obtain the following equations of motion:

$$\dot{\rho}_{aa} = -\Gamma_a \rho_{aa} + \{i(\Omega_{1_a} \cos \nu_1 t + \Omega_{2_a} \cos \nu_2 t) \rho_{ca} + c.c.\} \quad (1.6)$$

$$\dot{\rho}_{bb} = -\Gamma_b \rho_{bb} + \{i(\Omega_{1_b} \cos \nu_1 t + \Omega_{2_b} \cos \nu_2 t) \rho_{cb} + c.c.\} \quad (1.7)$$

$$\begin{aligned} \dot{\rho}_{ab} = & - (i\omega_{ab} + \gamma_{ab}) \rho_{ab} + i(\Omega_{1_a} \cos \nu_1 t + \Omega_{2_a} \cos \nu_2 t) \rho_{cb} \\ & - i(\Omega_{1_b}^* \cos \nu_1 t + \Omega_{2_b}^* \cos \nu_2 t) \rho_{ac} \end{aligned} \quad (1.8)$$

$$\begin{aligned} \dot{\rho}_{ac} = & - (i\omega_{ac} + \gamma_a) \rho_{ac} + i(\Omega_{1_a} \cos \nu_1 t + \Omega_{2_a} \cos \nu_2 t) (\rho_{cc} - \rho_{aa}) \\ & - i(\Omega_{1_b} \cos \nu_1 t + \Omega_{2_b} \cos \nu_2 t) \rho_{ab} \end{aligned} \quad (1.9)$$

$$\begin{aligned} \dot{\rho}_{bc} = & - (i\omega_{bc} + \gamma_b) \rho_{bc} + i(\Omega_{1_b} \cos \nu_1 t + \Omega_{2_b} \cos \nu_2 t) (\rho_{cc} - \rho_{bb}) \\ & - i(\Omega_{1_a} \cos \nu_1 t + \Omega_{2_a} \cos \nu_2 t) \rho_{ba} \end{aligned} \quad (1.10)$$

The terms  $\gamma_a$  and  $\gamma_b$  describe the dephasing of the dipole coherences, whereas  $\gamma_{ab}$  describes the dephasing of the Raman coherence between states  $|a\rangle$  and  $|b\rangle$ .

### 1.3 The Order by Order Calculation

It is now our task to solve the differential equations 1.6-1.10. To accomplish this, we do an iterative substitution order by order.

#### 1.3.1 Zeroth Order

For the Zeroth Order, we must assume some initial conditions. We will let the system be in the excited state  $|c\rangle$  initially. We will also assume the system is initially unpolarized. These assumptions can be written as follows:

$$\begin{array}{lll} \rho_{aa}^{(0)} = 0 & \rho_{bb}^{(0)} = 0 & \rho_{cc}^{(0)} = 1 \\ \rho_{ab}^{(0)} = 0 & \rho_{ac}^{(0)} = 0 & \rho_{bc}^{(0)} = 0 \end{array}$$

Each total matrix element is equal to the sum of its orders. For example,

$$\rho_{aa} = \rho_{aa}^{(0)} + \rho_{aa}^{(1)} + \rho_{aa}^{(2)} + \dots$$

Because the total population is unity,  $\rho_{aa} + \rho_{bb} + \rho_{cc} = 1$ , and we can see that  $\rho_{aa}^{(0)} + \rho_{bb}^{(0)} + \rho_{cc}^{(0)} = 1$ , we know that the sum of the diagonal matrix elements in each subsequent order must equal zero. That is,  $\rho_{aa}^{(n>0)} + \rho_{bb}^{(n>0)} + \rho_{cc}^{(n>0)} = 0$ .

### 1.3.2 First Order

In the first order, we can immediately see that the diagonal elements are zero. Because  $\rho_{ac}^{(0)} = 0$  and  $\rho_{bc}^{(0)} = 0$ , equations 1.6 and 1.7 have no source terms. Therefore  $\rho_{aa}^{(1)} = 0$  and  $\rho_{bb}^{(1)} = 0$ . We know that  $\rho_{cc}^{(1)} = 0$  because the sum of the three diagonal elements must be zero. We can also see that  $\rho_{ab}^{(1)} = 0$  because equation 1.8 also has no source term in the first order. It now remains to find  $\rho_{ac}^{(1)}$  and  $\rho_{bc}^{(1)}$ .

We use equation 1.9 to write the the differential equation for  $\dot{\rho}_{ac}^{(1)}$  in the rotating wave approximation:

$$\begin{aligned}
\dot{\rho}_{ac}^{(1)} &= - (i\omega_{ac} + \gamma_a)\rho_{ac}^{(1)} + \frac{i}{2}(\Omega_{1a}e^{-i\nu_1 t} + \Omega_{2a}e^{-i\nu_2 t})(\rho_{cc}^{(0)} - \rho_{aa}^{(0)}) \\
&\quad - i(\Omega_{1b}e^{-i\nu_1 t} + \Omega_{2b}e^{-i\nu_2 t})\rho_{ab}^{(0)} \\
&= - (i\omega_{ac} + \gamma_a)\rho_{ac}^{(1)} + \frac{i}{2}(\Omega_{1a}e^{-i\nu_1 t} + \Omega_{2a}e^{-i\nu_2 t})
\end{aligned} \tag{1.11}$$

The rotating wave approximation allows us to disregard the off-resonant parts of the fields. In this case, we canceled the  $e^{i\nu_1 t}$  and  $e^{i\nu_2 t}$  terms from the cosines in equation 1.9.

To solve the differential equation 1.11, we define  $\rho_{ac}^{(1)}$  in terms of two rotating frames.

$$\rho_{ac}^{(1)} = \tilde{\rho}_{ac_1}^{(1)}e^{-i\nu_1 t} + \tilde{\rho}_{ac_2}^{(1)}e^{-i\nu_2 t} \tag{1.12}$$

We take a derivative of equation 1.12 and substitute the derivative and equation 1.12 itself into equation 1.11. To solve for the steady state, we set  $\dot{\tilde{\rho}}_{ac_{1,2}} = 0$ . We then get expressions for  $\tilde{\rho}_{ac_1}^{(1)}$  and  $\tilde{\rho}_{ac_2}^{(1)}$ . Inserting these expressions into equation 1.12, we get the following solution for  $\rho_{ac}^{(1)}$ :

$$\rho_{ac}^{(1)} = \frac{\frac{i}{2}\Omega_{1a}}{\gamma_a + i\Delta_{1a}}e^{-i\nu_1 t} + \frac{\frac{i}{2}\Omega_{2a}}{\gamma_a + i\Delta_{2a}}e^{-i\nu_2 t} \tag{1.13}$$

To simply notation, we have made the following definitions for the detunings:

$$\begin{aligned}
\Delta_{1a} &= \omega_{ac} - \nu_1 & \Delta_{2a} &= \omega_{ac} - \nu_2 \\
\Delta_{1b} &= \omega_{bc} - \nu_1 & \Delta_{2b} &= \omega_{bc} - \nu_2
\end{aligned}$$

We repeat this procedure starting with equation 1.10. After make the rotating wave

approximation, defining  $\rho_{bc}^{(1)}$  in terms of two rotating frames, and making similar substitutions to those above, we obtain the following expression for  $\rho_{bc}^{(1)}$  in the steady state:

$$\rho_{bc}^{(1)} = \frac{\frac{i}{2}\Omega_{1b}}{\Gamma_{bc} + i\Delta_{1b}} e^{-i\nu_1 t} + \frac{\frac{i}{2}\Omega_{2b}}{\Gamma_{bc} + i\Delta_{2b}} e^{-i\nu_2 t} \quad (1.14)$$

We note here that the above expression for  $\rho_{bc}^{(1)}$  can be obtained from  $\rho_{ac}^{(1)}$  (and vice versa) simply by replacing  $a \leftrightarrow b$ .

### 1.3.3 Second Order

In the second order to the applied electric fields, the dipole transition matrix elements,  $\rho_{ac}^{(2)}$  and  $\rho_{bc}^{(2)}$ , are zero, whereas the population matrix elements and the Raman spin coherence term have values.

Examining equation 1.8, we write it in the second order, using the rotating wave approximation:

$$\begin{aligned} \dot{\rho}_{ab}^{(2)} = & -(i\omega_{ab} + \gamma_{ab})\rho_{ab}^{(2)} + \frac{i}{2}(\Omega_{1a}e^{-i\nu_1 t} + \Omega_{2a}e^{-i\nu_2 t})\rho_{cb}^{(1)} \\ & - \frac{i}{2}(\Omega_{1b}^*e^{i\nu_1 t} + \Omega_{2b}^*e^{i\nu_2 t})\rho_{ac}^{(1)} \end{aligned} \quad (1.15)$$

Recall that  $\rho_{bc}^{*(1)} = \rho_{cb}^{(1)}$ , and insert the first order results for  $\rho_{cb}^{(1)}$  and  $\rho_{ac}^{(1)}$  (equations 1.13 and 1.14) into equation 1.15. We then write  $\rho_{ac}^{(2)}$  in terms of two rotating terms, and one D.C. term as follows:

$$\rho_{ab}^{(2)} = \tilde{\rho}_{ab_1}^{(2)} e^{i\delta t} + \tilde{\rho}_{ab_2}^{(2)} e^{-i\delta t} + \tilde{\rho}_{ab_3}^{(2)} \quad (1.16)$$

We have defined a new variable as the detuning between the two fields,  $\delta = \nu_1 - \nu_2$ . We put equation 1.16 and its derivative back into 1.15, and then solve for the steady state—that is, we set  $\dot{\tilde{\rho}}_{ab_{1,2,3}}^{(2)} = 0$ . Our results are expressions for  $\tilde{\rho}_{ab_1}^{(2)}$ ,

$\tilde{\rho}_{ab_2}^{(2)}$ , and  $\tilde{\rho}_{ab_3}^{(2)}$ . These expressions are plugged back into equation 1.16 and we obtain the following result:

$$\begin{aligned}
\rho_{ab}^{(2)} = & \underbrace{\frac{\frac{1}{4}\Omega_{1_b}^*\Omega_{2_a}}{i(\omega_{ab} + \delta) + \gamma_{ab}} \left( \frac{1}{\gamma_b - i\Delta_{1b}} + \frac{1}{\gamma_a + i\Delta_{2a}} \right)}_{\text{coherent}} e^{i\delta t} \\
& + \underbrace{\frac{\frac{1}{4}\Omega_{1_a}\Omega_{2_b}^*}{i(\omega_{ab} - \delta) + \gamma_{ab}} \left( \frac{1}{\gamma_b - i\Delta_{2b}} + \frac{1}{\gamma_a + i\Delta_{1a}} \right)}_{\text{coherent}} e^{-i\delta t} \\
& + \underbrace{\frac{\frac{1}{4}\Omega_{1_a}\Omega_{1_b}^*}{i\omega_{ab} + \gamma_{ab}} \left( \frac{1}{\gamma_b - i\Delta_{1b}} + \frac{1}{\gamma_a + i\Delta_{1a}} \right)}_{\text{incoherent}} + \underbrace{\frac{\frac{1}{4}\Omega_{2_a}\Omega_{2_b}^*}{i\omega_{ab} + \gamma_{ab}} \left( \frac{1}{\gamma_b - i\Delta_{2b}} + \frac{1}{\gamma_a + i\Delta_{2a}} \right)}_{\text{incoherent}}
\end{aligned} \tag{1.17}$$

Consider the nature of each of the four terms in the expression above. By looking at the subscripts of the Rabi frequency prefactors, we see that the first and second terms in the expression (which are identical when you interchange indices 1 and 2) describe the coherent interaction of the two fields in the sample. We can see that these coherent terms oscillate according to  $e^{-i\delta t}$ , at the detuning frequency,  $\delta$ . The third and fourth terms are the incoherent, or so-called ‘‘D.C.’’ contributions. These terms are each due to one field acting twice on the sample, and result in a saturation of the transition. Only the first and third terms ultimately contribute to the DT signal because we will ignore all final terms that are not in the direction of the probe. The first term leads to the Coherent Zeeman Resonance peaks when sensed by the pump in the third order. The third term will contribute to our final signal by adding a pedestal effect, when sensed by the probe in the third order.

We can calculate the second order population terms in the same way, obtaining the following results:

$$\begin{aligned}
\rho_{aa}^{(2)} &= \frac{\frac{1}{4}\Omega_{1a}^*\Omega_{2a}}{\Gamma_a + i\delta} \left( \frac{1}{\gamma_a + i\Delta_{2a}} + \frac{1}{\gamma_a - i\Delta_{1a}} \right) e^{i\delta t} \\
&+ \frac{\frac{1}{4}\Omega_{1a}\Omega_{2a}^*}{\Gamma_a - i\delta} \left( \frac{1}{\gamma_a + i\Delta_{1a}} + \frac{1}{\gamma_a - i\Delta_{2a}} \right) e^{-i\delta t} \\
&+ \frac{|\Omega_{1a}|^2}{4\Gamma_a} \left( \frac{1}{\gamma_a + i\Delta_{1a}} + \frac{1}{\gamma_a - i\Delta_{1a}} \right) + \frac{|\Omega_{2a}|^2}{4\Gamma_a} \left( \frac{1}{\gamma_a + i\Delta_{2a}} + \frac{1}{\gamma_a - i\Delta_{2a}} \right)
\end{aligned} \tag{1.18}$$

$$\begin{aligned}
\rho_{bb}^{(2)} &= \frac{\frac{1}{4}\Omega_{1b}^*\Omega_{2b}}{\Gamma_b + i\delta} \left( \frac{1}{\gamma_b + i\Delta_{2b}} + \frac{1}{\gamma_b - i\Delta_{1b}} \right) e^{i\delta t} \\
&+ \frac{\frac{1}{4}\Omega_{1b}\Omega_{2b}^*}{\Gamma_b - i\delta} \left( \frac{1}{\gamma_b + i\Delta_{1b}} + \frac{1}{\gamma_b - i\Delta_{2b}} \right) e^{-i\delta t} \\
&+ \frac{|\Omega_{1b}|^2}{4\Gamma_b} \left( \frac{1}{\gamma_b + i\Delta_{1b}} + \frac{1}{\gamma_b - i\Delta_{1b}} \right) + \frac{|\Omega_{2b}|^2}{4\Gamma_b} \left( \frac{1}{\gamma_b + i\Delta_{2b}} + \frac{1}{\gamma_b - i\Delta_{2b}} \right)
\end{aligned} \tag{1.19}$$

Again we can see that the first two terms in the above expressions describe coherent interactions of the two fields, whereas the second two terms in each expression describe incoherent or D.C. contributions.

#### 1.3.4 Third Order

We have now reached the point at which we can calculate the desired expressions for the third order dipole coherences. Because we are only interested in the terms which propagate along the probe direction,  $\bar{k}_2$ , the line on which our detector is placed, we will only keep terms which contain  $\Omega_2|\Omega_1|^2$ . Further, in the interest of keeping track of the origin of each of the final terms contributing to the DT signal, we will treat contributions from population and spin separately. That is, contributions from the second order population terms  $\rho_{aa}^{(2)}$  and  $\rho_{bb}^{(2)}$  (Eqns. 1.18 and 1.19) will yield  $\rho_{bc_{pop}}^{(3)}$  and  $\rho_{ac_{pop}}^{(3)}$ , and contributions from the second order spin

coherence term  $\rho_{ab}^{(2)}$  (Eqn. 1.17) will yield  $\rho_{bc\text{spin}}^{(3)}$  and  $\rho_{bc\text{spin}}^{(3)}$ .

Referring to equation 1.10, we can write down the third order equation of motion for  $\dot{\rho}_{bc}$ , again applying the rotating wave approximation:

$$\begin{aligned} \dot{\rho}_{bc}^{(3)} = & -(i\omega_{bc} + \gamma_b)\rho_{bc}^{(3)} + \frac{i}{2}(\Omega_{1b}e^{-i\nu_1t} + \Omega_{2b}e^{-i\nu_2t})(\rho_{cc}^{(2)} - \rho_{aa}^{(2)}) \\ & - \frac{i}{2}(\Omega_{1a}e^{-i\nu_1t} + \Omega_{2a}e^{-i\nu_2t})\rho_{ba}^{(2)} \end{aligned} \quad (1.20)$$

By first only considering the spin contribution and ignoring the population contribution, we calculate  $\rho_{ba}^{(2)}$  by taking the complex conjugate of equation 1.17, and then we substitute into the third order equation above. We keep only terms proportional to  $\Omega_2|\Omega_1|^2$ . We then write  $\rho_{bc}^{(3)}$  in a rotating frame as follows:

$$\rho_{bc}^{(3)} = \tilde{\rho}_{bc}^{(3)} e^{-i\nu_2t} \quad (1.21)$$

As in the previous two orders, we substitute equation 1.21 and its derivative back into equation 1.20, and we solve for the steady state solution, by setting  $\dot{\tilde{\rho}}_{bc}^{(3)} = 0$ . After algebraic simplification, we obtain the following expression for  $\rho_{bc\text{spin}}^{(3)}$ :

$$\begin{aligned} \rho_{bc\text{spin}}^{(3)} = & \frac{\frac{1}{8}|\Omega_1|^2\Omega_2\mu_a^2\mu_b e^{-i\nu_2t}}{\Delta_{2b} - i\gamma_b} \left[ \frac{1}{(\omega_{ab} - \delta) + i\gamma_{ab}} \underbrace{\left( \frac{1}{i\gamma_a + \Delta_{1a}} + \frac{1}{i\gamma_b - \Delta_{2b}} \right)}_{\text{spin.coh}} \right. \\ & \left. - \frac{1}{\gamma_{ab} - i\omega_{ab}} \underbrace{\left( \frac{1}{\gamma_a - i\Delta_{1a}} + \frac{1}{\gamma_b + i\Delta_{1b}} \right)}_{\text{spin.DC}} \right] \end{aligned} \quad (1.22)$$

By tracking the origin of each term and where the detuning,  $\delta$ , plays a role, we can see that the first term in the expression is from coherent interactions and the second

term is from incoherent interactions of single fields.

Going back to Eqn. 1.20, we now consider the population contributions and similarly obtain an expression for  $\rho_{bc_{pop}}^{(3)}$ :

$$\begin{aligned} \rho_{bc_{pop}}^{(3)} = \frac{-i|\Omega_1|^2\Omega_2\mu_a^2\mu_b e^{-i\nu_2 t}}{i\Delta_{2b} + \gamma_b} & \left[ \frac{1}{\Gamma_a + i\delta} \underbrace{\left( \frac{1}{\gamma_a - i\Delta_{1a}} + \frac{1}{\gamma_a + \Delta_{2a}} \right)}_{pop.coh_1} \right. \\ & + \frac{1}{\Gamma_a} \underbrace{\left( \frac{1}{\gamma_a - i\Delta_{1a}} + \frac{1}{\gamma_a + i\Delta_{1a}} \right)}_{pop.DC_1} \\ & + \frac{2}{\Gamma_b + i\delta} \underbrace{\left( \frac{1}{\gamma_b - i\Delta_{1b}} + \frac{1}{\gamma_b + \Delta_{2b}} \right)}_{pop.coh_2} \\ & \left. + \frac{2}{\Gamma_b} \underbrace{\left( \frac{1}{\gamma_b - i\Delta_{1b}} + \frac{1}{\gamma_b + i\Delta_{1b}} \right)}_{pop.DC_2} \right] \end{aligned} \quad (1.23)$$

The total dipole coherence term in the third order,  $\rho_{bc}^{(3)}$  is given by the sum of Eqn. 1.23 and Eqn. 1.22, and thus has six total terms which we have identified as follows:

$$\begin{aligned} \rho_{bc}^{(3)} = & spin.coh + spin.DC \\ & + pop.coh_1 + pop.DC_1 + pop.coh_2 + pop.DC_2 \end{aligned}$$

Six similar terms comprise  $\rho_{ac}^{(3)}$ , which we can easily find by replacing  $a \leftrightarrow b$  in the  $\rho_{bc}^{(3)}$  expression.

#### 1.4 The Nonlinear Signal

To find the DT signal, we first need to calculate the third order polarization induced in the sample by the two fields. The polarization is found by taking the trace of the third order density matrix with the dipole interaction matrix, which reduces as follows:

$$\begin{aligned}
 P^{(3)} &= Tr[\mu\rho^{(3)}] \\
 &= \sum_k \sum_i \langle k | \mu | i \rangle \langle i | \rho^{(3)} | k \rangle \\
 &= \mu_a \rho_{ac}^{(3)} + \mu_b \rho_{bc}^{(3)} + c.c.
 \end{aligned}$$

The polarization-induced electric field,  $E^{(3)}$  can be found in the far-field limit by the relationship  $E^{(3)} \propto iP^{(3)}$ , which derives from the Maxwell-Bloch equations and implies a  $\pi/2$  phase shift between the polarization and emitted field.

The DT signal is the modulus squared of the sum of the probe,  $E_2$  written in complex form, and emitted field,  $E^{(3)}$ :

$$\begin{aligned}
 DT &\sim |E_2 + E^{(3)}|^2 \\
 &\sim |E_2 + iP^{(3)}|^2 \\
 &\sim |E_2|^2 + |E_p|^2 - 2E_2P^{(3)}
 \end{aligned}$$

The first term is neglected due to the detection technique. We use a lockin to detect signals at the modulation frequency of the chopped pump. The second term is ignored because it is of negligible amplitude. So, we are left with the relationship:

$$DT \propto [\rho_{bc}^{(3)} + \rho_{ac}^{(3)} + c.c.] \quad (1.24)$$

Eqn. 1.24 has terms of four different types: coherent spin terms, D.C. spin terms, coherent population terms and D.C. spin terms. Each type of term contributes a different effect to the overall DT signal. Each contribution is plotted below in Fig. 1.2.

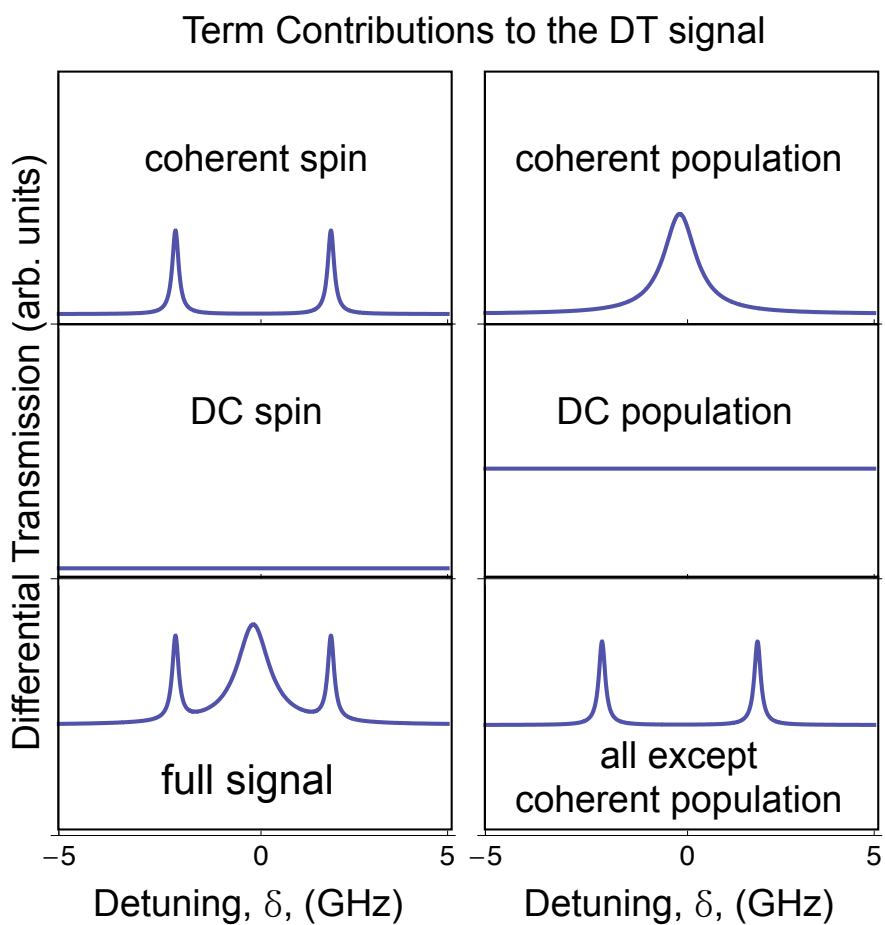


Figure 1.2: Contributions from each of the four types of terms are plotted separately. The bottom graphs show the full signal with and without population coherence. The full signal is obtained by co-circularly polarized light, and the signal without the coherent population terms is obtained with cross-linearly polarized light.

## BIBLIOGRAPHY

- [1] L. Bányai, Q. T. Vu, B. Mieck, and H. Haug, *Phys. Rev. Lett.* **81**, 882 (1998).
- [2] V. Langer, H. Stolz, and W. von der Osten, *Phys. Rev. Lett.* **64**, 854 (1990).
- [3] R. Binder and M. Lindberg, *Phys. Rev. Lett.* **81**, 1477 (1998).
- [4] S. E. Harris, *Physics Today* **50**, 36 (1997).
- [5] M. O. Scully and M. S. Zubairy, *Quantum Optics* (Cambridge Univ. Press, Cambridge, 1997).
- [6] D. Budker, D. F. Kimball, S. M. Rochester, and V. V. Yashchuk, *Phys. Rev. Lett.* **83**, 1767 (1999).
- [7] C. Liu, Z. Dutton, C. H. Behroozi, and L. V. Hau, *Nature* **409**, 490 (2001).
- [8] M. T. L. Hsu, G. Hetet, O. Glockl, J. J. Longdell, B. C. Buchler, H.-A. Bachor, and P. K. Lam, *Phys. Rev. Lett.* **97**, 183601 (2006).
- [9] G. Hetet, A. Peng, M. T. Johnsson, J. J. Hope, and P. K. Lam, *Phys. Rev. A* **77**, 012323 (2008).
- [10] M. Phillips and H. Wang, *Phys. Rev. Lett.* **89**, 186401 (2002).
- [11] M. Phillips and H. Wang, *Phys. Rev. Lett.* **91**, 183602 (2002).
- [12] S. Marcinkevicius, A. Gushterov, and J. P. Reithmaier, *Appl. Phys. Lett.* **92**, 041113 (2008).
- [13] A. V. Khaetskii, D. Loss, and L. Glazman, *Phys. Rev. Lett.* **88**, 186802 (2002).
- [14] I. A. Merkulov, A. L. Efros, and M. Rosen, *Phys. Rev. B* **65**, 205309 (2002).
- [15] A. P. Heberle, W. W. Rühle, and K. Ploog, *Phys. Rev. Lett.* **72**, 3887 (1994).
- [16] J. M. Kikkawa and D. D. Awschalom, *Phys. Rev. Lett.* **80**, 4313 (1998).
- [17] F. Meier and Zakharchenya, eds., *Optical Orientation* (North-Holland, Amsterdam, 1984).
- [18] L. J. Sham, *J. of Phys.: Cond. Matt.* **5**, A51 (1993).

- [19] P.-F. Braun, X. Marie, L. Lombez, B. Urbaszek, T. Amand, P. Renucci, V. K. Kalevich, K. V. Kavokin, O. Krebs, P. Voisin, et al., *Phys. Rev. Lett.* **94**, 116601 (2005).
- [20] A. Greilich, D. R. Yakovlev, A. Shabaev, A. L. Efros, I. A. Yugova, R. Oulton, V. Stavarache, D. Reuter, A. Wieck, and M. Bayer, *Science* **313**, 341 (2006).
- [21] R. Oulton, A. Greilich, S. Y. Verbin, R. V. Cherbunin, T. Auer, D. R. Yakovlev, M. Bayer, I. A. Merkulov, V. Stavarache, D. Reuter, et al., *Physical Review Letters* **98**, 107401 (2007).
- [22] D. D. Awschalom and J. M. Kikkawa, *Physics Today* **52**, 33 (1999).
- [23] S. A. Wolf, D. D. Awschalom, R. A. Buhrman, J. M. Daughton, S. von Molnár, M. L. Roukes, A. Y. Chtchelkanova, and D. M. Treger, *Science* **294**, 1488 (2001).
- [24] S. A. Crooker, D. D. Awschalom, J. J. Baumberg, F. Flack, and N. Samarth, *Phys. Rev. B* **56**, 7574 (1997).
- [25] P. Palinginis and H. Wang, *Phys. Rev. Lett.* **92**, 037402 (2004).
- [26] P. Palinginis and H. Wang, *Phys. Rev. B* **70**, 153307 (2004).
- [27] W. Yao, R.-B. Liu, and L. J. Sham, *Phys. Rev. Lett.* **95**, 030504 (2005).
- [28] L. M. Duan, M. D. Lukin, J. I. Cirac, and P. Zoller, *Nature* **414**, 413 (2001).
- [29] K.-M. C. Fu, C. Santori, C. Stanley, M. C. Holland, and Y. Yamamoto, *Phys. Rev. Lett.* **95**, 187405 (2005).
- [30] C. Santori, D. Fattal, S. M. Spillane, M. Fiorentino, R. G. Beausoleil, A. D. Greentree, P. Olivero, M. Draganski, J. R. Rabeau, P. Reichart, et al., *Optics Express* **17**, 7986 (2006).
- [31] T. A. Kennedy, A. Shabaev, M. Scheibner, A. L. Efros, A. S. Bracker, and D. Gammon, *Phys. Rev. B* **73**, 045307 (2006).
- [32] S. E. Economou, L. J. Sham, Y. Wu, and D. G. Steel, *Phys. Rev. B* **74**, 205415 (2006).
- [33] Z. Chen, R. Bratschitsch, S. G. Carter, S. T. Cundiff, D. R. Yakovlev, G. Karczewski, T. Wojtowicz, and J. Kossut, *Phys. Rev. B* **75**, 115320 (2007).
- [34] Y. Shen, A. M. Goebel, and H. Wang, *Phys. Rev. B* **75**, 045341 (2007).
- [35] J. Berezovsky, M. H. Mikkelsen, N. G. Stoltz, L. A. Coldren, and D. D. Awschalom, *Science* **320**, 349 (2008).

- [36] L. Allen and J. H. Eberly, *Optical Resonance and Two-Level Atoms* (Courier Dover Publications, 1987).
- [37] D. S. Chemla and J. Shah, *Nature* **411**, 549557 (2001).
- [38] H. Haug and S. W. Koch, eds., *Quantum Theory of the Optical and Electrical Properties of Semiconductors* (Word Scientific, Singapore, 1993).
- [39] V. M. Axt and T. Kuhn, *Rep. Prog. in Phys.* **67**, 433 (2004).
- [40] P. Y. Yu and M. Cardona, *Fundamentals of Semiconductors* (Springer-Verlag, Berlin Heidelberg, 1993).
- [41] S. O'Leary, H. Wang, and J. P. Prineas, *Opt. Lett.* **32**, 569 (2007).
- [42] S. O'Leary and H. Wang, *Phys. Rev. B* **77**, 165309 (2008).
- [43] E. Blackwood, M. J. Snelling, R. T. Harley, S. R. Andrews, and C. T. B. Foxon, *Phys. Rev. B* **50**, 14246 (1994).
- [44] M. Fox, *Optical Properties of Solids* (Oxford University Press Inc, New York, 2001).
- [45] C. J. Johnson, G. H. Sherman, and R. Weil, *App. Opt.* **8**, 1667 (1969).
- [46] C. F. Klingshirn, *Semiconductor Optics* (Springer-Verlag, Berlin, Heidelberg, 1995).
- [47] M. A. Lampert, *Phys. Rev. Lett.* **1**, 45 (1958).
- [48] J. R. Haynes, *Phys. Rev. Lett.* **4**, 361 (1960).
- [49] I. Bar-Joseph, *Semicond. Sci. Technol.* **20**, R29 (2005).
- [50] K. Kheng, R. T. Cox, M. Y. d' Aubigné, F. Bassani, K. Saminadayar, and S. Tatarenko, *Phys. Rev. Lett.* **71**, 1752 (1993).
- [51] D. D. Awschalom, D. Loss, and N. Samarth, eds., *Semiconductor Spintronics and Quantum Computation* (Springer-Verlag, Berlin, 2002).
- [52] R. W. Martin, R. J. Nicholas, G. J. Rees, S. K. Haywood, N. J. Mason, and P. J. Walker, *Phys. Rev. B* **42**, 9237 (1990).
- [53] R. M. Hannak, M. Oestreich, A. P. Heberle, and W. W. Rühle, *Sol. State Comm.* **91**, 869 (1994).
- [54] O. A. Kocharovskaya and Y. I. Khanin, *Jept. Lett.* **48**, 630 (1988).

- [55] S. E. Harris, Phys. Rev. Lett. **62**, 1033 (1989).
- [56] K. J. Boller, A. Imamoglu, and S. E. Harris, Phys. Rev. Lett. **66**, 2593 (1991).
- [57] J. E. Field, K. H. Hahn, and S. E. Harris, Phys. Rev. Lett. **67**, 3062 (1991).
- [58] J. J. Finley, P. W. Fry, A. D. Ashmore, A. Lemaître, A. I. Tartakovskii, R. Oulton, D. J. Mowbray, M. S. Skolnick, M. Hopkinson, P. D. Buckle, et al., Phys. Rev. B **63**, 161305 (2001).
- [59] I. Galbraith, P. Dawson, and C. T. Foxon, Phys. Rev. B **45**, 13499 (1992).
- [60] A. Manassen, E. Cohen, A. Ron, E. Linder, and L. N. Pfeiffer, Phys. Rev. B **54**, 10609 (1996).
- [61] A. Honold, L. Schultheis, J. Kuhl, and C. W. Tu, Phys. Rev. B **40**, 6442 (1989).
- [62] E. A. Zhukov, D. R. Yakovlev, M. Bayer, M. M. Glazov, E. L. Ivchenko, G. Karczewski, T. Wojtowicz, and J. Kossut, Phys. Rev. B **76**, 205310 (2007).
- [63] V. Ciulin, P. Kossacki, S. Haacke, J.-D. Ganière, B. Deveaud, A. Esser, M. Kutrowski, and T. Wojtowicz, Phys. Rev. B **62**, R16310 (2000).
- [64] R. T. Cox, V. Huard, C. Bourgognon, K. Saminadayar, S. Tatarenko, and R. B. Miller, Acta Phys. Pol. A **106** (2004).
- [65] I. E. Perakis and D. S. Chemla, Phys. Rev. Lett. **72**, 3202 (1994).
- [66] M. S. Skolnick, J. M. Rorison, K. J. Nash, D. J. Mowbray, P. R. Tapster, S. J. Bass, and A. D. Pitt, Phys. Rev. Lett. **58**, 2130 (1987).
- [67] M. V. G. Dutt, J. Cheng, B. Li, X. Xu, X. Li, P. R. Berman, D. G. Steel, A. S. Bracker, D. Gammon, S. E. Economou, et al., Phys. Rev. Lett. **94**, 227403 (2005).
- [68] J. S. Colton, T. A. Kennedy, A. S. Bracker, and D. Gammon, Phys. Rev. B **69**, 121307 (2004).
- [69] K.-M. C. Fu, W. Yeo, S. Clark, C. Santori, C. Stanley, M. C. Holland, and Y. Yamamoto, Phys. Rev. B **74**, 121304 (2006).
- [70] G. S. Uhrig, Phys. Rev. Lett. **98**, 100504 (2007).
- [71] B. Lee, W. M. Witzel, and S. D. Sarma, Phys. Rev. Lett. **100**, 160505 (2008).
- [72] D. D. Sell, S. E. Stokowski, R. Dingle, and J. V. DiLorenzo, Phys. Rev. B **7**, 4568 (1973).

- [73] K.-M. C. Fu, Ph.D. thesis, Stanford University (2007).
- [74] V. A. Karasyuk, D. G. S. Beckett, M. K. Nissen, A. Villemaire, T. W. Steiner, and M. L. W. Thewalt, *Phys. Rev. B* **49**, 16381 (1994).
- [75] H. Wang, K. Ferrio, D. G. Steel, Y. Z. Hu, R. Binder, and S. W. Koch, *Phys. Rev. Lett.* **71**, 1261 (1993).
- [76] K. Simmons-Potter and J. H. Simmons, *J. Opt. Soc. Am. B* **13**, 268 (1996).
- [77] M. Born and E. Wolf, *Principles of Optics* (Pergamon, New York, 1980), 6th ed.
- [78] D. Loss and D. P. DiVincenzo, *Phys. Rev. A* **57**, 120 (1998).